

Copyright  
by  
Alexander Ross Meadows  
2014

**The Thesis Committee for Alexander Ross Meadows  
Certifies that this is the approved version of the following thesis:**

**The Effect of Laser Contrast and Target Thickness on Laser-Plasma  
Interactions at the Texas Petawatt**

**APPROVED BY  
SUPERVISING COMMITTEE:**

**Supervisor:**

---

Bjorn Manuel Hegelich

---

Roger Bengtson

**The Effect of Laser Contrast and Target Thickness on Laser-Plasma  
Interactions at the Texas Petawatt**

**by**

**Alexander Ross Meadows, B.S.; B.S.**

**Thesis**

Presented to the Faculty of the Graduate School of

The University of Texas at Austin

in Partial Fulfillment

of the Requirements

for the Degree of

**Master of Arts**

**The University of Texas at Austin**

**December 2014**

## **Abstract**

### **The Effect of Laser Contrast and Target Thickness on Laser-Plasma Interactions at the Texas Petawatt**

Alexander Ross Meadows, MA

The University of Texas at Austin, 2014

Supervisor: Bjorn Manuel Hegelich

A two-year experimental campaign is described during which diamond-like carbon and plastic targets with thicknesses from 20 nanometers to 15 micrometers were irradiated by the Texas Petawatt Laser. Target composition and thickness were varied to modify the specifics of the laser-matter interaction. Plasma mirrors were selectively implemented to affect the contrast of the laser system and provide additional control of the physical processes under investigation. A number of particle diagnostics were implemented to measure the distribution of laser accelerated ions and electrons. In addition, optical diagnostics were fielded to measure the intensity profile of the laser and measure the density of the target pre-plasma.

The results of these experiments suggest that the Texas Petawatt laser pulse has pre-pulse and pedestal features with intensities at least  $10^{-8}$  of the main pulse. Micron-scale targets were able to survive these features and maintain a relatively sharp density gradient until the arrival of the main laser pulse, allowing for ion acceleration. Electron spectra measured in this configuration show an average temperature of 10 MeV, with no

angular dependence out to at least 60 degrees. By contrast, interferometric plasma density measurements and a lack of any observable ion acceleration suggest that nanoscale targets were destroyed well before the main pulse. In this case, the peak of the laser pulse interacted with a cloud of plasma between  $10^{-3}$  and  $10^{-2}$  of critical density.

The contrast improvement offered by the implementation of plasma mirrors was seen to increase the maximum energy of laser accelerated protons from targets thicker than 1 micrometer. In addition, the plasma mirrors allowed nanoscale targets to survive pre-pulse and pedestal features and support the production of ion beams. Proton spectra show that ions were accelerated to greater maximum energies from nanoscale targets than from more traditional micron-scale targets. This effect can be attributed to a reduction in the target pre-plasma scale length upon the introduction of plasma mirrors. These results indicate that the manipulation of target properties and laser contrast can significantly affect the interaction between an ultrahigh intensity laser and a target.

## Table of Contents

List of Tables .....	vii
List of Figures .....	viii
Chapter 1 Introduction .....	1
Chapter 2 Background and Review of Previous Work .....	3
High Intensity Laser Systems .....	3
Laser Produced Plasma .....	12
Electron Acceleration and Heating .....	15
Ion Acceleration.....	23
Chapter 3 Experimental Set-up.....	34
Primary TPW Beamline.....	34
Targets.....	37
Plasma Mirrors.....	37
Experimental Timeline.....	40
Chapter 4 Diagnostics .....	42
Thomson Parabola .....	42
Electron Spectrometers .....	51
Image Plates .....	58
Activation Stacks .....	61
Third-Order Autocorrelator .....	66
Probe Beam and Interferometer .....	76
Chapter 5 Experimental Results.....	88
Laser Contrast .....	89
Thick Targets .....	97
Thin Targets .....	110
Chapter 6 Conclusion.....	127
Bibliography .....	131

## List of Tables

Table 1:	Relevant Nuclear Reactions in Copper .....	64
----------	--	----

## List of Figures

Figure 1:	Target Chamber Schematic.....	36
Figure 2:	Plasma Mirror Schematic.....	40
Figure 3:	Thomson Parabola Schematic.....	44
Figure 4:	Thomson Parabola Signal.....	47
Figure 5:	Thomson Parabola ROI.....	51
Figure 6:	Electron Spectrometer Schematic.....	52
Figure 7:	Electron Spectrometer Analytic Model Drawing.....	54
Figure 8:	Electron Spectrometer Calibration Data.....	55
Figure 9:	Electron Spectrometer Signal and ROI.....	57
Figure 10:	Target Chamber Diagnostics Drawing.....	62
Figure 11:	Third-Order Autocorrelator Schematic.....	71
Figure 12:	Third-Order Autocorrelator Signal.....	76
Figure 13:	Probe Beam Optics.....	80
Figure 14:	Michelson Interferometer Schematic.....	81
Figure 15:	Interferometer Signal.....	83
Figure 16:	Autocorrelation with Plasma Mirrors.....	90
Figure 17:	Texas Petawatt Pulse Profile.....	95
Figure 18:	Thick Target Activation Profile.....	99
Figure 19:	Thick Target Proton Spectrum.....	100
Figure 20:	Maximum Proton Energies From Thick Targets.....	101
Figure 21:	Thick Target Electron Spectrum.....	103
Figure 22:	Angular Electron Temperatures From Thick Targets.....	105
Figure 23:	Pre-Plasma Density Profile.....	113

Figure 24:	Second Harmonic Pre-Plasma Image.....	115
Figure 25:	Thin Target Activation Profile.....	117
Figure 26:	Activation Stack Schematic.....	118
Figure 27:	Thin Target Proton Spectrum.....	120
Figure 28:	Maximum Proton Energies From Thin Targets.....	121
Figure 29:	Thin Target Electron Spectra.....	123
Figure 30:	Angular Electron Energies From Thin Targets.....	124

## Chapter 1: Introduction

Ultrahigh intensity lasers offer a means of studying in a laboratory setting some of the most energetic physical situations ever observed. These devices produce energetic pulses of coherent light on time scales as short as tens of femtoseconds. The most cutting edge facilities can deliver over a petawatt of peak power, producing intensities as high as  $10^{22}$  watts per square centimeter within a micron-scale focal volume [1]. Research using these tools has led to rapid progress in recent years as the field of high energy density physics has grown and developed.

A major thrust of research in the field has been the production of energetic particles using lasers. Highly relativistic electrons and beams of ions with cutoff energies of 10s-100s of MeV are regularly produced through the irradiation of solid target foils. Interactions between these beams and secondary targets have also been used to produce large numbers of neutrons using these high intensity laser systems. However, precise control of the spatial, temporal, and spectral characteristics of the particles produced by these laser-matter interactions is still a topic of considerable research. The challenge of accurately manipulating these properties is a major hurdle that must be overcome before these next generation particle sources can be implemented in a wide variety of applied settings.

Beginning in October 2012 and continuing through spring of 2014, experiments were carried out at the Texas Petawatt (TPW) laser facility with the intention of producing high energy ion beams and large numbers of neutrons from the irradiation of

thin solid plastic and diamond-like carbon (DLC) targets. The physical details of the interaction between the laser light and these targets were seen to depend on both the thickness of the targets and the temporal intensity profile of the laser light.

## **Chapter 2: Background and Review of Previous Work**

### **HIGH INTENSITY LASER SYSTEMS**

The incredibly high intensities attainable by modern ultrashort pulse laser systems were made possible by the advent of the chirped pulse amplification (CPA) process. In this method, a mode-locked oscillator produces a short pulse with a durations anywhere from tens of femtoseconds to hundreds of picoseconds. A dispersive component known as a stretcher then introduces a significant group delay to the pulse, resulting in a pulse hundreds of picoseconds or nanoseconds in duration [2]. This temporally stretched pulse has a positive chirp, or an increasing instantaneous frequency [2].

The stretching process drastically reduces the intensity of the light, resulting in a pulse that can be safely amplified without damaging any sensitive optical components or introducing extreme distortions through nonlinear effects [2]. After amplification, the pulse is again compressed to an ultrashort duration by gratings that introduce a negative dispersion intended to compensate for positive dispersion in the stretcher and other media through the system [2]. In the time domain, the inverse processes of pulse stretching and compression can be seen as formally equivalent to a Fourier transform and inverse Fourier transform of the laser pulse shape [3].

Traditionally, amplification of laser pulses has been accomplished by passing the light through an energized gain medium exhibiting a population inversion. Common examples of such media include neodymium-doped glass, typically pumped by flash lamps, and titanium-doped sapphire, typically pumped by a secondary laser [4]. With this type of amplifier, the final duration of the pulse depends critically on the bandwidth of

the gain medium [4]. Modern lasers may also make use of nonlinear processes to accomplish optical parametric amplification (OPA) of a seed pulse in a crystal [5]. In this process, a pump laser directly transfers energy to the seed in a three-wave mixing process, without any excitation of the crystal media. Here, the gain bandwidth is determined by the range of wavelengths over which phase matching can occur [5].

The contrast of a laser system, a function defined as the ratio of the intensity at a given time to the peak pulse intensity, is another important consideration for the design of both high intensity laser systems and experiments performed using them. Large amounts of energy are frequently contained before the main peak of an ultrashort laser pulse in the form of a nanoseconds-long pedestal and short intensity spikes known as pre-pulses [6]. The energy deposited by these features can disrupt the integrity of targets and create a pre-formed plasma before the arrival of the main pulse [7]. This significantly modifies the dynamics of the resulting laser-matter interaction in a manner that can be very detrimental, especially in experiments with solid targets [7]. As such, considerable effort has been focused on the development of theories to describe mechanisms of contrast degradation and experimental techniques to prevent them.

The plateau shaped pedestal of a typical ultrahigh intensity laser system is produced by incomplete compression of the pulse due to nonlinear effects and amplified spontaneous emission (ASE) in the laser amplifiers. In early glass-based CPA systems, the former phenomenon was the dominant effect due to the widespread usage of fiber stretchers with unmatched grating compressors in these systems [8] [6] [9]. This configuration of the stretcher and compressor was capable of compressing the 55

picosecond output of a Nd:YAG or Nd:YLF oscillator to picosecond or sub-picosecond pulse durations, and operation at a wavelength of 1053 nanometers made it possible to utilize widely available Nd-doped glass amplifiers [9]. Unfortunately, self-phase modulation in these fiber stretchers would introduce a nonlinear chirp to the pulse that could not be fully compensated by the grating compressor [6]. Due to this effect, the contrast of early CPA systems with this architecture was often limited by a nanoseconds-long pedestal with an intensity as great as  $10^{-3}$  of the main pulse [8].

During the same time period, the use of matched grating stretchers and compressors allowed systems based on Ti:sapphire to produce pulses with much more favorable contrast ratios [10]. These systems were designed to introduce a well-defined linear chirp in the stretcher and then exactly compensate with the compressor, resulting in an output pulse that ideally had the same duration as the input [9]. These early systems were able to produce output pulses with contrast ratios as high as  $10^{-7}$ , albeit at lower intensities than modern systems [9]. However, compression to an ultrashort pulse with this configuration required an oscillator capable of delivering ultrashort pulses to the input of the stretcher [9].

In a standard CPA laser system with a well matched stretcher and compressor, the primary contribution to the intensity of the pulse pedestal is due to ASE [11]. This component of the pulse profile is generated when spontaneous emission from a laser amplifier with an inverted population is amplified by either the medium that produced it or later gain stages [12]. Spontaneous emission from a pumped amplifier occurs in all directions and with all frequencies within the fluorescence bandwidth. However, the

amplification process serves to narrow the spectrum and reduce the spatial divergence of ASE light compared to light produced by typical spontaneous emission [12]. Nevertheless, light produced by ASE is not as coherent as typical laser light and cannot be compressed with the rest of the pulse because it is not chirped [11].

The ASE component of the laser pulse profile extends in time before the main peak, beginning whenever the first excited states decay in the presence of the population inversion created by pumping the gain medium. In typical systems, this means that the pedestal formed by ASE extends for nanoseconds ahead of the main pulse [13]. The intensity of the ASE light in a given system depends on the detailed geometry and gain properties of the amplifiers in the laser chain [12]. Nevertheless, the intensity of the ASE, denoted by  $I$ , from a quantum transition with a Lorentzian lineshape can be approximated for a single gain stage. The result is given by:

$$I = \varphi \frac{h\nu_0}{\sigma\tau} \frac{\Omega}{4\pi} \frac{(G-1)^{3/2}}{[GLn(G)]^{1/2}}$$

where  $\varphi$  is the fluorescence quantum efficiency,  $h\nu_0$  is the photon energy at the center of the fluorescence bandwidth,  $\sigma$  is the peak cross-section for stimulated emission,  $\tau$  is the excited state lifetime,  $\Omega$  is the solid angle subtended by one end of the amplifier as seen from the other, and  $G$  is the peak gain of the amplifier [12]. For real systems, the intensity of this ASE component is typically between  $10^{-4}$  and  $10^{-6}$  of the peak pulse intensity [14].

The intensity profile of an ultrashort laser pulse may also include highly intense satellite pulses with durations that are comparable to that of the main pulse. These

satellites are called pre-pulses if they occur at times before the main pulse and post-pulses if they occur at later times. They can rise to intensity levels well above the pedestal, and these pre-pulses can induce significant ionization in a target before the arrival of the peak pulse intensity [7]. These features are produced by nonlinear effects and uncompensated dispersion in the laser chain, as well as undesired reflections from glass optical elements in multipass systems [3] [15]. Typically, post-pulses that arrive after the main pulse are of little interest because the target is destroyed before they ever interact with it. However, these post-pulses can generate pre-pulses through nonlinear interactions with other parts of the pulse [16].

There are a number of nonlinear phenomena that can induce modulations in either the phase or the amplitude of a chirped pulse in a CPA system [3]. These modulations result in the incomplete compression of the pulse, producing a temporal profile that exhibits pre-pulses [3]. One example of such an effect is the introduction of a nonlinear chirp throughout the system that is not compensated by the compressor [3]. As described above, this was a major problem in early CPA systems that relied on the highly nonlinear chirp induced by grating stretchers. Even with the well-matched grating stretchers and compressors used in modern ultrashort pulse systems, small misalignments can result in contrast degradation due to residual higher-order dispersion [17]. Additional sources of nonlinear chirp include optical aberrations and material dispersion in amplifiers and optics [17]. To the extent that the constant sources of dispersion in a system are understood and diagnosed, they can be compensated to third order by judicious grating

alignment and to even high orders by the introduction of optical elements with a tunable negative dispersion [17].

Another mechanism by which the phase of a chirped pulse can be distorted is known as self-phase modulation [18]. Every material exhibits a change in its index of refraction when irradiated with light of sufficient intensity, a phenomenon known as the Kerr effect [19]. At intensities for which this nonlinear effect is significant, the index of refraction of a medium, denoted by  $n$ , can be expressed as:

$$n = n_0 + n_2 I$$

where  $n_0$  is the standard linear index of the medium,  $n_2$  is the nonlinear component of the refractive index (positive for most materials), and  $I$  is the incident light intensity [18]. The result of the intensity-dependent index is the introduction of a nonlinear phase that is quantified by the so-called "B-integral":

$$B(\mathbf{r}, t) = \frac{2\pi}{\lambda} \int dz (n_2 I)$$

where  $\lambda$  is the light's wavelength,  $z$  is the propagation direction,  $\mathbf{r}$  is the position vector,  $t$  is time, and the integration is performed along the entire beam path [18]. The phase accumulation from this effect varies with both frequency (or equivalently time for a chirped pulse) and transverse position across the beam profile. This makes it difficult to compensate for self-phase modulation, and significant contrast degradation occurs for even modest distortions with  $B \sim 1$  [18].

There are also nonlinear effects that result in frequency-dependent amplitude modifications of the chirped pulse. The most familiar of these are due to the gain

properties of the amplifiers in the laser system [3]. More specifically, the phenomena of gain narrowing and gain saturation can induce relative changes in the amplitudes of different frequency components of a laser pulse [3]. Gain narrowing occurs because optical amplifiers based on transitions between atomic and molecular energy levels can only provide gain at frequencies within the bandwidth of the transition [12]. Moreover, the magnitude of the gain is typically a function of frequency that decreases from the center of the line [12]. This effect ensures that different frequency components of a pulse experience different levels of gain upon amplification. In solid state amplifiers, the result is typically an amplification-dependent loss of pulse bandwidth that can limit the minimum pulse duration of otherwise undistorted pulses after compression [3]. However, gain narrowing has also been shown to reduce compressed pulse durations in some systems by reducing the effect of nonlinear chirp on the wings of the pulse spectrum [20].

Due to the temporal separation of different frequency components in a chirped pulse, the effect of gain saturation also causes frequency-dependent amplitude distortions [3]. Gain saturation occurs when the population inversion in an amplifier is significantly depleted by the laser pulse during the interaction [12]. This results in the leading edge of the pulse, which sees with a significant population inversion, experiencing a greater gain than the trailing edge, which sees a depleted population inversion [12]. For chirped pulses, this distortion of the pulse envelope can affect the compressed intensity contrast, but the effect is usually less than that of gain narrowing [3].

All of these phase and amplitude distortion mechanisms can occur together in a chirped pulse amplification system, often with counter-intuitive results. For example, a

common scenario is the chirped pulse amplification of a primary pulse and a trailing post-pulse produced by reflections from plane-parallel optics. Recall that the stretcher essentially performs a Fourier transform on the incident temporal pulse profile.

Therefore, these two temporally separated pulses will produce a stretched pulse that is amplitude modulated in time [16]. In the absence of any other distortions, this modulation would be corrected by a matched compressor. However, amplitude-dependent phase distortions occur throughout the system due to the processes of self-phase modulation and gain saturation [16]. The amplitude modulation due to the original pre-pulse therefore introduces additional phase modulation, which leads to the formation of pre-pulses on compression [16]. For this example, an analytical treatment suggests that self-phase modulation causes the most intense of these pre-pulses, which has an energy of:

$$E = 0.58B^2P$$

where  $E$  is the pre-pulse energy,  $B$  is the B-integral, and  $P$  is the initial post-pulse energy [16].

The contrast degradation due to these nonlinear effects is somewhat mitigated in OPCPA systems [5]. The direct transfer of energy from a pump laser to the signal beam in an OPA prevents the formation of any ASE background [5]. In addition, the interaction length in the crystals of an OPA is relatively short compared to solid state amplifiers, reducing pulse distortions due to self-phase modulation and material dispersion [5]. OPA gain stages also provide amplification over a much broader bandwidth than the rare earth element-doped glass amplifiers in many systems, reducing the effects of gain narrowing [5].

However, the process of OPCAPA can also introduce contrast degradation through novel effects that are not present in more traditional CPA system. One well-known phenomenon in this category is known as optical parametric fluorescence. In this process, individual photons from the pump laser are spontaneously down-converted into two photons with half the pump frequency [21]. This results in an incoherent, incompressible pedestal with the same duration as the pump pulse, much like the ASE pedestal produced by conventional amplifiers [5]. The temporal extent of this pedestal before the main pulse can be minimized if the leading edge of the pump pulse is used for amplification [21]. Since the parametric fluorescence process competes with amplification of the main pulse, it can also be suppressed by injecting a higher energy seed into the OPA to utilize more of the pump energy for useful amplification [23]. The contrast of the parametric fluorescence pedestal in OPCPA systems varies widely, with measured values ranging from  $10^{-4}$  to  $10^{-8}$  [24].

Another mechanism of contrast degradation that is unique to OPCPA systems is due to noise in the pump laser. The gain in an OPA is very sensitive to the pump energy, so amplitude noise in this laser will modulate the spectrum of the chirped signal pulse as different spectral components experience a variable amplification [25]. High-energy commercial nanosecond lasers often exhibit noise at the  $10^{-4}$  level. In an OPA pumped with this kind of laser, pump noise has been observed to produce a 10 picosecond pedestal in the final compressed pulse at the  $10^{-3}$  intensity level [25]. As such, this effect may be the limiting factor affecting the contrast of many systems.

Unwanted reflections from optics in multipass laser systems can also produce pre-pulses capable of disrupting a target. This occurs when the small reflected component from a transmissive optic (typically anti-reflection coated) is able to short-cut one or more passes through a section of the laser chain [15]. These unwanted reflections are usually clipped by spatial filters within the laser system, which are used to remove unwanted high spatial frequencies from the beam profile. This results in a pencil beam with a significantly smaller profile than the primary laser pulse [15]. Although they will not focus correctly, these pencil beams can travel through the system and reach the target as pre-pulses. This effect can be eliminated through the use of entirely reflective optics in the laser chain or the introduction of a small tilt angle to all transmissive optics [15].

#### **LASER-PRODUCED PLASMA**

Most materials will be ionized by light at a threshold intensity of a few  $10^{14}$  watts per square centimeter, a figure easily exceeded by modern high intensity laser systems [26]. Therefore, even the lower intensity ASE and pre-pulse features of high intensity laser pulses (described in the High Intensity Laser Systems section above) are capable of rapidly stripping electrons from nuclei and forming a pre-plasma. Even on high contrast systems with no significant pre-pulses, the leading edge of the main pulse will easily ionize any solid material before the onset of peak intensity. This means that an understanding of the interactions between a plasma and an incident light field is vital for an understanding of the phenomena that occur when these systems are used to irradiate solid targets.

The presence of a plasma significantly affects the phase propagation of an electromagnetic wave, introducing a shift due to the electron density-dependent plasma refractive index.

$$n = \sqrt{1 - \frac{\omega_p^2}{\omega^2}}$$

Here,  $n$  is the plasma refractive index,  $\omega$  is the electromagnetic wave frequency, and  $\omega_p$  is the plasma frequency, given by:

$$\omega_p = \sqrt{\frac{n_e e^2}{\epsilon_0 m_e}}$$

where  $n_e$  is the electron number density,  $e$  is the electronic charge,  $\epsilon_0$  is the permittivity of free space, and  $m_e$  is the electron mass [27]. The plasma is transparent to electromagnetic waves with frequencies above the plasma frequency, while waves of lower frequency are reflected. If the index of refraction of a plasma can be measured by some method, the plasma density can then be determined.

For laser light of a given fixed wavelength, the index of refraction of a plasma becomes imaginary at a certain density, known in this context as the critical density. Diffuse plasma below this density will be transparent to a laser, interacting relatively weakly with the light. By contrast, plasma above the critical density will reflect the laser, presenting an interface at which significant interactions can occur. If there is a plasma density gradient that ramps up to the critical density, then the surface at which this density is attained is called the critical surface. Plasmas with this structure are typically

formed when the front surface of a solid target is ionized, producing some amount of pre-plasma at their front surface.

As described in the High Intensity Laser Systems section above, most highly intense laser pulses have some pre-pulse and pedestal features that are capable of ionizing solid targets before the arrival of the peak light intensity. The intensity of the pre-pulses and their time of arrival at the target influence both the extent of the ionization and the degree of plasma expansion beyond the original target surface. In turn, these properties can significantly influence the laser-matter interaction upon the arrival of the main pulse. Mathematically, the dimensions of the pre-plasma are described by the plasma scale length, denoted by  $L$ , and given by:

$$L^{-1} = \left| \frac{d(\ln N_e)}{dz} \right|$$

where  $N_e$  is the plasma electron density,  $z$  is the laser propagation direction, and the expression is evaluated at the critical density surface.

Short scale length plasmas have a relatively sharp increase in the plasma density, which typically reaches values above critical density. This type of pre-plasma is formed when a solid target is only pre-ionized at times shortly before the arrival of the main pulse, precluding any significant plasma expansion. By contrast, long scale length plasmas present a much gentler density gradient that may never reach critical density, indicating significant expansion due to the ionization of the target at times well before the arrival of the main pulse. Details about the impact of the pre-plasma scale length on ion acceleration from solid targets is discussed in the Ion acceleration section of this chapter.

## ELECTRON ACCELERATION AND HEATING

By virtue of their relatively small mass, electrons are the first particles in a target to absorb appreciable energy from a driving laser pulse. As such, an understanding of the behavior of electrons in the field of an intense light wave is vital for an understanding of more complex laser-matter interactions. Therefore, consider a plane electromagnetic wave propagating in the  $x$ -direction with a dimensionless vector potential, denoted  $\mathbf{A}$ , given by:

$$\mathbf{A} = \hat{y}\delta a_0 \cos(\omega t - kz) + \hat{z}\sqrt{1 - \delta^2}a_0 \sin(\omega t - kz)$$

where  $\hat{y}$  and  $\hat{z}$  are unit vectors,  $a_0$  is a dimensionless amplitude,  $\omega$  is the wave frequency,  $k$  is the wavenumber, and  $\delta$  is a polarization parameter. In this case,  $\delta = \pm 1, 0$  corresponds to a linearly polarized wave and  $\delta = \pm \frac{1}{\sqrt{2}}$  corresponds to a circularly polarized wave. The physical electric field, denoted  $\mathbf{E}$ , and magnetic field, denoted  $\mathbf{B}$ , can be determined by the standard procedure:

$$\mathbf{E} = -\frac{\partial \mathbf{A}}{\partial t}$$

$$\mathbf{B} = \nabla \times \mathbf{A}.$$

Given these fields, the equation of motion for an electron is given by:

$$\frac{d\mathbf{p}}{dt} = -e \left( \mathbf{E} + \frac{\mathbf{v}}{c} \times \mathbf{B} \right)$$

where  $\mathbf{p}$  is the electron momentum,  $\mathbf{v}$  is the electron velocity,  $e$  is the electron charge, and  $c$  is the speed of light.

Solving these equations yields the electron orbits and illustrates some important features of the behavior of electrons in the field of a wave. For an electron that is initially at rest at the origin:

$$\mathbf{p} = \hat{x} \frac{a_0^2}{4} [1 + (2\delta^2 - 1) \cos(2\phi)] + \hat{y} \delta a_0 \cos(\phi) + \hat{z} \sqrt{1 - \delta^2} a_0 \sin(\phi)$$

$$\mathbf{x} = \hat{x} \frac{a_0^2}{4} \left[ \phi + \frac{(2\delta^2 - 1)}{2} \sin(2\phi) \right] + \hat{y} \delta a_0 \sin(\phi) - \hat{z} \sqrt{1 - \delta^2} a_0 \cos(\phi)$$

where  $\mathbf{x}$  is the particle's position and  $\phi$  is the phase of the wave. Two facts about this solution are immediately striking. First, the electron has a constant drift velocity in the direction of wave propagation. Second, the electron oscillates in this longitudinal propagation direction at twice the wave frequency while oscillating at the fundamental frequency in the transverse directions. The velocity of the oscillations, known as the quiver velocity and denoted by  $v_{osc}$ , and the amplitude of the electric field, denoted by  $E_0$ , are given in terms of the dimensionless amplitude by:

$$a_0 = \frac{\gamma v_{osc}}{c} = \frac{eE_0}{mc\omega}$$

where  $\gamma$  is the relativistic gamma and  $m$  is the electron mass. Light at a wavelength of  $\lambda$  with an intensity greater than  $\lambda^2 I = 1.37 \times 10^{18} \frac{W \cdot \mu m^2}{cm^2}$  will drive electrons with a quiver energy greater than their rest mass.

The fields experienced by particles at the focus of a highly intense laser are quite different from infinite plane waves. The spatially varying amplitude of the field in a laser beam introduces a force in the opposite direction of the field gradient, known as the ponderomotive force [28]. Qualitatively, this occurs because electrons are displaced by

the strongest field regions and experience a weaker restoring force that does not return them to their original position. Mathematically, the ponderomotive force (denoted by  $\mathbf{F}_P$ ) due to a wave with electric field magnitude  $E$  is given in the non-relativistic case by:

$$\mathbf{F}_P = -\frac{e^2}{4m\omega^2}\nabla E^2$$

where  $\omega$  is again the wave frequency [28]. This force tends to repel charged particles from high field areas, such as the focus of an intense laser pulse, and convert the quiver energy of electrons into thermal energy. For laser systems, the magnitude of this effect is often quantified by a ponderomotive potential, denoted by  $U_p$ , which is given in terms of the laser parameters by:

$$U_p = 9.33 \times 10^{-14} \frac{eV}{(W/cm^2)(\mu m^2)} * I * \lambda$$

where  $I$  is the laser intensity in watts per square centimeter and  $\lambda$  is the laser wavelength in micrometers. Ponderomotive heating is the dominant energy absorption process for electrons at very high intensities. This mechanism heats electrons to a characteristic temperature, denoted  $T_e$ , given by:

$$T_e = mc^2 \left( 1 + \frac{2U_p}{mc^2} \right)^{1/2}$$

where  $m$  is the mass of the electron and  $c$  is the speed of light [29].

As discussed in the Laser Produced Plasmas section above, the electrons irradiated by a high intensity laser pulse are generally the constituents of a pre-formed target plasma. The electrons in such a plasma can absorb significant energy through interactions with incident light waves. In the simplest case, damping of an

electromagnetic wave propagating in an underdense plasma occurs due to collisions between electrons and ions, which serve to turn light energy into thermal energy of the bulk plasma. This effect can be described mathematically by introducing a dielectric constant that contains both real and imaginary parts:

$$\epsilon(\omega) = 1 - \frac{\omega_p^2}{\omega(\omega + i\nu_{ei})}$$

where  $\nu_{ei}$  is the electron-ion collision frequency,  $\omega$  is the electromagnetic wave frequency, and  $\omega_p$  is the plasma frequency. In turn, this parameter can be expressed in terms of more fundamental properties of the plasma by:

$$\nu_{ei} = 3 \times 10^{-6} Z n_e T_e^{-3/2} \ln \Lambda$$

where  $Z$  is the average number of electrons per ion,  $n_e$  is the electron density in particles per cubic centimeter,  $T_e$  is the electron temperature in electronvolts, and  $\ln \Lambda$  is the Coulomb logarithm. This collision frequency can also be used to express the mean free path of electrons between collisions, denoted by  $l_e$  and given by:

$$l_e = \frac{v_{th}}{\nu_{ei}}$$

where  $v_{th}$  is the mean thermal electron velocity.

While this collisional absorption of light energy can occur throughout an underdense plasma, significantly more absorption occurs at the critical density surface of an overdense plasma. For a relatively cool, collisional plasma, the classical skin effect is the most familiar of the phenomena that occur at this surface. When light is reflected by a conductor such as a plasma, it penetrates past the reflective surface with an exponentially

decaying amplitude. The  $1/e$  distance scale of this decay is given by the skin depth, denoted by  $\delta$  and given for a plasma by:

$$\delta = \frac{c}{\omega_p}$$

where  $c$  is the speed of light. As long as the mean electron free path is less than the skin depth,  $l_e < \delta$ , then electrons within the skin layer are driven by the light field and dissipate energy through collisions.

In fact, the hot, dense plasmas produced by irradiating solid targets with ultraintense laser pulses do not typically absorb an appreciable amount of energy through collisions. Therefore, the absorption mechanisms discussed above do not directly apply to these plasmas. This is because the extremely rapid heating produced by ultrashort pulses drives up the plasma temperature to such an extent that the electron-ion collision frequency, which scales like  $\nu_{ei} \sim T_e^{-3/2}$ , drops below the driving laser frequency. At this point, the plasma becomes essentially collisionless and its dynamics are very strongly influenced by the driving field. In terms of experimental parameters, collisional processes can play only a small role in energy absorption when the laser energy is greater than about  $10^{15}$  watts per square centimeter. As such, a variety of collisionless absorption mechanisms have been described for these plasmas, many of which have strong analogies with more well-known phenomena.

One of the most well known of these collisionless energy absorption mechanisms is resonance absorption. In this process, light energy from the driving laser pulse is coupled into plasma waves at the critical surface [30]. This occurs only when there is a

component of the electric field perpendicular to the plasma gradient, and the absorption is strongly dependent on the light's incidence angle [30]. The waves driven by the field are damped by wave breaking at low temperatures and Landau damping at higher temperatures, coupling wave energy into thermal plasma energy [31] [32]. This process can result in a very efficient transfer of energy if the scale length of the plasma is long. So, the condition for efficient resonant absorption is  $kL \gg 1$ , where  $k$  is the laser wavenumber.

Despite the collisionless nature of resonance absorption, the plasma scale length dependence of this process implies that the classical version of this mechanism does not significantly contribute to energy absorption in short scale length plasmas produced from solid targets. In this context, it is quite possible for the resonant wave amplitude to exceed the scale length of the plasma, and it no longer makes sense to speak in the language of plasma waves. More precisely, this new regime is reached when the intensity of the laser is great enough to produce electron quiver velocities, denoted  $v_{osc}$ , such that:

$$\frac{v_{osc}}{\omega} > L$$

where  $L$  and  $\omega$  are again the plasma scale length and laser frequency, respectively [33]. In this regime, the driving laser pulls electrons out of the plasma and into the surrounding vacuum before accelerating them back into the plasma. Since the laser does not penetrate far past the critical surface, the energy of these electrons becomes thermal energy of the plasma. This mechanism, known as Brunel Absorption or vacuum heating, results in a transfer of energy to the plasma with a characteristic power, denoted by  $P$  and given by:

$$P_{abs} = \frac{\eta}{2\pi} v_{osc} \frac{E_0^2}{8\pi}$$

where  $E_0$  is the amplitude of the driving light field and  $\eta$  is an efficiency parameter [33].

A modified version of the classical skin effect can also describe a mechanism of energy absorption in this type of hot, dense, collisionless plasma. The so-called anomalous skin effect occurs when the classical skin depth is less than both the electron free path due to collisions,  $l_e > \delta$ , and the mean electron displacement over one period of the driving field,  $\frac{v_{th}}{\omega} > \delta$  [34]. In this regime, the energy dissipation is no longer local and the electric field penetrates the plasma within an anomalous skin depth, denoted by  $\delta_a$  and given by:

$$\delta_a = \left( \frac{c^2 v_{th}}{\omega \omega_p^2} \right)$$

where all the variables are as defined previously [34]. The fractional portion of the light energy absorbed through dissipation in this anomalous skin layer, denoted by  $A$ , is given in the overdense plasma limit by:

$$A = \frac{\omega}{c} \delta_a$$

where this expression is valid for normal incidence of the light wave [35].

Electrons in a plasma can also gain energy by virtue of the longitudinal motion induced at twice the driving frequency by an ultrahigh intensity laser, as described above [36]. This motion is produced by the magnetic deflection of particles that are moving in the direction of the light wave's electric field. As such, the magnitude of this component of the motion only becomes significant at relativistic intensities. In the field of a real laser

beam, there is a longitudinal ponderomotive force at twice the fundamental frequency associated with this motion, given by:

$$\mathbf{F}_P = -\frac{e^2}{4m\omega^2} \frac{\partial}{\partial x} E^2(x) \cos(2\omega t)$$

where the wave is propagating in the  $x$ -direction and dependence on any other variables has been ignored [36]. This mechanism of energy transfer to electrons by longitudinal oscillations against the field gradient is called  $\mathbf{J} \times \mathbf{B}$  heating, in analogy with the magnetic deflection experienced by a current density  $\mathbf{J}$  in a magnetic field [36]. The rate of energy absorption by this process decreases with increasing plasma density, as the light wave cannot penetrate as far into the plasma and accelerate as many electrons [37].

Experimentally, highly energetic electrons are routinely observed to be accelerated from solid targets upon their irradiation by high intensity lasers. Interactions between petawatt class lasers and thick metal targets have been observed to produce electron beams containing particles with energies in excess of 100 MeV [38]. The details of the interaction between the laser and the solid target and the directionality of the resulting electrons have been seen to depend on the properties of the plasma at the front target surface [39]. In particular, the direction of such an electron beam has been seen to move from the target normal direction to the laser wave-vector direction as the scale length of the target pre-plasma increases [39].

Energetic jets of electrons can also be produced by the irradiation of plumes of slightly underdense plasma. This scenario can occur when a pre-pulse ionizes a target well before the arrival of the main laser pulse, giving the plasma time to expand and drop

below critical density. Simulations suggest that a laser incident on plasma at this density tends to filament and forms jets of electrons that are confined by the pinch of their own magnetic field [40]. Here, electrons gain energy due to a betatron resonance between the driving field and transverse oscillations of the particles across the plasma channels produced by the highly intense light [41].

This mechanism of electron production, known as direct laser acceleration, has been observed in experiments with gas targets between  $10^{-2}$  and  $10^{-1}$  of critical density at the ATLAS laser at the Max-Planck-Institut für Quantenoptik [42]. Similar results have been obtained at the Laboratoire d'Optique Appliquée in Palaiseau, France by irradiating thin foils with a laser known to have a significant ASE pedestal. This pedestal fully ionized the target, leaving it time to expand before the arrival of the main pulse. The majority of the light energy then interacted with a plasma cloud between  $10^{-3}$  and  $10^{-2}$  of critical density [43].

## **ION ACCELERATION**

Beams of high energy protons and ions have a wide variety of potential applications to science and industry, ranging from ion-based drivers for fast ignition fusion energy sources to radiation sources for the treatment of cancer. Traditionally, beams of this kind have only been produced at expensive accelerator facilities, limiting their widespread implementation. However, in recent years, the use of ultra-intense laser systems to produce high quality ion beams has paved the way for the growth of this research area at universities and smaller scale research facilities. A variety of experimental efforts around the world are currently focused on improving the

characteristics of these beams and understanding the physics underlying their production during intense laser-plasma interactions.

The production of energetic ions in laser-matter interactions has been a well-documented phenomenon since the earliest nanosecond pulse experiments of the 1960s [44]. These ions were observed in all directions, and they were often seen to absorb a significant portion of the incident laser energy [45]. At this time, high intensity lasers were primarily used for fusion research, and the transfer of laser energy to ions was generally seen as an undesirable effect limiting useful energy absorption [45]. Experimental and theoretical studies in this regime identified the mechanism of ion acceleration as the formation of charge separation fields at the boundary of the target plasma [45].

The accepted physical picture describing these early fusion experiments is one in which electrons are primarily heated by resonance absorption at the critical density surface throughout the duration of the nanosecond laser pulse (as described in the section above describing Electron Acceleration and Heating) [45]. The hot electron population produced by this process then expands into the vacuum surrounding the target, producing an electric field that accelerates ions [46]. This field preferentially accelerates ions with the largest charge to mass ratio, and the resulting energetic particles are typically dominated by hydrogen from contaminants on the target surface [45]. Theoretically, the magnitude of the accelerating field, denoted by  $E$ , is determined by the hot electron temperature and the local scale length of the plasma by:

$$E = \frac{T_e}{eL}$$

where  $T_e$  is the hot electron temperature,  $e$  is the electron charge, and  $L$  is the plasma scale length [46]. In nanosecond pulse experiments, the magnitude of this accelerating was therefore limited by both the achievable electron temperature and the development of a long scale length plasma during the relatively long laser pulse.

A new era of ion acceleration experiments was precipitated by the construction of the first petawatt class laser, located at Lawrence Livermore National Laboratory [47]. This system was used to produce pulses from 0.5 to 5.0 picoseconds in duration that were focused to intensities as high as  $3 \times 10^{20}$  watts per square centimeter onto solid gold and plastic targets with thicknesses from 20 to 120 micrometers [48]. This resulted in the production of collimated beams of protons with energies as high as 55 MeV from the rear unirradiated target surface [48]. The observed particles were more energetic than empirical scaling laws from previous experiments would predict, and they were well collimated in the target normal direction [49]. These unique features suggested the onset of new physical processes in the regime of ion acceleration driven by ultrashort petawatt laser pulses [50].

An accepted theoretical picture was soon developed to describe ion acceleration by ultrashort high energy pulses. In this regime, acceleration of ions occurs from the back surface of the target in a process known as target normal sheath acceleration (TNSA) [50]. As in the nanosecond pulse case, electrons absorb energy from the laser at the critical density surface, pass through the bulk of the foil, and expand into the vacuum.

The distinguishing features of the ultrashort pulse high intensity regime include electron heating by fundamentally different energy absorption mechanisms (as described in the Electron Acceleration and Heating section above), resulting in enhanced electron temperatures of 1 MeV or greater [50]. In addition, the ultrashort duration of the laser pulse provides impulsive heating without allowing time for the target plasma to expand, preserving the short scale length at the rear target surface [50]. Given typical experimental parameters in this regime for electron temperature and plasma scale length of  $T_e = 2$  MeV and  $L \cong 1$  micrometer, the sheath field at the rear target surface exceeds  $10^{12}$  volts per meter. This is much greater than the sheath fields produced in nanosecond pulse experiments, as well as the electric fields in conventional particle accelerators [50].

By modeling the expansion of a plasma into a vacuum, theoretical expressions were developed to describe the properties of ions accelerated by the TNSA process. The simplest relevant model is a one-dimensional approximation of TNSA, in which electrons are heated to a temperature of  $T_e$  and expand from the rear target surface, which initially presents a perfectly sharp interface [51]. The expanding electrons come to equilibrium with an electrostatic potential, which then accelerates an ion front that propagates into the vacuum, preceded by the electrons [51]. The peak electric field magnitude is located at the position of the ion front, which is also where the most energetic ions are located [51].

This one-dimensional model gives a theoretical expression for the maximum energy of protons produced by TNSA, given by:

$$E_p = 2T_e \left\{ \ln \left[ \frac{t_i \omega_{pp}}{\sqrt{2e_E}} + \sqrt{1 + \left( \frac{t_i \omega_{pp}}{\sqrt{2e_E}} \right)^2} \right] \right\}^2$$

where  $E_p$  is the proton cutoff energy,  $e_E = 2.71828 \dots$  is the Euler number, and  $t_i$  is the interaction time [7]. The proton plasma frequency at the rear target surface also enters into this equation, and is given by:

$$\omega_{pp} = \sqrt{\frac{n_{e0} e^2}{\epsilon_0 m_p}}$$

where  $n_{e0}$  is the initial electron density at the rear target surface,  $e$  is the electron charge,  $\epsilon_0$  is the permittivity of free space, and  $m_p$  is the proton mass. The initial electron density at the rear of the target can be approximated by assuming that the laser, of pulse duration  $\tau$ , is focused to a spot of radius  $r$  on a target of thickness  $d$  at an incidence angle of  $\theta$ . The laser accelerates an electron beam of length  $c\tau$  comprised of  $N_e$  electrons, where:

$$N_e = \frac{\eta E}{T_e}$$

with  $0 < \eta < 1$  the efficiency of energy absorption by electrons and  $E$  the laser pulse energy. This results in an electron density at the rear target surface given by:

$$n_{e0} = \frac{N_e}{c\tau\pi \left[ r + \frac{d}{\cos(\theta)} \tan(\theta_e) \right]}$$

where  $\theta_e$  is the half-angle through which the electron beam diverges [7]. This model describes ion acceleration with reasonable accuracy for targets without any pre-formed plasma at the rear surface [7]. However, it fails for thinner targets and targets irradiated

by laser with significant pre-pulses due to the influence of the rear surface plasma gradient [7].

Clearly, the sharp density gradient at the rear target surface is a necessity for ion acceleration to high energies through the TNSA mechanism [50]. This proposition has been validated by both theoretical and experimental work suggesting that the introduction of a shallow density gradient at the rear target surface leads to reduced ion energies [52] [53]. Theoretically, simulations have demonstrated a decrease in the maximum ion energy produced by TNSA when an initial ion density scale length larger than a few percent of the target thickness is introduced at the rear interface [52]. Experimentally, the validity of this principle was demonstrated by an experiment at Rutherford Appleton Laboratory in which a 1 picosecond pulse was focused onto 25 micrometer thick aluminum targets with an intensity of  $5 \times 10^{19}$  watts per square centimeter, resulting in the production of protons with energies as high as 21.7 MeV [53]. The same targets were then irradiated after the formation of a preformed plasma on the rear surface by a 600 picosecond pulse with intensity  $5 \times 10^{19}$  watts per square centimeter at a time 250 picosecond before the main pulse. On these shots, an interferometer measured a 100 micrometer scale length plasma extending from the rear target surface at the time of arrival of the main pulse [53]. No protons with an energy exceeding 5 MeV were observed on these shots, confirming the detrimental effect of a pre-formed plasma on the TNSA process [53]. This principle explains the relatively low energy of ions originating from the front surface of laser target, which is typically pre-ionized by pre-pulse and pedestal features of the laser pulse to form a spherical plasma with a shallow density

gradient (as described in the High Intensity Laser Systems and Laser Produced Plasma section above) [50].

As stated above, the strong electrostatic sheath field generated during the TNSA process preferentially accelerates ions with the greatest charge to mass ratio. This typically results in an ion beam dominated by hydrogen originating from a thin layer of hydrocarbon contaminants on the rear target surface [50]. These protons shield the sheath field of the electrons and inhibit the efficient acceleration of heavier ion species [54]. However, the possibility of inhibiting proton acceleration has been demonstrated through the implementation of target cleaning methods that remove adsorbed hydrocarbons. One group at Lawrence Livermore National Laboratory first irradiated 15 micrometer thick gold foils at intensities  $> 10^{20}$  watts per square centimeter, producing more than  $10^{11}$  protons per shot [55]. They then used an argon-ion sputter gun to selectively remove hydrocarbon contaminants from the front or back target surfaces [55]. This process decreased the observed proton yield by more than 99% when applied to the rear target surface, but had no effect when the front target surface was cleaned [55].

Beams of heavier ions have also been produced in laser acceleration experiments by the inhibition of proton acceleration and the implementation of microstructured targets. More specifically, a group at the Laboratoire pour l'Utilisation des Lasers Intenses (LULI) produced 50 micrometer thick aluminum and tungsten foils with rear surface coatings of 1 micrometer thick carbon and 300 nanometer thick calcium fluoride, respectively. These foils were then resistively heated inside the vacuum target chamber to temperatures of 600 kelvin for aluminum and 1200 kelvin for tungsten in order to remove

hydrocarbon contaminants [56]. Upon irradiation at intensities  $5 \times 10^{19}$  watts per square centimeter, ion signals corresponding to various carbon and fluorine charge states were observed [56]. This work was continued at Los Alamos National Laboratory, where beams of beryllium, carbon, oxygen, fluorine, and palladium ions were produced with energies greater than 1 MeV per nucleon using the same method [54].

The energy distribution of ions produced through this TNSA mechanism is typically exponential, with a 100% energy spread and a sharp cutoff energy [57]. This unattractive spectrum has prevented the widespread use of these beams for many applications and motivated a search for experimental conditions capable of producing quasi-monoenergetic ion beams. Some progress has been made toward this goal through the implementation of targets with relatively small ion source dimensions. The group at Los Alamos National Laboratory resistively heated a palladium foil to 1,100 kelvin, removing all hydrogen contaminants and leaving only a layer of graphitic carbon a few monolayers thick. This extremely thin source layer led to the quasi-monoenergetic acceleration of  $C^{5+}$  to an energy of about 3 MeV per nucleon [57]. Another experiment in the same vein was carried out at the University of Jena, where researchers demonstrated quasi-monoenergetic acceleration of protons to about 1.2 MeV from a microstructured target. Here, the low energy spread of the ions was attributed to the small transverse dimensions of a hydrogen-rich PMMA dot deposited on the back surface of a solid target [58].

All of these experimental and theoretical studies present substantial evidence that the TNSA mechanism is responsible for ion acceleration from laser irradiated targets

thicker than one micrometer. However, new phenomena have been observed in simulations and experiments investigating the irradiation of ultrathin nanoscale targets, including ion acceleration by a new mechanism known as the break-out afterburner (BOA) [59]. In this regime, the laser pulse initially penetrates the front target surface up to the skin depth and heats electrons to relativistic energies through the ponderomotive force, as in TNSA [60]. The relativistic mass increase of these electrons increases the skin depth by a factor of  $\sqrt{\gamma}$ , where  $\gamma$  is the relativistic gamma factor of the electrons, enhancing the ability of the laser to further heat electrons [60]. This process continues until the skin depth has increased to the thickness of the target [61]. At this point, the conditions for BOA acceleration are met if:

$$\frac{n_e}{\gamma n_{cr}} \leq 1 < \frac{n_e}{n_{cr}}$$

where  $n_e$  is the electron density and  $n_{cr}$  is the classical critical density [61].

The condition for BOA ion acceleration is therefore one of induced relativistic transparency in a classically overdense plasma [60]. This occurs when the plasma's constituent electrons experience a significant relativistic mass increase before the plasma can expand to a classically underdense state [60]. Simulations suggest that ions accelerated by the BOA mechanism gain most of their energy throughout this period of relativistic transparency [60]. During this time, the laser pulse passes through the plasma and the target electrons are exposed to the intense driving field, which produces a large forward motion of these particles at relativistic velocities [61]. The ions are still moving

relatively slowly at this point by virtue of their greater mass, so there exists a large relative drift between these particles and the electrons [61].

The existence of a large relative drift velocity between different charge species is a physical situation that is unstable to the so-called Buneman instability [62]. In the BOA process, a relativistic variant of this well-known instability neutralizes the relative drift between electrons and ions by imparting a forward velocity to the ions [63]. This occurs by the transfer of energy and momentum from the electron population to the ions [61]. However, the electrons are continually driven by the co-propagating laser pulse, so this ion acceleration process can occur repeatedly and impart these particles with significant energies [61]. Unlike TNSA, which only accelerates ions from a thin contaminant layer, this BOA process accelerates all the target ions [61].

As described above, BOA acceleration requires the irradiation of fragile nanoscale targets, which must not expand significantly before the arrival of the main laser pulse if a state of relativistic transparency is to be achieved. Therefore, experimental investigation of this process requires a laser system with exceedingly high contrast. The Trident laser at Los Alamos National Laboratory was the first system to overcome this difficulty and experimentally realize BOA acceleration of ions [61] [64]. The pulse contrast required to access this regime was attained in initial experiments through the implementation of a double plasma mirror filter (a method described in the Plasma Mirrors section of the Experimental Methods chapter) [64]. An upgrade to the laser soon supplied a more permanent solution by introducing an Optical Parametric Amplification Pre-Pulse Eliminator into the laser chain.

The first BOA ion acceleration experiments at trident produced carbon ions with energies greater than 185 MeV, a factor of three greater than the record energy of previous experiments [64]. This experimental evidence demonstrated the feasibility of the BOA mechanism as well as its ability to produce greater particle energies than TNSA [64]. Further experiments with the upgraded Trident system ultimately resulted in the acceleration of carbon ions from resistively heated targets to an energy of 1 GeV [61]. In addition to these experimental results, simulation campaigns at Los Alamos also suggest that BOA acceleration may be capable of producing mono-energetic ion beams [65]. As such, there is currently considerable interest in reproducing these results at other laser facilities in order to learn more about the physics of the BOA and the laser-matter interactions that lead to these record ion energies.

## Chapter 3: Experimental Set-Up

### PRIMARY TPW BEAMLINER

The experiments described in this thesis were performed at the Texas Petawatt laser facility, located on the campus of the University of Texas in Austin. This research laboratory is administered by the Texas Center for High Energy Density Science, and houses one of the most powerful lasers in the world. As a user facility, the laboratory has hosted researchers from all over the world, and offers unique experimental capabilities for the investigation of high field phenomena.

The Texas Petawatt laser produces 150 femtosecond pulses containing as much as 180 joules of energy at a 1058 nanometer wavelength [66]. It achieves this level of performance through the implementation of a unique hybrid design combining optical parametric chirped pulse amplification on the front end with power amplification in neodymium-doped mixed glass. This allows the system to realize high pulse energies comparable to those produced at other large glass systems while still retaining enough bandwidth to compress the pulse to an ultrashort duration [66]. After amplification, the pulse is sent to a compressor containing two 40 centimeter by 80 centimeter multilayer dielectric gratings offering an efficiency of 85% [66]. After a double pass of this grating system, a turning mirror directs the beam to one of two experimental vacuum target chambers with different geometries. One chamber, optimized for the irradiation of gaseous targets, and contains an  $f/40$  focusing optic to provide a relatively large interaction volume. By contrast, the other chamber, shown in figure 1 and utilized for the experiments described in this manuscript, contains a custom  $f/3$  off-axis parabola for the

irradiation of solid targets with maximum intensity. Both the compressor chamber and the experimental target chamber are kept at a high vacuum of  $10^{-6}$  torr in order to protect the large compressor gratings and prevent dielectric breakdown of the air in the strong fields at the laser focus.

As part of standard operating procedure, a number of performance metrics are recorded for each shot of the Texas Petawatt laser. Using the leakage from a mirror after the compressor, a diagnostic package provides pulse duration, energy, and equivalent focal spot size measurements to experimentalists. During the experiments described in this thesis, typical on-target intensity levels during the experiments were calculated from these measurements to be a few  $10^{20}$  watts per square centimeter, with some exceptional shots reaching as high as  $10^{21}$  watts per square centimeter. Most shots during this campaign were taken at a reduced energy level of about 90 joules per pulse, due to damage in the optical system.

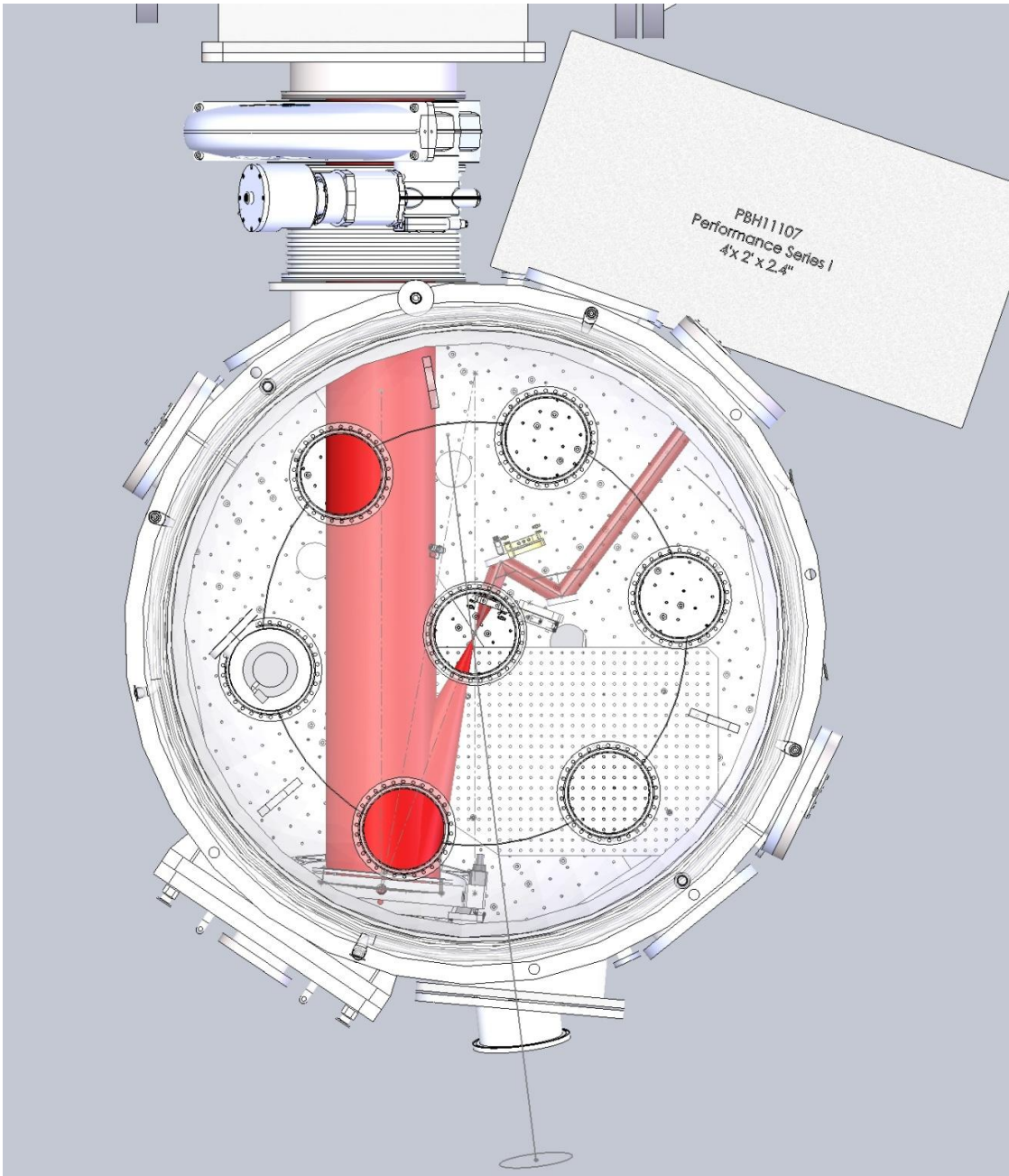


Figure 1: Schematic of the vacuum target chamber in which the TPW laser pulse was brought to a focus on solid targets. In order to diagnose the laser focus, removable optics were inserted to collimate the beam and then image the focus to a camera outside the chamber.

## **TARGETS**

Diamond-like carbon and thin plastic foils were the primary targets for the TPW laser. Both types of targets were available in thicknesses from tens of nanometers to fifteen microns. The interaction between a laser pulse and a target can depend greatly on the target thickness, so this wide range of target properties ensured that various physical situations of interest were available for investigation. Each target was irradiated by the laser at normal incidence.

In order to ensure that these targets were at the best focus of the laser beam, an optical system was used to image the laser beam outside of the vacuum target chamber. This optical chain consisted of a microscope objective and two achromatic lenses, which were used to view the oscillator beam on a camera. After obtaining an image, the best focus of the laser was brought to the object plane of this optical system using the final focusing parabola. The target was then brought to the laser focus by ensuring that it was also in focus on the same camera, specifically in the focus of the high NA microscope objective. In order to prevent damage to these focal diagnostic optics, they were moved out of the laser path before each system shot.

## **PLASMA MIRRORS**

To improve the on-target contrast at the Texas Petawatt laser, a double plasma mirror apparatus was employed on many shots. This method is based on the principle of self-induced plasma shuttering, and was implemented in the context of ultrafast high energy laser optics as early as 1991 [26]. Typically, dielectric slides are introduced after the final focusing optic in a laser system. The slides offer only a small reflectance for

light at intensities below the ionization threshold of about  $10^{14}$  watts per square centimeter, but become highly reflective at greater intensities due to the formation of a plasma [26]. If the slides are placed at a position along the focusing beam such that pre-pulse and pedestal features fall below this threshold, they can affect a significant reduction in the intensity of these features on a target. By contrast, the rising edge of the main laser pulse from such a system is capable of ionizing the front surface of the slides, ensuring nearly perfect specular reflection from the resulting plasma [26].

This double plasma mirror method has been implemented at various laser facilities in the past, such as the Trident system at Los Alamos National Laboratory [64]. During this experiment, two anti-reflection coated glass slides were introduced after the  $f/3$  focusing optic at a position optimized for maximum contrast improvement. The energy throughput of this double plasma mirror apparatus was measured to be between 50% and 60% [64]. This method provided a measured contrast increase from the  $10^{-8}$  level to  $10^{-12}$  at picoseconds before the main pulse. This improvement allowed for the irradiation of ultrathin nanoscale diamond targets, which provided the first observation of enhanced ion energies due to break-out afterburner acceleration (as described in the Ion Acceleration section of the Background and Review of Previous Work chapter) [64].

The plasma mirror device utilized at the TPW facility was very similar to the one used in the early BOA experiments at Los Alamos. It consisted of two parallel dielectric slides placed after the final focusing parabola in the experimental target chamber. As shown in figure 2, the plasma mirrors were positioned so that the laser spot on the first one was 12 millimeters in diameter. The energy throughput of this plasma mirror apparatus

was measured by picking off a small part of the expanding laser beam after the focus and sending it to an energy meter. The result of these measurements indicated a throughput of 69%, in agreement with typical values in the literature [64] [67].

While the introduction of plasma mirrors reduced the total energy deposited on the target, it succeeded in reducing the disturbance of a target foil by pre-pulse and pedestal features of the laser's intensity profile as well. This method allowed us to observe ion acceleration from ultrathin targets that were unable to support a sheath field and produce an ion beam when irradiated by the unfiltered TPW pulse (as described in the Thin Targets section of the Results chapter). Both uncoated glass microscope slides and optically polished anti-reflection coated substrates were employed for this pulse cleaning purpose. Before ignition, the uncoated slides with a refractive index of  $n \cong 1.5$  provided a reflectance of about 9% per surface due to Fresnel reflections of the s-polarized TPW beam. Therefore, these slides were only capable of reducing the intensity of undesirable features before the main pulse by a factor of  $0.09^2 = 8.5 \times 10^{-3}$ . On the other hand, the anti-reflection coated substrates provided a reflectance of less than 0.5% at each surface, resulting in an approximate intensity reduction of pre-pulse and pedestal features by a factor of  $0.005^2 = 2.5 \times 10^{-5}$ .

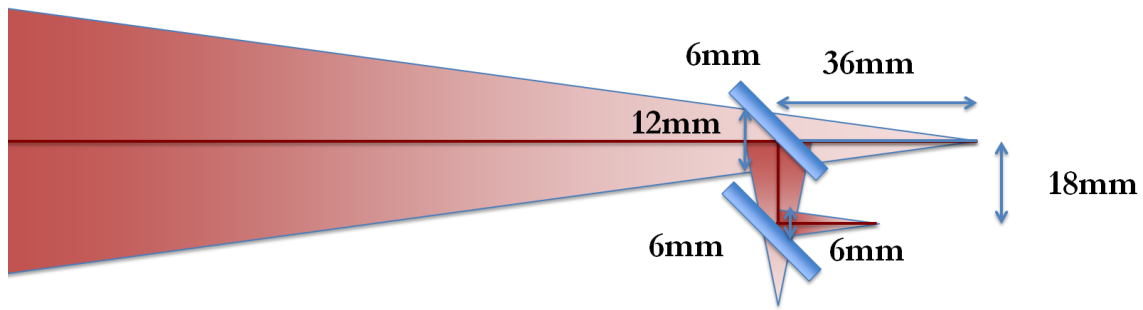


Figure 2: Schematic of the double plasma mirror apparatus utilized to enhance the contrast of the Texas Petawatt laser pulse. The dielectric slides reflected only a small percentage of the incident light until the intensity of the laser was sufficient to ionize their front surface.

### EXPERIMENTAL TIMELINE

Throughout the experimental campaign, multiple diagnostics were utilized during different periods of time in order to accomplish specific objectives. During the first run on the TPW laser in October 2012, a Thomson parabola ion spectrometer and stacks of copper diagnosed laser produced ions. A notable absence of any electron diagnostics during this time left the experimental data set without any measurements of these particles. Shots during this time period were primarily done with plasma mirrors in order to test the feasibility of ion production from ultrathin targets at the TPW facility.

In March 2013 there was a second experimental run, during which the focus was on contrast measurements of the TPW laser pulse. Only a small number of shots were taken on targets during this time, and these were mostly for training purposes. An optical chain was inserted after the laser focus to pick off part of the expanding beam and spatially filter the light before sending it to a third-order autocorrelator. This instrument was used to measure the temporal intensity profile of a number of system shots, both with

and without plasma mirror filtering. Additional measurements by Dr. Erhard Gaul provided a complete picture of the temporal contrast of the TPW pulse.

A third experimental effort in June 2013 was a more mature iteration of the ultrathin target work. The Thomson parabola and stacks of copper were again implemented to detect ions. A full suite of electron spectrometers measured the energy distribution of these particles in an angularly-resolved manner. The emphasis during this experiment was on the irradiation of targets of varying thicknesses. This was accomplished both with and without plasma mirrors, providing a significant amount of data on particles produced under variable experimental conditions.

The final experimental run of this campaign took place in February of 2014. During this effort, the emphasis was on the irradiation of ultrathin targets and the diagnosis of the plasma at the front target surface just before the arrival of the peak of the laser pulse. To this end, targets were irradiated without the use of plasma mirrors during this experiment. Again, the Thomson parabola spectrometer, stacks of copper, and the suite of electron spectrometers were used to detect laser-produced particles.

Complete details about the operation of the diagnostics used in these experiments can be found in the Diagnostics chapter. This chapter also includes information about the data analysis methods applied to obtain meaningful results from measurements with these instruments. The Experimental Results chapter details the outcome of these measurements.

## Chapter 4: Diagnostics

### THOMSON PARABOLA

The main ion diagnostic employed during this work was a Thomson parabola spectrometer. This device, first utilized by J. J. Thomson during his studies of positively charged particle beams, consists of parallel electric and magnetic fields and a detection plate that is sensitive to charged particles [68]. Particles are made incident on this device with an initial velocity that is perpendicular to the direction of the fields. Typically, a collimating pinhole is employed to ensure that all of these particles travel on straight paths through the center of these fields, where they are the most uniform. The dispersion induced by the electric and magnetic forces separates the particles by both energy and charge to mass ratio. Upon leaving the fields, these charged particles travel freely for some distance before they are incident on the detector [68]. The resulting signal consists of a number of parabolic traces corresponding to each distinct charge to mass ratio observed, with particles of different energies incident at different points along their respective curve [68].

As shown below in figure 3, a particle with charge  $q$ , mass  $m$ , and an initial velocity  $v_x$  in the  $x$ -direction will be deflected in the  $y$  and  $z$ -directions by uniform, parallel electric and magnetic fields such as those found in a Thomson parabola spectrometer. The final deflection of this particle due to the electric field is given by:

$$y = \frac{qV_e L}{dmv_x^2} \left( D + \frac{L}{2} \right)$$

where  $L$  is the length of the electric field,  $d$  is the width of this field,  $D$  is the distance from the end of the electric field to the detector, and  $V_e$  is the voltage across the electric field. Similarly, the final deflection of this particle due to the magnetic field is given by:

$$z = \frac{qBL'}{mv_x} \left( D' + \frac{L'}{2} \right)$$

where  $L'$  is the length of the magnetic field,  $d'$  is the width of this field,  $D'$  is the distance from the end of the magnetic field to the detector, and  $B$  is the magnetic induction.

Combing these two expressions, we have:

$$z^2 = \frac{qdB^2L'^2}{V_e L m} \frac{\left( D' + \frac{L'}{2} \right)^2}{\left( D + \frac{L}{2} \right)} y$$

so the resulting trace on the detector can be seen to take the form of a parabola for each observed charge to mass ratio.

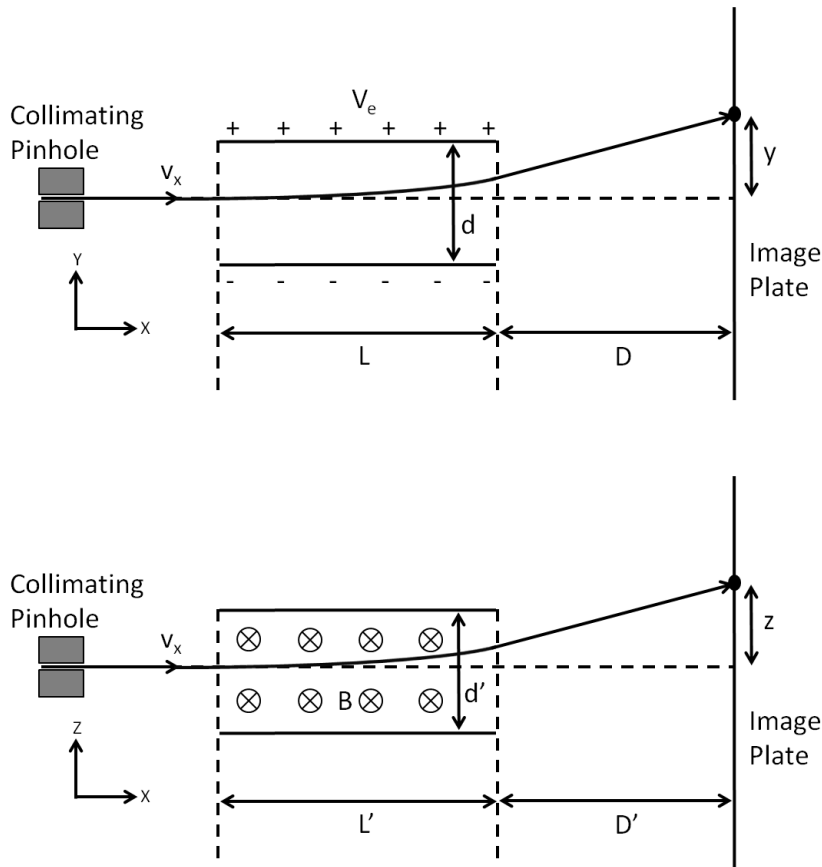


Figure 3: Schematic of the deflection of a charged particle by the parallel electric and magnetic fields in a Thomson parabola spectrometer. The particle is deflected in both directions that are perpendicular to its initial velocity.

In order to accurately measure charged particle spectra using a Thomson parabola, it is essential to design a device that will provide a high energy resolution and an efficient separation of distinct charge to mass ratios at high energies while still providing a sufficient signal level [69]. The energy resolution of the instrument for a given charge to mass ratio is determined by the amount of magnetic dispersion and the size of the ion beam spot on the detector. Greater dispersion due to a stronger magnetic field, greater

field length, or increased drift after the field will increase the resolution of the device, and so will a decreased spot size due to a smaller pinhole [69]. However, a decrease in the pinhole size or an increased drift distance will also decrease the signal on the detector, so it is preferable to increase resolution through the magnetic field parameters. These effects can be quantified by expressing the energy resolution of a Thomson parabola for a particle of charge  $q$  and mass  $m$  at energy  $E$  as the range of energies covered by an ion spot, denoted by  $\Delta E$ , divided by its center energy:

$$\frac{\Delta E}{E} = \frac{2s}{z(1 - (\frac{s}{2z})^2)^2}$$

where  $s$  is the ion spot size and  $z$  is the magnetic displacement given above [69].

While the energy resolution of a Thomson parabola for a given species depends on the magnetic field parameters, the electric field parameters determine the ability of the device to separate particles with distinct charge to mass ratios. Increasing the electric field dispersion by increasing the field strength, lengthening the field, or increasing the drift distance after the field will serve to better separate different traces [69]. Again, it is preferable to increase the field parameters to avoid unnecessary signal loss. For two different ion species of charges  $q_1$  and  $q_2$  and masses  $m_1$  and  $m_2$ , the energies at which the traces overlap can be calculated in terms of the electric field parameters and the ion spot size  $s$ . This is done by finding the energy at which the boundary of one trace overlaps the boundary of the other, where the trace has a thickness given by the ion spot size. The resulting overlap energies can be seen to be:

$$E_i = \frac{q_i EL}{sR} \left( D + \frac{L}{2} \right)$$

$$R = \frac{q_1/m_1 + q_2/m_2}{q_1/m_1 - q_2/m_2}$$

where  $E_i$  is the merging energy for the particle of charge  $q_i$  and mass  $m_i$  [69].

During this experiment, ion data was collected using a Thomson parabola spectrometer designed by Dr. Daniel Jung. It was attached to the experimental target chamber on a flange at 22.5 degrees from target normal at a distance of one meter from the target. Like the experimental chamber, this diagnostic was kept at a high vacuum of  $10^{-6}$  torr. Charged particles propagating to this instrument were first incident on a tungsten block capable of stopping all ions in the energy range observed during this work. A 500 micron diameter pinhole in the center of the tungsten collimated the incident particle beam, providing a solid angle of 0.2 microsteradians. These particles then passed through parallel electric and magnetic fields oriented such that only neutral particles and positively charged ions could reach the detector, while negatively charged electrons and ions were deflected away. After this dispersion, ions travelled freely for some distance and were then incident on a photostimulable image plate. The particles deposited energy on the image plate, which was later read by a scanner to produce digital images of the incident radiation levels, as seen in figure 4. The plate was wrapped in a 25 micron thick layer of kitchen aluminum foil to shield them from x-rays, low energy particles, and heavy ions.

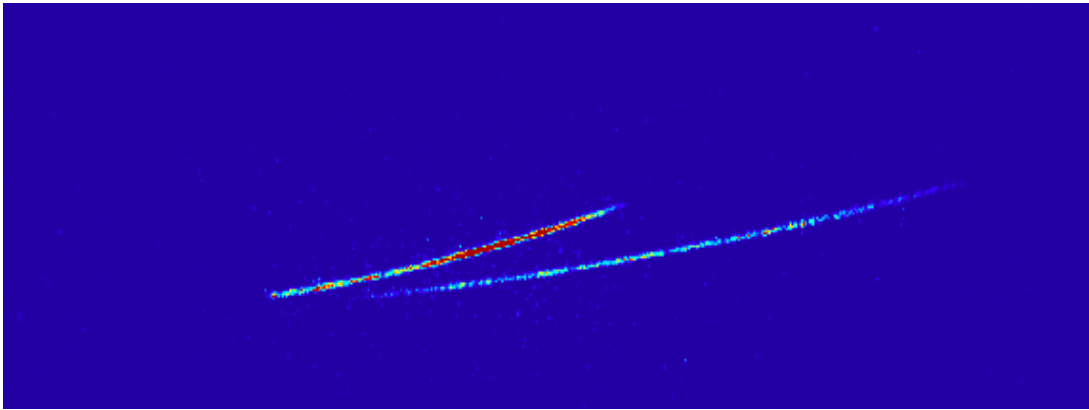


Figure 4: PSL signal level of an image plate from the Thomson parabola spectrometer. Parallel electric and magnetic fields disperse particles by charge to mass ratio and energy. Each species leaves a parabolic trace, with counts from particles of different energies at different positions along the parabola. The traces above correspond to protons and deuterons.

The electric field inside this Thomson parabola was created by a pair of parallel electrodes 330 millimeters long that were separated by 20 millimeters and charged to 10 kilovolts. One of the most difficult parts of operating this instrument involved the prevention of dielectric breakdown inside the device due to this field. Any such breakdown would produce enough x-rays to saturate the detector and obfuscate any ion signal. To prevent this issue, a number of tests were run to determine the maximum field that could be consistently reached without any breakdown. The magnetic field inside the device was provided by a permanent magnet of length 106 millimeters inside a yolk of magnetic steel that helped to minimize fringing effects and ensure that the field was more uniform. Hall probe measurements verified that this field was indeed very uniform across the region of interest, with a magnitude of 0.55 tesla. The distance from the end of the electric field to the image plate detector was 50 millimeters, while the distance from the

end of the magnetic field to the detector was 290 millimeters. The total distance from the pinhole to the detector was 510 millimeters. This configuration resulted in an ion spot size on the detector with a diameter of 753 microns.

When calibrating a Thomson parabola, it is not sufficient to consider only the analytical expressions for the particle deflection stated above. In reality, the fields inside such a device are not perfectly uniform and the incident particles are not perfectly collimated. As such, these expressions provide only an approximation to the true deflection experienced by charged particles as they traverse the instrument. To obtain a more realistic calibration for this Thomson parabola, the true shape of the electric and magnetic fields inside the instrument had to be determined. A calibration of this sort was provided by Dr. Daniel Jung, who supplied a field solver and particle tracker that simulates the passage of ions through the diagnostic. This software provided theoretical signal curves for different values of the relevant parameters of electric field strength, electrode length, magnetic field strength, magnet length, pinhole size, and drift length. A comparison of simulated parabolic traces with real data then allowed for a determination of the ion energy distribution incident on the detector. The accuracy of this calibration method was confirmed by comparing the low energy cut-off of the experimental data with the known ion energy required to punch through the aluminum shielding that covered the image plate detector.

In order to produce an ion spectrum from raw image plate data, the signal was first converted to PSL values (as detailed in the Image Plates section). Next, a reference was identified by locating the zero point, a highly exposed point on the detector caused

by the arrival of undeflected photons collimated by the entrance pinhole. Dr. Jung's particle tracker simulation was then employed to determine the expected shape of the parabolic trace left by protons or other ions of interest. The thickness of this simulated trace was determined by the ion spot size, which was calculated from the other provided parameters. Typically, the simulated trace clearly overlapped the data on the image plate, although small corrections to the angular orientation of the simulated Thomson parabola were sometimes required to ensure agreement. The extent of the simulated trace was then taken as the region of interest (ROI) for the signal on the image plate, as shown in figure 5. At each point along this ROI, the simulated signal was used to determine the ion energy, resulting in data in the form of measured PSL as a function of energy.

Before calculating an ion spectrum from this data, the PSL signal was collected into discrete energy bins. This was done by summing the signal level over discrete, non-overlapping regions within the ROI. These spatial bins were chosen to be the same size as the ion spot on the detector, since details below this scale were not accurately resolved by the diagnostic. The result was bins that were equally spaced along parabolic trace, but non-uniform in energy. The integrated PSL level in each bin was taken as a measure of the total signal at the energy of simulated particles incident at the center of the bin.

In order to determine the background level of the measurement, the same process of spatially binning the measured data was then performed again along another trace, which was the same shape as the first but displaced by the ion spot size. The resulting background values were then subtracted, bin by bin, from the values within the signal

ROI. Finally, the resulting background-subtracted PSL values were converted into particle numbers using the method in the Image Plates section above:

$$\Delta N = \Delta PSL * S * F$$

where  $\Delta N$  is the number of particles in each bin,  $\Delta PSL$  is the total PSL value in each bin,  $S$  is the sensitivity of the image plate detector to ions, and  $F = 0.65$  is the fade time factor (see the Image Plates section for details). The differential spectrum was then calculated using the energy range spanned by each bin, denoted by  $\Delta E$ :

$$\frac{dN}{dE} = \frac{\Delta PSL}{\Delta E} * S * F$$

where  $dN/dE$  is the final differential ion spectrum. If multiple ion species were present, the preceding analysis was carried out independently for each.

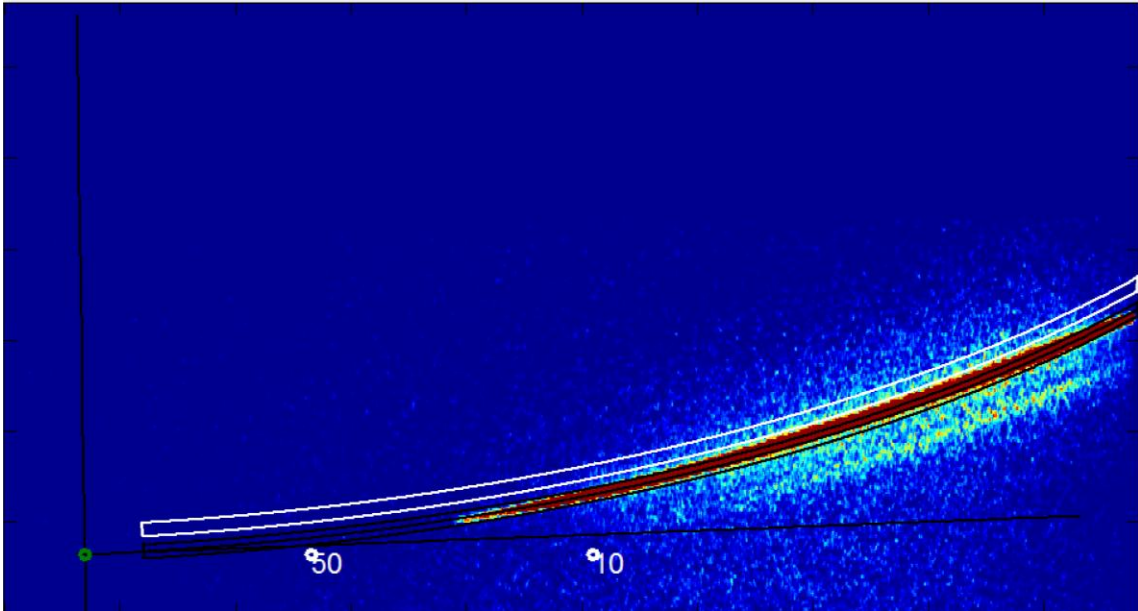


Figure 5: Illustration of the regions selected to calculate a spectrum from raw Thomson parabola data. The green circle indicates the zero point, and the lines coming from it indicate the directions of magnetic and electric deflection. The three black lines along the parabolic trace mark the borders and centerline of the data ROI. Background was measured in the region within the white box.

### ELECTRON SPECTROMETERS

During these experiments, a suite of magnetic electron spectrometers was used to measure the distribution of electron energies. These instruments were capable of measuring energies up to about 18 MeV, and were situated at 10, 15, 50, and 60 degrees from target normal at a distance of 60 centimeters. Particles were collimated at the entrance of each spectrometer by a 1.27 centimeter thick lead shield with a 1 millimeter diameter pinhole, which presented a solid angle of 2 microsteradians. These particles then traversed a 0.49 tesla magnetic field, which they entered in the direction perpendicular to

the field's orientation due to the collimating pinhole. This field was provided by a pair of NdFeB permanent magnets 5.08 centimeters in length separated by 1.27 centimeters. Like the magnets in the Thomson parabola described above, these magnets were placed in yokes of magnetic steel to reduce fringing effects and increase the uniformity of the field. The orientation of the field was such that negative particles were deflected upward, toward an image plate placed on top of the magnets at a height of 13 millimeters above the plane of the pinhole. A schematic of these spectrometers is presented below in figure 6.

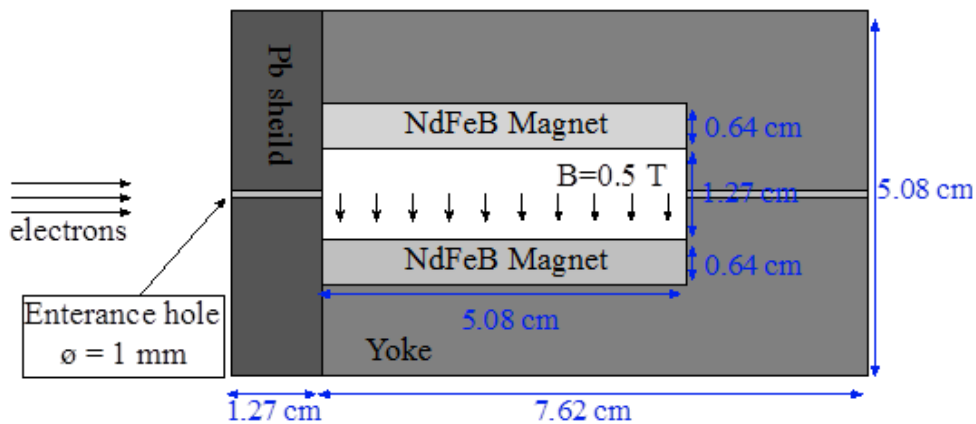


Figure 6: Schematic of the magnetic spectrometers used to measure the angular distribution of electron energies. Electrons were collimated by a small entrance pinhole in a lead shield. They were then deflected toward an image plate detector 13 mm above the plane of the pinhole by two permanent magnets.

In order to determine the energy of particles incident at each point on the image plate, a simple analytical model was derived. It was assumed that a relativistic electron of charge  $e$ , rest mass  $m$ , and energy  $E$  is incident on a uniform magnetic field of magnitude

B. It is deflected toward an image plate at a height  $h$  above its initial position. Relativistic kinematics easily yields the Larmor radius of these electrons to be:

$$R = \frac{mc}{eB} \sqrt{\left(\frac{E + mc^2}{mc^2}\right)^2 - 1}$$

where  $c$  is the speed of light. These particles travel along an arc of a circle with this radius until they reach a vertical displacement of  $h$ , when they are incident on the detector as shown in figure 7. The horizontal displacement of the electron at this time, denoted by  $x$ , can be determined by simple geometry to be:

$$x = \sqrt{R^2 - (R - h)^2}$$

providing a connection between position on the image plate and particle energy.

Expressing the Larmor radius in terms of the particle energy and then solving for this energy, we obtain:

$$E = mc^2 \sqrt{\left(\frac{x^2 + h^2}{2h}\right)^2 \left(\frac{eB}{mc}\right)^2 + 1} - mc^2$$

which gives the desired expression for particle energy as a function of the position that the particles leave signal on the image plate.

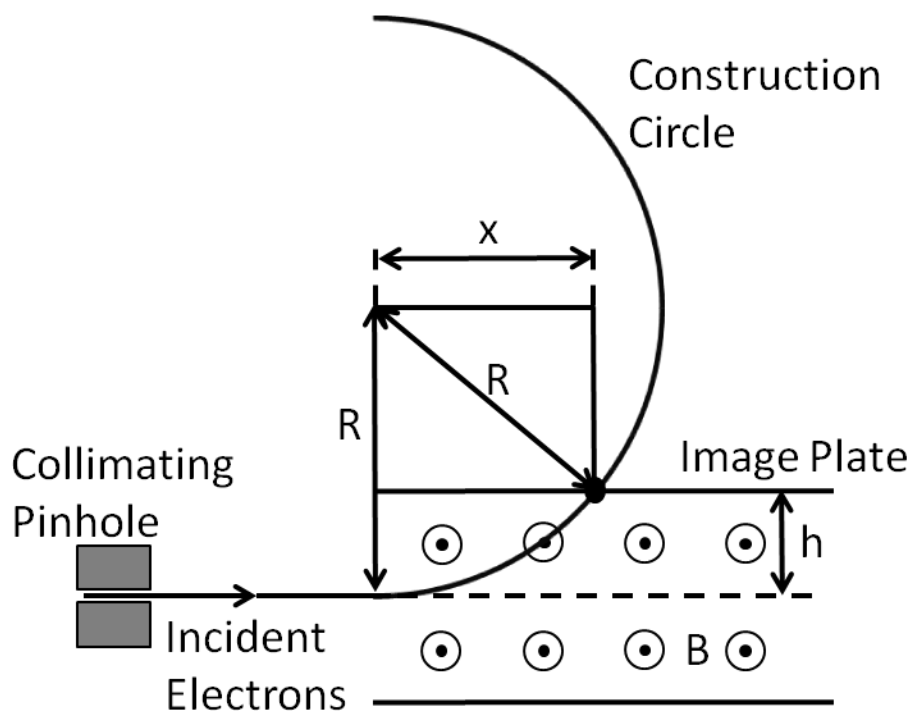


Figure 7: Drawing of the geometry considered to derive the analytical calibration function for the electron spectrometers. Collimated electrons are incident on a uniform magnetic field. They travel on the arc of a circle of radius  $R$  until they intersect with the image plate detector at a height  $h$  above the pinhole. The circle defining the path of the electrons is extended past the image plate for clarity.

In order to confirm the accuracy of this analytical expression, the isotope Sr-90 was implemented as an electron source with a known cutoff energy. Sr-90 undergoes beta decay to Y-90, which is also a beta emitter with a decay energy of 2.28 MeV. Inserting this energy value into the equation above, the model predicts that the beta particles from this decay should cut-off at a horizontal position on the image plate 1.75 centimeters from the pinhole. In order to confirm this prediction, a sample of Sr-90 was placed 3 inches from the pinhole of each electron spectrometer inside the experimental vacuum

chamber. The spectrometers were exposed to electrons produced by this source for four and a half hours apiece. The spectra produced by this experimental calibration process (shown below in figure 8) agree well with the model, verifying the validity of the analytical approach over the relatively small acceptance range of these spectrometers.

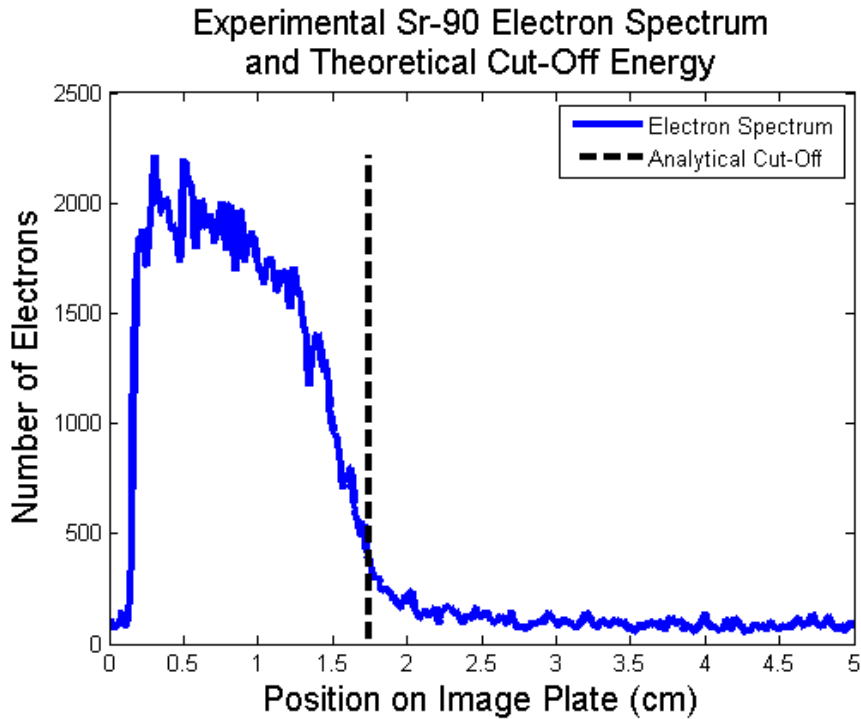


Figure 8: Sr-90 beta decay spectrum as measured by one of the electron spectrometers is shown in blue. The characteristic cut-off energy for electrons produced by a Sr-90 source is 2.28 MeV. The analytical model relating electron energy to position on the image plate that this cut-off should be at 1.75 cm from the instrument's pinhole, as shown by the vertical dashed line. The analytical model is in good agreement with the experimental data.

Given this calibration function, the analysis of the image plate scans from these electron spectrometers began with an identification of the signal region of interest (ROI). The size of the thin electron trace in the direction orthogonal to the energy dispersion was

taken as the height of the region of interest, while the width of this region was taken to cover electron energies from 3 MeV to 17 MeV. This range was chosen to exclude signal from high energy particles at the edge of the image and from low energy particles that were deflected to extreme angles inside the spectrometer. The PSL values for points within the region of interest were calculated from the raw data using the method described in the Image Plates section, and these values were summed along the vertical spatial dimension after background subtraction.

A measurement of the background signal level was obtained by choosing a second region well separated from the signal ROI. This background region was taken to have the same horizontal extent as the ROI, with a vertical height of ten pixels. The average background PSL value over the vertical dimension was then calculated at each horizontal position, giving an energy-dependent measure of the experimental noise level. The corresponding background level was then subtracted from each pixel in the data ROI to complete the background subtraction process. Below, figure 9 shows PSL levels recorded on a system shot by one of these spectrometers, with the signal and background regions indicated.

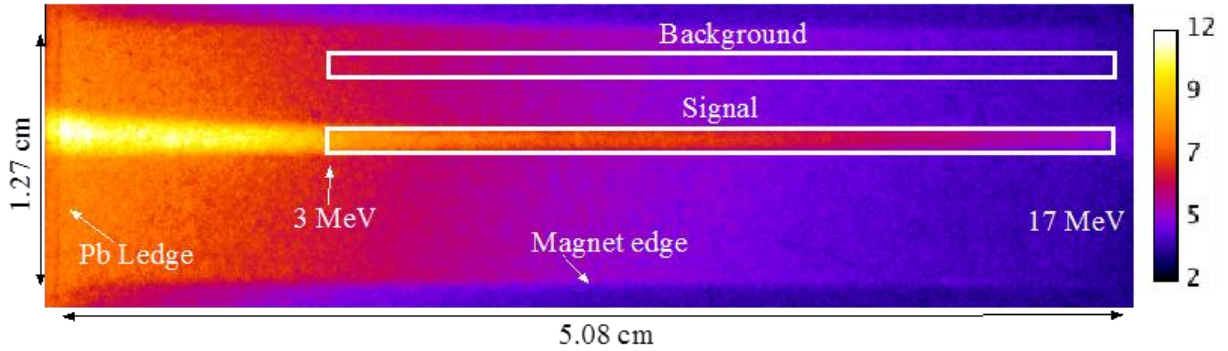


Figure 9: PSL signal level of an image plate from the small electron spectrometers. The energy dispersion of the instrument is in the horizontal direction, while the vertical direction is a spatial dimension. The yellow rectangle indicates the region of interest on the image plate, while the red rectangle indicates the region used for a determination of the background signal level.

After background subtraction, the x-axis of the image was then organized into bins of 25 pixels each, with the PSL values of the data in each bin summed up to give a total for the bin. The energy of the electrons contributing signal to each bin was then determined by applying the calibration curve at the midpoint of the bins. This process resulted in bins that were uniformly distributed in space, but non-uniform in energy. The number of electrons in a given energy bin, denoted by  $\Delta N$ , was then determined from the binned PSL values using the method described in the Image Plates section above:

$$\Delta N = \Delta PSL * S * F$$

where  $\Delta PSL$  is the total PSL signal value in each bin,  $S = 0.007$  is the sensitivity of the image plate detector to electrons, and  $F = 0.65$  is the fade time factor (see the Image Plates section below for details). The differential spectrum was then calculated using the derivative of the energy calibration curve, denoted by  $dE/dx$ :

$$\Delta E = \frac{dE}{dx} \Delta x$$

$$\frac{dN}{dE} = \frac{\Delta PSL}{\Delta E} * S * F$$

where  $\Delta x$  is the size of each bin in space,  $\Delta E$  is the energy range covered by a bin, and  $dN/dE$  is the final differential electron spectrum.

### **IMAGE PLATES**

The image plate detectors utilized in the electron and ion spectrometers were produced by FujiFilm, and operate on the principle of photostimulable luminescence. The active phosphor layer in these plates is composed of barium fluorobromide crystals with a 5 micrometer grain size containing small amounts of bivalent europium [70]. Exposure to radiation such as x-rays, electrons, positrons, or ions excites electrons from europium to the conduction band, where they are trapped in metastable color centers. Secondary exposure to visible light re-excites these electrons, which relax to the valence band and emit light at 390 nanometers [70]. These detectors are ideal for measurements of laser produced radiation due to their insensitivity to EMP noise and their high dynamic range ( $\sim 10^5$ ) and resolution compared to standard film [70] [71].

After exposure to radiation, these image plates were read using a FLA-7000 scanner produced by FujiFilm. This device exposes the plate using a HeNe laser and collects the secondary luminescence using a photomultiplier tube (PMT) [70]. The output of this PMT is amplified and stored on a logarithmic scale in a digital image [72]. Linear photostimulated luminescence (PSL) values can be retrieved using the formula:

$$PSL = \left(\frac{res}{100}\right)^2 \frac{4000}{S} 10^{L\left(\frac{QL}{65535} - \frac{1}{2}\right)}$$

where the scan parameters are described by the variables *res* for resolution, *S* for sensitivity, *L* for latitude, and *QL* for the raw signal on the log scale [72]. These calculated PSL values are directly related to the amount of radiation incident on the detector [70]. After scanning, image plates are easily erased for further use by exposure to white light.

The radiation exposure of the image plates was then determined by making use of independent calibration data relating PSL values to the number of incident particles. For electrons, the sensitivity of these image plates is a sharp function of particle energy for incident particles below about 1 MeV, but the curve flattens to a value of 0.007 PSL per electron for particle energies from 1 MeV to 100 MeV [73]. In addition, the decay of the image plate signal as a function of time after exposure must be taken into account. Calibration curves also exist describing this signal loss, and the ten minutes between each laser system shot and the electron image plate scans introduced another factor of 0.9 to account for this effect [73].

For protons, the response of the image plates is a more complicated function of energy. Nevertheless, two sets of independent calibration data for protons exist, with the first data set extending from 0.6 MeV to 3.4 MeV [74]. This set of calibration data was collected at the SUNY Genesco 1.7 megavolt Pelletron accelerator, which is capable of delivering well calibrated monoenergetic particle beams [74]. The particles produced by this instrument were recorded using a BAS-TR image plate, which was read using a FUJI

FILM BAS-1800 II scanner. The results include fifteen data points indicating a sensitivity between 0.10 and 0.15 PSL per proton, with a distinct maximum at a particle energy of about 1.1 MeV [74].

The second independent set of calibration data was collected across a range of particle energies from 0.5 MeV to 20 MeV using BAS-TR 2025 image plates and a FUJI FILM BAS-1800 II scanner. This calibration was determined by simultaneously exposing an image plate and calibrated RCF and CR-39 detectors to laser produced protons [75]. The resulting 26 data points indicate a sensitive between 0.01 and 0.23 PSL per proton, with a maximum at an energy of about 1.5 MeV [75]. Three fitting functions are provided that approximate the shape of this calibration curve for different energy ranges. For energies (denoted E) up to 2.11 MeV, the conversion factor is:

$$\frac{PSL}{\# \text{ of Protons}} = 0.22039 * \exp(-(E - 1.5049)^2 / (1.1842^2)). [75]$$

For energies (E) from 2.11 MeV to 20 MeV, the equivalent factor is:

$$\frac{PSL}{\# \text{ of Protons}} = 0.33357E^{-0.91377}. [75]$$

It is likely that the disagreement between these two calibrations is due to the different experimental conditions under which the data was collected.

When determining the number of protons recorded by image plates in the ion spectrometer during this series of experiments, both of these calibrations were considered. For low energy particles from 0.6 MeV to 3.6 MeV, the average of the two data sets was used, with the range between the two results indicating the uncertainty of the sensitivity factor. For the energy range between 3.6 MeV and 20 MeV, the fitting

function given above for these energies was utilized. For energies above 20 MeV, no calibration data is available and a flat conversion factor of 0.02 PSL per proton was used in lieu of an sensitivity curve for this range. In all cases, a factor of 0.65 was used to account for the twenty minutes required to scan the image plates after a system shot.

#### **ACTIVATION STACKS**

Further determinations of proton energies and proton beam shapes were accomplished through the use of copper activation stacks and radiochromic film (RCF). The copper activation stacks consisted of 18 millimeter thick stacks made of 9 individual 2 millimeter thick copper plates placed 10 millimeters downstream from the primary target. The copper plates in these stacks had a natural abundance of isotopes, with  $^{63}\text{Cu}$  making up 69.17% of the material and  $^{65}\text{Cu}$  making up 30.83%. They were wrapped in a layer of 25 micrometer thick aluminum foil to stop electrons, low energy photons, and heavy ions. A schematic showing the position of these stacks in relation to the target and the other particle diagnostics is shown below in figure 10.

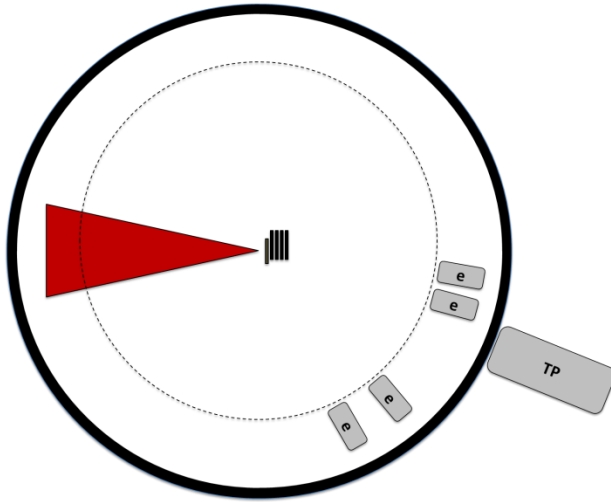


Figure 10: Schematic of the particle diagnostics utilized in the experimental target chamber. Electron spectrometers, labeled e, were positioned 60 cm from the target at  $10^\circ$ ,  $15^\circ$ ,  $50^\circ$ , and  $60^\circ$ . A Thomson parabola ion spectrometer was connected to the target chamber 1m from the target at  $22.5^\circ$ . Activation stacks of copper or radiochromic film and CR-39 were often placed directly in front of the target at a distance of 10 millimeters.

Upon irradiation of the primary laser target, energetic particles were produced which transmuted the copper nuclei in these stacks to radioactive isotopes through various nuclear reactions. These activated copper plates were then used to expose image plate detectors for twenty minutes, during the period from ten to thirty minutes after each system shot. The resulting signal was a measure of the radioactivity induced in the stack as a function of position on the plate and depth in the stack. Since particles of different energies and different species are stopped at different depths in the stack, this results in a spatially and spectrally resolved measurement of the particles produced by the primary laser-matter interaction [76].

Protons, photons, and neutrons can all be produced by the irradiation of a solid target with an ultrahigh intensity laser, and all of these particles can in turn induce nuclear reactions in copper. However, the threshold energy of the particles inducing the reaction, the cross section for the reaction, and the half-life of the resultant daughter nuclei vary widely in these reactions, as shown in table 1 [77]. Taking these properties into account, it is clear that  $^{63}\text{Zn}$  and  $^{62}\text{Cu}$  were the dominant sources of radioactivity during the time in which the image plates were exposed to the activated copper [77]. This was confirmed by Geiger counter measurements of the copper's radioactivity taken every ten minutes for a period of one hour after two shots. By fitting these measurements to an exponential decay, the half-life of the signal was measured to be 9.7 minutes in one case and 38 minutes in another case. The transition between these two results demonstrated a significant change in the primary laser-matter interaction, as explained in the Results section.

Reaction Channel	Reaction Threshold (MeV)	Max Cross Section (mb)	Decay Half-Life of Daughter Nuclei	Fraction that decay in time 10 min < t < 30 min
$^{63}\text{Cu}(p,2n)^{62}\text{Zn}$	13.26	135	9.1 hr	2.48%
$^{63}\text{Cu}(p,n)^{63}\text{Zn}$	4.149	500	38.4 min	25.30%
$^{63}\text{Cu}(p,p+2n)^{61}\text{Cu}$	19.74	323	3.3 hr	6.53%
$^{65}\text{Cu}(p,n)^{65}\text{Zn}$	2.13	760	244 days	0.00%
$^{65}\text{Cu}(p,p+n)^{64}\text{Cu}$	9.91	490	12.7 hours	1.79%
$^{63}\text{Cu}(\gamma,n)^{62}\text{Cu}$	10.8	68	9.7 min	37.22%
$^{63}\text{Cu}(\gamma,2n)^{61}\text{Cu}$	19.7	12	3.3 hours	6.53%
$^{65}\text{Cu}(\gamma,n)^{64}\text{Cu}$	9.9	75	12.7 hours	1.79%
$^{63}\text{Cu}(n,2n)^{62}\text{Cu}$	14	454	9.7 min	37.22%

Table 1: Nuclear reactions induced in  $^{63}\text{Cu}$  and  $^{65}\text{Cu}$  by protons, photons, and neutrons. The threshold energy of the incident particles, the maximum cross section of the reaction, and the half-life of the resulting nuclei all vary widely.  $^{63}\text{Zn}$  and  $^{62}\text{Cu}$  can be seen to dominate the induced radioactive signal during the period of time from ten to thirty minutes after the reaction [77].

RCF and CR-39 were also utilized as spatially-resolved ion diagnostics, by virtue of the physical changes induced in these materials upon their exposure to radiation. More specifically, RCF changes color to dark blue when exposed to ionizing radiation because of an induced polymerization reaction [78]. The most commonly utilized type of RCF is sold under the trademarked name "Gafchromic film" in a number of varieties that differ in sensitivity [78]. This film requires no additional fixing or processing to reveal the radiation signal, which is quite stable over long time periods [78].

The induced color change in RCF is dependent on the absorbed radiation dose, with darker colors corresponding to a greater exposure. As such, information about the incident radiation pattern is encoded in the spatial distribution of the optical density of the

film [78]. The spatial resolution of this optical density signal can be quite good, with published RCF radiation measurements in the medical literature claiming to have resolved features as small as 1200 lines per millimeter [78]. Once the film has been exposed, the distribution of the optical density can be measured and digitized using a transmission densitometer, spectrophotometer, or film scanner [79]. While the color change of the RCF is mostly complete within milliseconds of exposure, there is residual darkening that continues for up to 24 hours. As such, it is important to wait at least one day before analyzing exposed film [79].

Once the raw signal from an RCF diagnostic has been recorded, the energy deposited by incident particles can be determined using a calibration curve that relates the optical density of the exposed film to the absorbed radiation dose [80]. Unfortunately, the manufacturer of this film has been known to change the properties of their product, and variations in response have even been measured for different batches of the same film [78] [80]. Therefore, it is preferable to produce an independent calibration for each batch of RCF if a highly accurate measurement is desired [79]. In addition, the response of the scanner used to read the film must also be accounted for in the data reduction process [79].

The use of Gafchromic film is widespread in medical applications, and various groups have demonstrated its use as a diagnostic of laser-accelerated protons [49] [80] [79]. In this context, RCF is commonly implemented in a stacked configuration with a material of known stopping power [49] [79]. In analogy with the copper stack diagnostic described above, the exposure of pieces of film at different depths is then caused by

protons of different energies. The result is a spatially-resolved measurement of the proton spectrum [49] [79].

During the work described by this thesis, RCF was used as a qualitative diagnostic of the ion beams produced by the laser-target interaction. It was placed in 18 millimeter stacks made up of alternating layers of RCF and optical-quality plastic, with RCF in the first layer. Like the copper stacks described above, these were wrapped in a layer of 25 micrometer thick aluminum foil to stop electrons, low energy photons, and heavy ions. They were placed in the same position as the copper stacks shown above in figure 10, at a distance of 10 millimeters downstream from the target. After each shot with one of these RCF stacks in place, the films were visually inspected to determine if an ion beam had been produced. Proton spectra were not calculated from the RCF signal, as the Thomson parabola provided a better method for diagnosing these particles. After inspection, each piece of film was then photographed and cataloged.

### **THIRD-ORDER AUTOCORRELATOR**

Measurements of the temporal intensity profile of the Texas Petawatt laser pulse were accomplished using a single-shot third-order autocorrelator. For ultrashort pulses, this type of measurement is notoriously difficult to accomplish, as there are no conventional diagnostics capable of resolving the relevant timescale. The problem is compounded in ultrahigh intensity glass systems that operate at very low repetition rates, as it becomes necessary to measure the complete temporal profile in a single shot. Generally, measurements of this kind employ another ultrashort reference pulse to interact with the original pulse in a nonlinear medium, resulting in a signal that yields

time-resolved information about the pulse shape. This reference pulse is often a copy of the original pulse obtained by splitting its amplitude through partial transmission and reflection. The resulting signal then takes the form of correlation functions between the original pulse and its harmonics.

The simplest case of such an instrument, known as an autocorrelator, is the second-order device, which was first demonstrated in 1979 [81]. In this instrument, an optical pulse is overlapped with a copy of itself, possibly delayed in time, in a nonlinear crystal oriented for noncollinear second harmonic generation. If the original pulse has a temporal intensity profile given by  $I(t)$ , second harmonic light is produced in the crystal with a time-integrated intensity proportional to the second-order autocorrelation function:

$$A_2(\tau) = \int_{-\infty}^{\infty} dt I(t) \cdot I(t + \tau)$$

where  $\tau$  is the time delay of the reference pulse relative to the original pulse.

In order to recover the desired pulse duration from the second-order autocorrelation function, it is sufficient to measure the total time-integrated intensity of the second harmonic light as the delay between pulses is varied [82]. Experimentally, this is accomplished by sending one beam down an optical delay leg of adjustable length that is controlled by the position of a micrometer and recording the intensity of the resulting second harmonic light with a photodetector. Unfortunately, this method is not suitable for low repetition rate systems because it requires a number of shots to determine the pulse duration. Alternatively, the same information can be determined by making a spatially resolved measurement of the second harmonic light produced in the autocorrelator [82].

Since the two pulses cross at an angle in the nonlinear medium, they interact with a different effective delay time at each transverse position in the interaction plane across the crystal [81]. By imaging the interaction region onto a camera, this spatial variation of the effective time delay can be exploited to measure the complete autocorrelation function in a single-shot on low repetition rate systems.

Unfortunately, the second-order autocorrelation function is not sufficient to recover the complete temporal intensity profile of the original laser pulse [83]. This function is symmetric in its argument about  $\tau = 0$ , so it is not possible to distinguish pre-pulses from post-pulses using a second-order autocorrelator. This is a serious limitation, as pre-pulses are much more significant for a solid target experiment than post-pulses. In addition, the process of direct conversion of fundamental light from a single pulse to second harmonic light generates significant background signal when the second-order method is employed [83]. This limits the dynamic range of the resulting measurement to about  $10^5$ , presenting an obstacle for experimentalists that need to resolve the  $10^{10}$  contrast required for many interaction scenarios [83].

In order to bypass these difficulties, third-order autocorrelators are often utilized to make temporal intensity measurements that require a high level of sensitivity. This more complex device utilizes two nonlinear processes to produce a signal at the third harmonic of the input frequency [83]. First, the original input pulse with intensity profile  $I(t)$  has its amplitude split, as in the second-order autocorrelator, resulting in two copies of the same pulse. One of these pulses is then focused onto a frequency doubling nonlinear crystal, producing second harmonic light with an intensity profile proportional

to  $I^2(t)$  [83]. This second harmonic pulse, which may be delayed in time relative to the fundamental, is then overlapped with the fundamental pulse in another nonlinear crystal oriented for sum frequency generation [83]. The resulting signal at the third harmonic frequency can be separated from noise at the second harmonic through the use of optical filters, allowing for measurements with a dynamic range approaching  $10^{10}$  [83]. In analogy with the second-order device, this device produces third harmonic light with a time-integrated intensity proportional to the third-order autocorrelation function:

$$A_3 = \int_{-\infty}^{\infty} dt I^2(t) \cdot I(t + \tau)$$

where  $\tau$  is again the time delay between the two pulses [83].

It has been shown mathematically that the third-order correlation function contains all the information necessary to completely reconstruct the temporal profile of the laser pulse [84]. This can be done by measuring the spatially-integrated intensity of the autocorrelation signal as a function of the time delay between the two pulses [83]. As in the second-order case, this requires too many shots to be practical for systems with a low repetition rate. Again, this limitation can be circumvented by overlapping the two beams in the second crystal at some angle, mapping different time delays to different transverse positions in the interaction plane [85]. Spatially-resolved measurements of the third harmonic signal, made by imaging the overlap region to a camera, then provide the complete autocorrelation function.

Alternatively, the prohibitive phase matching requirements of noncollinear sum frequency generation can be avoided by introducing a pulse front tilt to one of the two

pulses in an autocorrelator [86]. A beam is said to possess pulse front tilt when the constant amplitude pulse fronts are inclined at some angle to the beam's propagation direction [87]. In this scenario, the arrival of the pulse varies in time over its cross-section. This can be caused by an angular dispersion of the frequency components of the pulse, which is easily affected with a diffraction grating [87]. In the context of autocorrelation measurements, a pulse front tilt maps time delay to transverse position across the interaction region in the nonlinear medium without the need for an extreme crossing angle [86].

This type of single-shot third-order autocorrelator was utilized to make measurements of the temporal intensity profile of the Texas Petawatt laser pulse. Input light at the fundamental frequency was first split into two identical pulses by a 50-50 beamsplitter, which directed the two pulses to distinct legs of the device. One leg contained an adjustable delay stage that was traversed by fundamental light, with a micrometer for precise control of the optical path length. The other leg included a nonlinear crystal oriented for type I second harmonic generation that produced a pulse at twice the input frequency. This second harmonic pulse was then directed to a diffraction grating, which introduced a pulse front tilt. These two legs were then combined and imaged onto another nonlinear crystal oriented for type II sum frequency generation (SFG), producing a third harmonic signal. All light with frequencies below the third harmonic was then filtered, and the source of the remaining light was imaged onto a 16-bit cooled Andor camera.

The tilted wavefronts in the second harmonic leg of the device mapped contrast information at different times to different spatial positions on the CCD chip within the camera. An analysis of the image recorded by the camera after a shot then provided a means of determining the intensity of the pulse as a function of time over a period of just over 10 picoseconds. Different windows of time could be observed by adjusting the optical path length in the fundamental leg by means of the delay stage. A schematic of the third-order autocorrelator is shown below in figure 11.

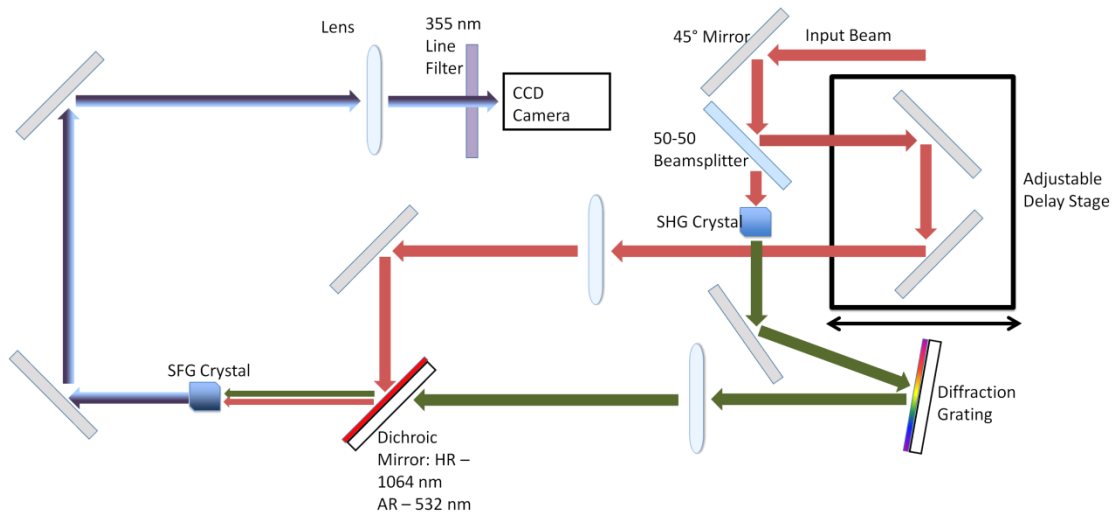


Figure 11: Schematic of the third-order autocorrelator used to measure the contrast of the TPW laser pulse. Fundamental light traversed one leg of the instrument, while frequency doubled light passed along the second leg and acquired tilted wavefronts after reflection from a grating. Light from each leg was overlapped in a nonlinear crystal to produce third harmonic light, which was imaged onto a camera.

Light was delivered to the third-order autocorrelator by means of a pick-off system in the experimental target chamber. A mirror sampled the diverging TPW beam after its focus, reflecting a small portion of the wavefront. This diverging beam was then

collimated and passed through a spatial filter to improve its wavefront quality. The pulse then passed through a window out of the target chamber toward a table that held the diagnostic.

In order to ensure that the camera in the autocorrelator was not saturated, various neutral density (ND) filters were included before the entrance aperture to the device. Each unit of optical density introduced by these ND filters cut the power of the transmitted light into the autocorrelator by one order of magnitude. Since the output of a third-order autocorrelator is produced by two nonlinear processes yielding the third harmonic, the signal on the camera was reduced by a factor of  $10^{-3}$  per unit of optical density introduced in this location. ND filters were also placed with the infrared leg of the autocorrelator for finer control the output signal level. The light intensity in this leg of the diagnostic is directly proportional to the resulting signal, so each unit of optical density decreased the camera exposure by a factor of only  $10^{-1}$ .

The single-shot design of the third-order autocorrelator maps interaction time in the SFG crystal to space. This produces a signal on the camera that varies horizontally across the image according to the time argument of the autocorrelation. The conversion between pixels on the camera and time was determined by inserting a glass slide of known thickness into the IR leg of the diagnostic and measuring the horizontal shift of the resulting signal on the camera. The result of this measurement indicated that the autocorrelator had a resolution of 86 femtoseconds per pixel. In order to determine the length of the time window measured on each shot, signal from the main peak of the TPW pulse was observed at 10 hertz on the camera using only the OPA stage of laser

amplification. The delay stage in the infrared leg of the device was then adjusted, changing the interaction time and translating the signal on the camera. The signal level began to fall off at clear horizontal positions on the image, indicating each edge of the instrument's acceptance. Using this method, it was determined that the diagnostic was capable of recording an 11.18 picosecond window on each shot.

Unfortunately, excessive noise in the system limited the dynamic range of the third-order autocorrelator contrast measurements to about  $10^3$  on each individual shot. This is significantly less than the magnitude of variations in the laser intensity profile, which may be  $10^{10}$  over tens of picoseconds. Therefore, the optical density of the filters in the system had to be adjusted as the observation window of the autocorrelator was scanned in time using the delay stage. For each measurement, the optical density of the filters was chosen to provide the greatest possible signal level that would not saturate or damage the camera. Since a 16-bit camera was utilized for these measurements, the maximum signal before saturation was a value of  $2^{16} = 65536$  per pixel.

It is illustrative to walk through an example of the filter and delay stage adjustments required to collect contrast data with the third-order autocorrelator over a wide range of times and intensities. First, the OPA beam was sent to the device at 10 hertz with no filters in the system and the delay stage was adjusted until the main peak was visible on the camera. Then, a relatively large optical density was introduced before the device and the autocorrelation signal from the most intense part of the pulse profile near the main peak was measured on a system shot. After these measurements, the unfiltered OPA beam was again utilized for make delay adjustments to move the main

peak out of the temporal observation window and make observations at earlier instants of time. Previously, the less intense features at these times were buried in the noise of the heavily filtered measurements of the main peak. Now that the main peak was outside of the instrument's acceptance window, the optical density of the filters was safely decreased in order to enhance the signal level and collect data on the lower intensity features. Adjustments of the filters were made anytime the temporal window was adjusted, and extra filters were introduced to prevent camera damage if there was any uncertainty about the expected signal level. In these cases, the signal was then increased in a controlled manner until it reached the optimal level.

The first step in processing an autocorrelator image was determining the region of interest (ROI). This was accomplished by cropping the image horizontally to include only the 11.18 picosecond acceptance window described above and cropping the image vertically at the point where the signal level from the main peak began to decrease. A background region was then defined by selecting a section of the image that was the same size as the ROI and covered the same horizontal range, but began at the top edge of the image. The signal levels in both the ROI and this background region were averaged over the vertical dimension, resulting in a signal and background value for each pixel along the horizontal direction. The difference between these two values was then calculated at each position, resulting in a background-corrected intensity level at each horizontal point, or instant of time.

Once this background subtraction process was completed, the signal was corrected to account for the variable intensity level of the light in the autocorrelator. The

different power provided by each laser shot was divided out using measurements from the TPW diagnostic package. The signal was also divided by additional powers of ten to account for the optical density of the filters in the system. The attenuation factor due to filters before the autocorrelator was cubed to account for the dependence of the instrument's signal on the incident light intensity. On the other hand, the attenuation factor introduced by filters in the infrared leg of the device was directly proportional to the attenuation of the resulting signal. This normalization process gave a final measured intensity value of:

$$I = S * PD / (E * 10^{3*ND} * 10^{ND_{IR}})$$

where  $S$  was the background corrected signal level,  $PD$  was the laser pulse duration for the system shot,  $E$  was the laser pulse energy,  $ND$  was the optical density of the filters before the autocorrelator, and  $ND_{IR}$  was the optical density of the filters in the infrared leg of the instrument.

If the main peak of the pulse was within the time acceptance of the autocorrelator on a given shot, the signal level at this maximum was normalized to unity. On the other hand, if the shot was part of a scan in which the diagnostic was measuring a period of time before the main pulse, then a reading from a different shot was used to normalize the intensity. By adjusting the amount of filtering in the diagnostic, different periods of time with different intensity levels were measured by this instrument. Multiple shots were then combined to obtain a complete intensity profile of the TPW laser pulse. An example of the data collected by this diagnostic is pictured below in figure 12.



Figure 12: Raw signal level from a measurement of a system shot of the Texas Petawatt laser using the third-order autocorrelator. The instrument maps time onto the horizontal axis, while the vertical axis is a spatial dimension. The bright region indicates the main peak of the laser pulse.

### **PROBE BEAM AND INTERFEROMETER**

As a part of this experiment, a probe beamline was utilized to diagnose the pre-plasma density profile at the front target surface using interferometry. Measurements of the properties of such a laser-produced plasma are difficult to obtain because the plasma is localized to a micron-scale region and its properties, such as density, evolve on extremely short time scales [88]. These considerations, along with the relatively slow response of most electronic systems, make the implementation of many standard plasma diagnostics, such as Langmuir probes, problematic for performing these density measurements [88]. In principle, spectroscopic methods could be utilized to measure the width of spectral lines emitted by the plasma, which increase in proportion to the  $2/3$  power of the ion density due to Stark broadening [27]. These plasma density measurements could even be made in a time-resolved manner, through the use of a streak camera or gated imaging system. Unfortunately, strong emission of continuum radiation from laser-produced plasmas makes these measurements difficult, and the high resolution necessary to measure line widths in a time-resolve manner with sufficient accuracy makes this type of diagnostic very expensive [88].

Another class of techniques employs ultrashort probe laser beams to make density measurements of laser-produced plasmas on the relevant timescales. Free electrons in a

plasma scatter infrared and visible electromagnetic radiation through the classical process of Thomson scattering. The fraction of scattered light, denoted by  $I/I_0$ , is dependent on the plasma density  $n_e$ , the Thomson cross-section  $\sigma$ , and the plasma scale length  $L$  by:

$$I/I_0 = L\sigma n_e$$

Therefore, a measurement of the amount of light scattered by a plasma from a probe beam of known intensity will yield information about the plasma density [27]. Unfortunately, the Thomson scattering cross-section is extremely small at  $\sigma = 6.65 \times 10^{-29} \text{ m}^2$ , making these measurements very difficult in practice [88].

A more practical method of making density measurements of laser-produced plasmas is based on the use of interferometric methods to determine the plasma's refractive index. In this process, coherent electromagnetic waves from a probe laser are superimposed to obtain phase information in the form of bright and dark interference fringes. In an amplitude-splitting interferometer such as the common Michelson design, a single beam is split using a partially reflective optical element and the two legs are then recombined and made incident on a detector, causing interference and producing fringes. In order to diagnose the density of a plasma, a reference must first be taken by recording the interference pattern produced by the interferometer in the absence of the plasma. Then, the device is used to overlap undisturbed light with probe light that has passed through the plasma under interrogation. A relative phase shift due to the plasma causes a change in the interference signal relative to the reference, and this difference provides information about the plasma's index of refraction.

The total phase shift of the probe beam relative to the reference at each point of its cross-section provides a measure of the total amount of plasma encountered by each portion of the beam. As detailed in the Laser-Produced Plasma background section, the index of refraction, denoted by  $n$ , of a plasma with electron density  $n_e$  is given at frequency  $\omega$  by:

$$n = \sqrt{1 - \frac{\omega_p^2}{\omega^2}}$$

where  $\omega_p$  is the plasma frequency. This quantity is given by:

$$\omega_p = \sqrt{\frac{n_e e^2}{\epsilon_0 m_e}}$$

where the other relevant factors are the charge of the electron, denoted by  $e$ , the permittivity of free space, denoted by  $\epsilon_0$ , and the mass of the electron, denoted by  $m_e$ . If the probe beam propagates in the  $z$ -direction through a plasma with a spatially-varying extending from  $z = z_0$  to  $z = z_f$ , then the phase shift due to this plasma at each point of the beam's cross-section is given by:

$$\varphi(x, y) = \int_{z_0}^{z_f} dz [n(x, y, z) - 1] \frac{\omega}{c}$$

where  $\omega$  is the probe beam frequency and  $c$  is the speed of light.

After interaction with the plasma, the probe beam is then directed to the interferometer. The phase shift given above causes a change in the observed interference pattern relative to the reference produced in the absence of the plasma. This provides a measure of the plasma density encountered by the probe that is integrated along the

beam's propagation direction, but spatially-resolved in the transverse dimensions. The time resolution of the measurement is limited by the pulse duration of the probe beam. As such, laser-produced plasmas must be interrogated by ultrashort probes to resolve the relevant dynamics. It is important to note at this point that light will only propagate through a plasma if the index of refraction remains real, so this type of interrogation will only work with sufficiently diffuse plasmas traversed by light of sufficient frequency.

During the experiments described in this paper, density measurements of the target pre-plasma a short time before arrival of the main laser pulse were performed using this method. To this end, a small amount (~10 millijoules) of the energy of the TPW laser was picked off after the stretcher and first OPA stage and sent through a delay line of variable length, allowing for control of the relative timing between this pulse and the main beam. This probe pulse was compressed to about 500 femtoseconds using a single grating compressor at ambient conditions in the TPW laser bay. To enable propagation through denser plasma, the beam was then frequency doubled before being passed through a window into the experimental target chamber. Inside the chamber, an iris was used to select the most uniform part of the beam profile, resulting in a beam with a one millimeter diameter. This beam was then sent vertically along the target surface such that one edge of the beam passed through the target pre-plasma on system shots.

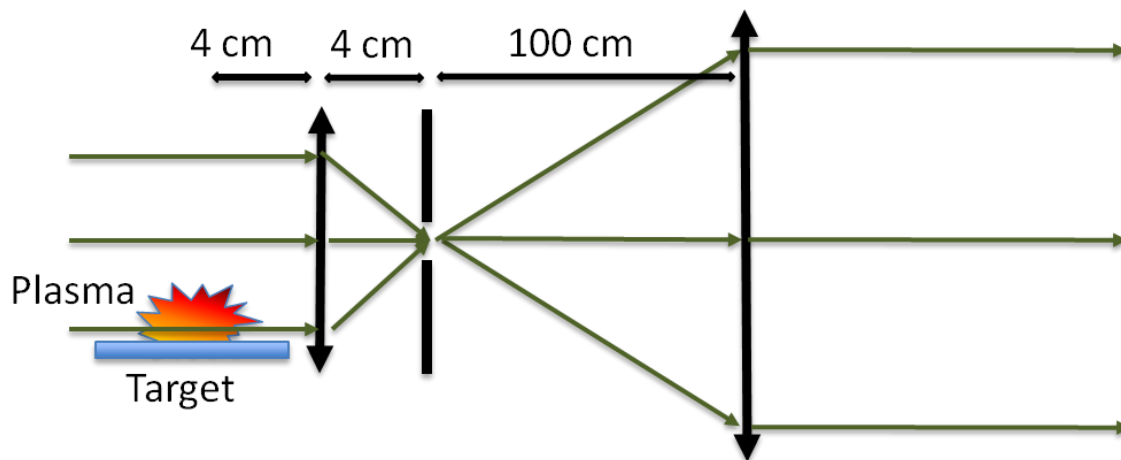


Figure 13: Schematic of the optical system utilized to manipulate the probe beam inside the target chamber. One section of the probe beam passed through the target pre-plasma and the entire beam was then magnified by a factor of twenty using a telescope made from achromatic lenses. Light emitted from the plasma was mostly filtered using an iris at the focal length of the first lens.

The front surface of the target was placed at the focal spot of a 4x objective with a 4 centimeter focal length, which was protected from being damaged by shrapnel using a flat glass blast shield. At the back focal point of this objective, an iris was used to filter out the majority of the light emitted by the plasma. A one meter focal length achromatic lens was used to recollimate the probe beam after the 4x objective, giving a total magnification of about 20. A drawing of this arrangement is shown in figure 13.

After the last achromat, the probe beam was sent out of the target chamber and into a Michelson interferometer with a flat mirror in one leg and a rooftop prism in the other, as shown in figure 14. A 50-50 beamsplitter evenly divided the amplitude of the probe beam between these two legs. The rooftop prism inverted the beam that it reflected, while the beam sent to the mirror was directly reflected. The beams were then

recombined, overlapping the potentially phase shifted portion of the beam profile that passed along the target surface with the portion that passed the target at a sufficient distance to avoid interaction with any plasma. These combined beams were passed through a 532 nanometer line filter with a 5 nanometer bandwidth to further filter emission from the plasma that was collected by the probe beamline optics. They were then incident on an 8-bit CCD camera triggered by the master TPW clock, which recorded an interference pattern.

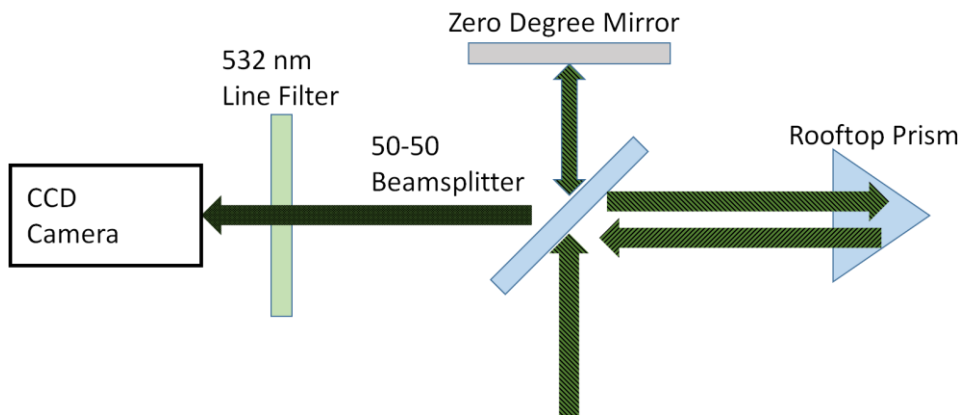


Figure 14: Schematic of the Michelson interferometer used to diagnose the pre-plasma density at the front target surface just before the arrival of the main peak of the laser pulse. A 50-50 beamsplitter directed half of the probe beam energy to a zero degree mirror and the other half to a rooftop prism. The reference half of the beam was then overlapped on a CCD camera with the portion of the beam that passed through the pre-plasma, producing interference fringes.

In order to determine the relative timing between the probe pulse and the main laser pulse, both beams were directed onto a fast photodiode and the output was sent to an oscilloscope. To accomplish this measurement, a flat piece of glass was placed at target chamber center. The main beam was observed in transmission through this

substrate, while the probe beam was reflected onto the photodiode. Using this method, it was determined with a resolution of 50 picoseconds that the probe beam interrogated the target pre-plasma at about 150 picoseconds before the main pulse.

In order to collect meaningful information about the target pre-plasma using the probe beam and interferometer, an OPA reference shot was taken before each laser system shot. For this reference shot, the beam dump in the TPW system was used to block the primary beam while the probe beam was allowed to propagate through the target chamber, along the target surface, and through the interferometer. This provided a reference interference pattern of straight fringes produced in the absence of any plasma. A change in this otherwise straight fringe pattern was then observed by the interferometer camera on the following system shot, indicating the presence of a plasma along the probe beam path. A reference interference pattern and the modified pattern recorded on the corresponding system shot are shown in figure 15.

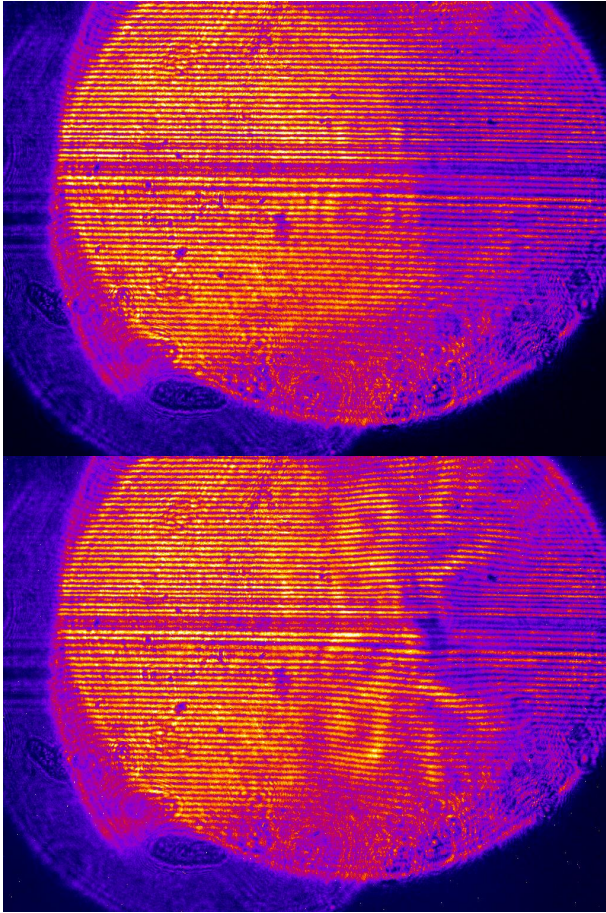


Figure 15: Reference and data images from the interferometer camera. The left image was taken using only the probe beam, with no laser light incident on the front of the target. The right image was taken on a system shot, showing the distortion of the straight fringes by the presence of pre-plasma. The phase extracted from the reference image was then subtracted from the phase extracted from the data image to yield the phase shift caused by the plasma.

As described previously, the shift in the interference patterns on a system shot relative to a reference shot provides information about the total integrated plasma density along the probe beam path. The retrieval of these phase shifts from the raw images was accomplished using a standard Fourier domain methodology [89]. The data recorded by the interferometer camera as the reference and data images, denoted by  $r(x,y)$  and

$d(x, y)$ , respectively, were two-dimensional arrays describing the intensity recorded at each position on the beam profile. The fringes recorded by the reference shot prior to each system shot were set to be horizontal, with a roughly sinusoidal variation in the vertical direction. Therefore, these spatial intensity patterns can theoretically be expressed in the form:

$$r(x, y) = a(x, y) + b(x, y) \cos[2\pi f_0 y]$$

$$d(x, y) = a(x, y) + b(x, y) \cos[2\pi f_0 y + \varphi(x, y)]$$

where  $x$  is the horizontal coordinate,  $y$  is the vertical coordinate,  $f_0$  is the spatial carrier frequency of the fringes, and  $\varphi(x, y)$  is the desired phase shift between the data shot and the reference [89]. In this expression,  $a(x, y)$  and  $b(x, y)$  represent undesired intensity variations caused by noise, damaged or dirty optics, and other effects that reduce the uniformity of the beam profile [89]. For convenience, these functions can also be expressed in complex form as:

$$r(x, y) = a(x, y) + \frac{b(x, y)}{2} \exp[2\pi i f_0 y] + \frac{b^*(x, y)}{2} \exp[-2\pi i f_0 y]$$

$$d(x, y) = a(x, y) + c(x, y) \exp[2\pi i f_0 y] + c^*(x, y) \exp[-2\pi i f_0 y]$$

where  $c(x, y) = \frac{b(x, y)}{2} \exp[i\varphi(x, y)]$  and the star indicates complex conjugation.

As a step toward recovering the phase function of interest, this two-dimensional intensity data was then Fourier transformed in the vertical direction. The result was frequency domain data at each horizontal position, expressed mathematically as:

$$R(x, f) = A(x, f) + \frac{1}{2} B(x, f - f_0) + \frac{1}{2} B^*(x, f + f_0)$$

$$D(x, f) = A(x, f) + \frac{1}{2}C(x, f - f_0) + \frac{1}{2}C^*(x, f + f_0)$$

where capital letters represent the Fourier transform of the corresponding function that is labeled with a lowercase letter. These spectral domain expressions display large peaks near DC corresponding to noise in the images and symmetric peaks near the carrier frequency of the fringes [89]. In order to filter out much of the noise in the images, the spectral data was multiplied by a window function centered on the positive fringe carrier frequency. This window function, denoted by  $W(f)$ , took the form of a super-Gaussian described by:

$$W(f) = \exp\left[\frac{f - f_0}{\sigma}\right]^N$$

where  $N > 2$  and  $\sigma$  were parameters chosen for each data set on a case-by-case basis. More specifically, these numbers were chosen to ensure that the filter function was approximately five to ten times as wide as the individual symmetric peaks in the spectral data but still fell to zero without overlapping the noise located around zero frequency [90].

After filtering in the spectral domain, the resulting image data included only the positive frequency components of the original data set:

$$R'(x, f) = R(x, f)W(f) = \frac{1}{2}B(x, f - f_0)$$

$$D'(x, f) = D(x, f)W(f) = \frac{1}{2}C(x, f - f_0)$$

where  $R'$  and  $D'$  are filtered data. This filtered data was then shifted to DC in order to remove the sinusoidal oscillations at the fringe carrier frequency:

$$R'(x, f) \rightarrow R'(x, f + f_0) = \frac{1}{2}B(x, f)$$

$$D'(x, f) \rightarrow D'(x, f + f_0) = \frac{1}{2}C(x, f)$$

where the arrow in these expressions indicates the transformation. Finally, this filtered and translated data was inverse Fourier transformed to recover the functions  $b(x, y)$  and  $c(x, y)$ . which had been isolated from the other terms and factors in the original intensity data by the manipulations in Fourier space [89].

The complex logarithm of the difference between the functions  $b(x, y)$  and  $c(x, y)$  can be expressed as:

$$\text{Log}[c(x, y) - b(x, y)] = \varphi(x, y)$$

which describes the phase shift in the interference fringes due to the laser-produced plasma. Unfortunately, the computational analysis procedure detailed above results in a two-dimensional phase map with values limited to the range between zero and two pi [89]. The creation of a continuous phase map from the discontinuous phase obtained from the Fourier transform is a process called phase unwrapping [90]. Identification of the best methods for efficient and accurate phase unwrapping in various contexts remains a major topic of investigation in modern computational science. Entire books have been filled with information on this topic, some with example code for implementation of various algorithms, and a thorough discussion of phase unwrapping is outside the scope of this thesis [91].

During this work, phase unwrapping was performed using a code written by Dr. Will Grigsby [90]. This program was capable of employing a number of algorithms to

produce a continuous phase map from a discontinuous one [90]. Examples include a minimum weighted discontinuity algorithm developed by Thomas Flynn, a residue and branch cut algorithm developed by Richard Goldstein, and a quality guided algorithm developed by Donald Bone to the phase unwrapping problem [92] [93] [94]. Application of one of these algorithms returned the two-dimensional phase map  $\varphi(x, y)$ , containing all experimental information about the plasma that interacted with the probe beam.

As described above, the total phase shift in the probe beam at different points in front of the target provided a measure of the total amount of plasma encountered by a given portion of the beam. By making the simplifying assumption that the plasma had a rectangular shape extending from the front surface of the target, the average plasma density was calculated from this phase shift. To accomplish this calculation, the linear extent along the target surface of the region of negative phase shift was determined. Denoting this dimension by  $d$ , the average index of refraction, denoted by  $n_{avg}$ , along each line of sight was then calculated from the total phase shift, denoted by  $\Delta$ , to be:

$$n_{avg} = 1 + \Delta * \frac{c}{\omega} * d$$

The average plasma density followed immediately from the equation describing the index of refraction of a plasma.

## **Chapter 5: Experimental Results**

This chapter presents results from the campaign of experiments covered by this thesis, as well as supplemental contrast measurements performed by the TPW scientific staff. These experimental measurements indicate that the nature of a laser-target interaction has a strong dependence on both the target thickness and the properties of the target pre-plasma. In turn, the formation of this pre-plasma depends on the details of the laser pulse contrast profile. Targets thinner than one micron were seen to produce very different results than thicker targets and the presence of plasma mirrors was seen to significantly impact results compared to the standard laser pulse. While these general effects have been observed in the past at other laser facilities, this work presents a characterization of these phenomena at the TPW system.

This chapter begins by describing the result of contrast measurements of the TPW laser pulse. These measurements indicate the presence of numerous pre-pulses from pencil beams and wrap around of post-pulses, but fail to convincingly measure the effect of plasma mirrors on these pulse features. Experimental results from shots on targets thicker than one micrometer are then presented, which indicate that these targets were capable of surviving the pre-pulse and pedestal features of the pulse. This data shows an enhancement in laser accelerated ion energies upon the introduction of plasma mirrors, suggesting that these filters modify the laser-target interaction. Results from experiments on the irradiation of ultrathin nanoscale targets are then presented, including particle data and measurements of the pre-plasma density profile in the absence of plasma mirrors. These measurements suggest that ultrathin targets were destroyed by the pre-pulse

features of the unfiltered laser pulse, preventing any ion acceleration but producing beams of energetic electrons. The implementation of plasma mirrors was seen to drastically change this interaction, resulting in the highest ion energies ever measured at TPW.

### **LASER CONTRAST**

The single-shot third order autocorrelator was used to measure the pedestal of the TPW laser pulse and determine the effect of plasma mirrors on this feature. To this end, a small portion of the expanding laser cone was picked off after the focus by a one inch mirror, spatially filtered, and sent to the diagnostic, which is described in detail in the Third-Order Autocorrelator section of the Diagnostics chapter. TPW shots were taken into the autocorrelator without plasma mirrors, with uncoated glass plasma mirrors, and with anti-reflection (AR) coated plasma mirrors. In order to optimize the ignition time of the plasma mirrors, their position along the laser propagation direction was scanned over a series of shots. As expected, both types of plasma mirrors diminished the intensity of the laser pulse's pedestal and decreased the rise time up to the main intensity peak. Experimental observations indicate that uncoated glass slides decreased the pulse pedestal by a factor of half an order of magnitude when placed at this optimum position, even at times as close as one picosecond to the main pulse. Further, the utilization of antireflection coated optical glass plasma mirrors introduced a factor of a full order of magnitude of contrast improvement compared to the unfiltered laser pulse. These results are shown in figure 16 below.

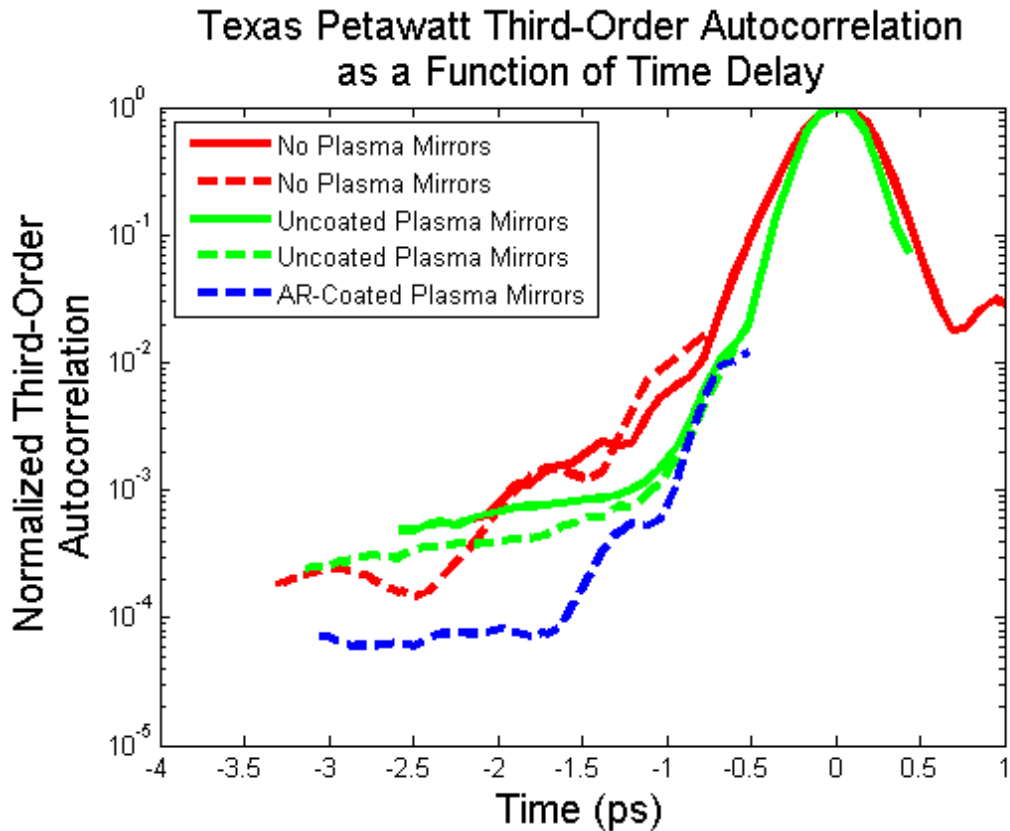


Figure 16: Processed third-order autocorrelator traces showing the intensity profile of the Texas Petawatt laser pulse. The red profile is the unfiltered laser pulse, the green profile is the pulse with uncoated plasma mirror filtering, and the blue profile is the pulse with anti-reflection (AR) coated plasma mirror filtering. The uncoated plasma mirrors were seen to reduce the intensity of the pulse's pedestal by about half an order of magnitude, with the AR coated slides providing a full order of magnitude of contrast enhancement.

Unfortunately, the contrast measurements collected during this experiment were not sufficient to diagnose the entire laser pulse profile or fully quantify the value of the plasma mirrors. Valid data was only collected out to a time of about 2.5 picoseconds before the main pulse. Measurements at earlier times were buried under a noise floor that was only  $10^{-2}$  to  $10^{-3}$  below the maximum signal level. All efforts to increase the signal

to noise ratio were unsuccessful, resulting in a very incomplete pictures of the TPW pulse profile.

There are a number of lessons from this effort that will improve the prospects of future attempts to field a similar diagnostic. These recommendations are primarily aimed at increasing the signal-to-noise ratio of the contrast measurements, since that was the limiting factor that prevented the collection of adequate data. To begin, the imaging lenses in the second harmonic leg of the autocorrelator need to be carefully aligned to ensure proper imaging of the grating onto the SFG crystal in the horizontal dimension. If the grating is not imaged to this crystal, the resulting signal will be smeared temporally and will not accurately represent the true pulse shape. In addition, cylindrical lenses can be inserted into each leg of the autocorrelator to focus light onto the SFG crystal in the vertical direction. This increases the intensity of the beams as they interact in the crystal, boosting the signal level considerably.

In addition to these signal boosting methods, there are also some techniques to reduce the noise level of the third-order autocorrelation signal. The most beneficial of these is the introduction of a nonzero vertical crossing angle for the beams in the SFG crystal. Direct conversion of fundamental light to third harmonic light was identified to be a major noise source, as evidenced by the observation of significant signal levels when the second harmonic leg of the instrument was blocked. If the beams are overlapped with a vertical crossing angle at the second crystal, the third harmonic light produced by this direct conversion is spatially separated from the SFG signal. A pinhole or slit can then be introduced after the crystal to filter the original beams and pass only the SFG light.

Another possible source of noise was the accumulation of B-Integral as the pulse passed through bulk media on the way to the autocorrelator. As described in the third-order autocorrelator diagnostic section above, the energy of each shot into the autocorrelator was recorded using the reflection from a wedged glass window. The window out of the target chamber, through the wedge directing light to the energy meter, and through absorptive glass filters.

Further measurements of the TPW temporal intensity profile were performed by the laser's technical staff, led by Dr. Erhard Gaul. This effort consisted of both energy contrast measurements made with a fast photodiode and intensity contrast measurements made with a single-shot third-order autocorrelator [95]. In order to collect the energy contrast data, Dr. Gaul attenuated the TPW pulse and focused the attenuated beam through a pinhole in air prior to irradiation of a fast InGaAs photodiode connected to a high bandwidth oscilloscope. This method produced measurements with a dynamic range of about  $10^3$  over a temporal window extending out to 120 nanoseconds before the main pulse [95].

In order to obtain the complete pulse energy profile with a greater dynamic range, Dr. Gaul diagnosed a number of shots at various attenuation levels. With a large optical density attenuating the beam, the entire pulse profile passed through the pinhole and was recorded by oscilloscope [95]. At lower attenuation levels, damage to the photodiode was prevented by dielectric breakdown of the air by the field of the main pulse at the focal point within the pinhole. This produced a plasma that absorbed the energy of the main pulse, allowing only the less intense pre-pulse and pedestal features to pass on to the

photodiode [95]. With this methodology, Dr. Gaul was able to produce a complete measurement over ten orders of magnitude of the energy contrast of the TPW laser over 120 nanoseconds.

The complete energy contrast profile measured by Dr. Gaul is displayed in figure 17 below. The green dotted line in this figure indicates the detection limit of the measurement as a function of time, and the black spikes denote observed pre-pulses. The wide gray feature around the main pulse shows the energy level of the fluorescence pedestal due to ASE and OPF, which was measured to be  $10^{-4}$  of the peak energy [95]. The data reveals a number of pre-pulses, at energy levels as high as a few  $10^{-6}$  of the main pulse. These features were identified as pencil beams generated when ghost reflections from lenses in the spatially multiplexed TPW amplifier chain are clipped by the 1.5 millimeter diameter pinholes in the system, as described in the High Intensity Laser Systems section of chapter 2 [95]. By calculating the expected arrival time and energy level of parasitic pencil beams from each optical element in the TPW system, Dr. Gaul was able to identify the source of many of these pre-pulses.

Parasitic pencil beams skip some of the gain experienced by the main pulse, decreasing their energy to the observed level [15]. In addition, the 1.5 millimeter diameter of these pencil beams is much greater than that of the main laser pulse, which is focused in each spatial filter to a much smaller spot that is ultimately imaged to the target. This effect serves to reduce the peak fluence a pencil beam at TPW by about  $10^3$  relative to a properly focused and imaged beam [95]. Taking this effect into account, Dr. Gaul calculated the intensity for each pencil beam, and the results are displayed in figure

17 as red peaks next to the measured energy level of each black peak. Similarly, the calculated intensity of the fluorescence pedestal is shown in red below the gray level of the measured energy pedestal. The most energetic pencil beams were measured at 52 nanoseconds and 56 nanoseconds before the main pulse, with calculated intensity contrast ratios of just over  $10^{-8}$  [95].

Dr. Gaul also made measurements of the intensity contrast of the TPW system using a single-shot third-order autocorrelator. By implementing the improvements described above to the autocorrelator, he was able to increase the dynamic range of this instrument to  $10^6$ , allowing him to collect meaningful information about the pulse profile [95]. Each shot recorded intensity levels over a 26 picosecond window with the grating aligned for first-order diffraction, or a 52 picosecond window with alignment for second-order diffraction. Over the course of more than 20 data shot, Dr. Gaul collected intensity data from 250 picoseconds before the main pulse to 150 picoseconds after its arrival [95].

Within the sensitivity of the instrument, this third-order autocorrelation data does not show any pre-pulses out to 250 picoseconds before the main pulse. However, the measurements did reveal a number of highly intense post-pulses within 150 picoseconds of the peak intensity [95]. These features are likely formed by multiple reflections in optical elements throughout the laser chain. Since they exist within the 2 nanosecond temporal window occupied by the stretched main pulse, it is likely that these post-pulses introduce modulate the main pulse and produce pre-pulses on by the mechanism of post-pulse wrap around described in the High Intensity Laser Systems section of chapter 2 [16]. Dr. Gaul calculated the theoretical intensity levels of the pre-pulses produced by the

post-pulses, and the results are shown in figure 17 in red within the temporal duration of the pedestal. It is likely that there are additional post-pulses in the TPW system at time delays greater than 2 nanoseconds, but these are inconsequential because they cannot produce pre-pulses [95].

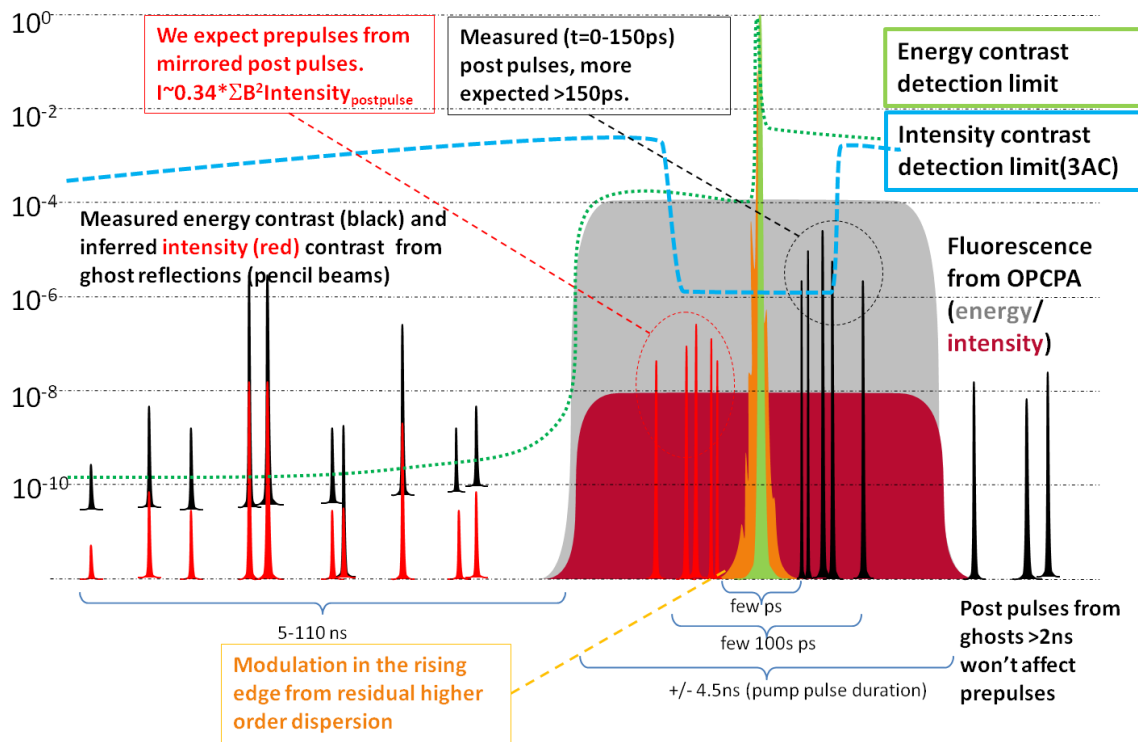


Figure 17: Measured temporal contrast of the Texas Petawatt laser pulse. A number of pencil beam pre-pulses were detected during energy contrast measurements at times from 5 to 110 nanoseconds before the main pulse. The energy of the pedestal, extending up to 4.5 nanoseconds before the main pulse was also measured. A number of post-pulses were measured with a third-order autocorrelation intensity measurement. Post-pulses within the temporal window of the pedestal likely wrap around to produce pre-pulses. The calculated intensity for these pulse features are shown in red. This data is presented courtesy of Dr. Erhard Gaul and the TPW scientific staff [95].

The large number of pre-pulses identified by these measurements were likely very destructive to the ultrathin targets irradiated during the experiments described in this thesis. Of particular concern are the most intense pencil beams around 50 nanoseconds before the main pulse and the pre-pulses within 2 nanoseconds that were caused by wrap around of post-pulses. The destructive nature of these features is evidenced by interferometry measurements performed by Dr. Gilliss Dyer and described by Dr. Gaul, which indicate the formation of a pre-plasma in front of wire targets at a time 50 nanoseconds before the main pulse [95]. This is consistent with Thomson parabola data presented in the Thin Targets section of this chapter, which shows no ion acceleration from ultrathin targets irradiated by the unfiltered TPW pulse. This suggests that the integrity of these fragile targets was compromised by the pre-pulses. Further interferometric measurements described in the Thin Targets section provide additional evidence to support this hypothesis, as they show a diffuse underdense plasma cloud formed from a formerly solid target at a time 150 picoseconds before the main pulse.

Unfortunately, the contrast data collected during this campaign does not convincingly demonstrate the effect of plasma mirrors on the TPW pulse. However, there is sufficient evidence to infer that the double plasma apparatus significantly improved the pulse contrast. This is evidenced by the observation of ion acceleration from targets as thin as 20 nanometers when plasma mirror filtering was implemented. These observations, described in the Thin Targets section below, indicate that the pulse features responsible for destroying thin targets before the main pulse were reduced to an inconsequential level by the plasma mirrors.

## **THICK TARGETS**

Traditionally, targets thicker than one micron have been most commonly employed in laser-matter interaction experiments. When irradiated, foils in this thickness range typically survive the pre-pulse and pedestal of the laser, albeit with the formation of some amount of pre-plasma at the front target surface. The main pulse of the laser therefore interacts with a plasma gradient that ramps up all the way to solid density. The survival of a relatively sharp interface at the rear target surface allows for the production of ion beams from these thick targets through the TNSA mechanism, as described in the Ion Acceleration section of the background chapter of this thesis [50] [49]. However, the details of the interaction and the energy of the resulting ions depends on the hot electron temperature and the scale length of any pre-formed plasma at the rear target surface [52]. In turn, these properties on the intensity profile before the peak of the laser pulse.

Experimental results from the TPW laser support this heuristic description, with ion diagnostics indicating the production of ions from targets thicker than one micrometer regardless of the presence or absence of plasma mirrors. This confirms that these targets were capable of supporting a sheath field at the time of arrival of the main pulse, and indicates that the steep density gradient at the rear target surface was not destroyed by the pre-pulse features described in the Laser Contrast section above. Ion measurements were made with both copper activation stacks and a Thomson parabola spectrometer. In addition, electron spectra recorded using a suite of electron spectrometers. All of the relevant details describing the design and operation of these diagnostics, as well as the analysis of the resulting data, are described in the Diagnostics chapter of this report.

Images of the activation signal from stacks of copper plates, as described in the Activation Stacks section of the Diagnostics chapter, showed strong activation in the first copper plate, as seen in figure 18. Measurements of the half-life of this activated copper revealed it to be the isotope  $^{63}\text{Zn}$ , formed in nuclear reactions induced by protons (for full details on the nuclear reactions induced in copper by various particles, see the Diagnostics chapter). There was no observable difference in this activation signal when plasma mirrors were implemented with thick targets. These results confirmed that energetic beams of ions were the primary products of interactions between the TPW pulse and targets thicker than one micron. According to stopping power data from the PSTAR database maintained by NIST, protons require an energy in the range of 30-35 MeV to penetrate 2 millimeters of copper [96]. The lack of significant activation from copper plates after the first therefore sets an upper limit on the energy of laser accelerated protons, both with and without plasma mirrors.

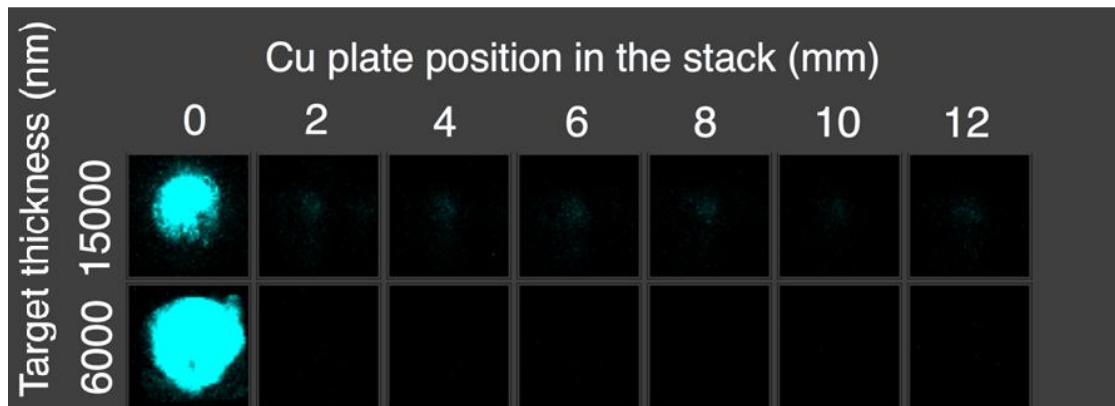


Figure 18: Activation signal of copper plates within the converter stack after the irradiation of thick targets. Each row presents an activation signal from a target of different thickness. The signal is due to the decay of  $^{63}\text{Zn}$ , created when ions interact with copper nuclei. The induced radioactivity is confined to the first layers of copper, indicating activation by protons with energies less than 30-35 MeV.

Ions were also observed by the Thomson parabola spectrometer upon the irradiation of thick targets, both with and without plasma mirror filtering. Typical ion spectra from these targets were semi-exponential, and the point at which the signal fell below the background level was taken to be the maximum observed ion energy, as described in the Diagnostics chapter. For thick targets, most shots only produced a single ion trace produced by laser accelerated protons. A typical proton spectrum and the corresponding background signal level is presented in figure 19 below. In the case of thick targets irradiated without plasma mirrors, Thomson parabola spectrometer data indicated an absolute maximum observed proton energy of 12.3 MeV, with cutoff energies in the single digits on most shots. This is consistent with the energy cutoff suggested by the activation signals induced in the copper stacks. The maximum proton

energies measured by the spectrometer are presented in figure 20 below, along with data from thick targets irradiated after plasma mirror filtering.

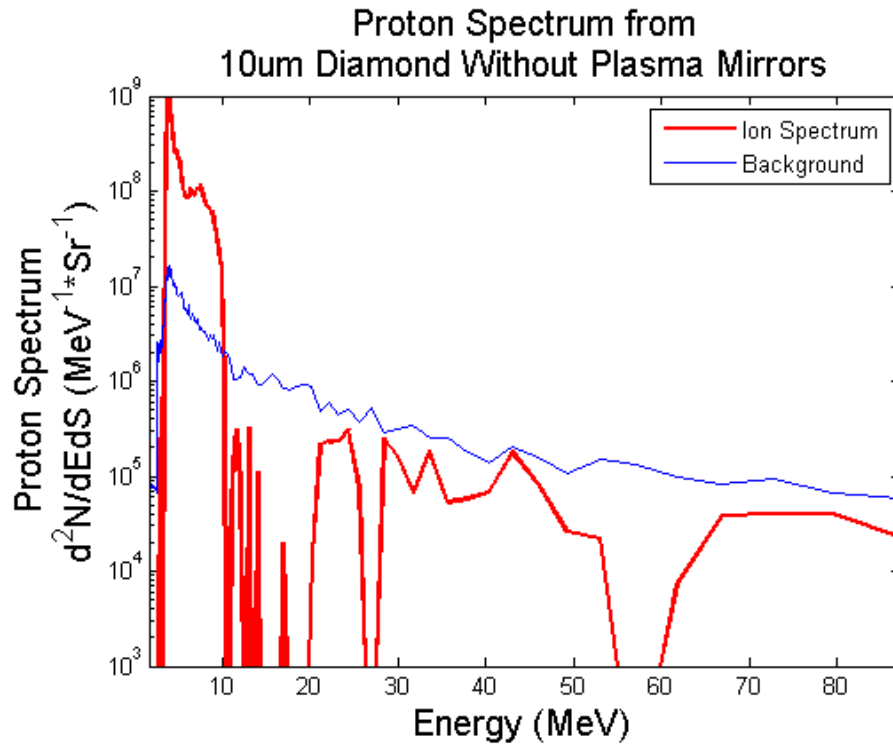


Figure 19: A typical proton ion spectrum measured by the Thomson parabola spectrometer is shown in red, while the background level of the measurement is shown in blue. This spectrum was produced by the irradiation of a 10  $\mu\text{m}$  diamond target without plasma mirrors, and the signal can be seen to cross below the background level at 10.2 MeV.

The spectra of protons produced from thick targets was also measured with plasma mirrors positioned before the target. The implementation of the double plasma mirror apparatus was seen to influence the maximum energy of these laser-accelerated protons, as measured by the Thomson parabola. As expected, introduction of these filters was seen to increase the maximum proton energy, resulting in particles as energetic as

21.4 MeV. This is a remarkable result considering that the plasma mirror pulse cleaner caused significant energy losses from the laser pulse.

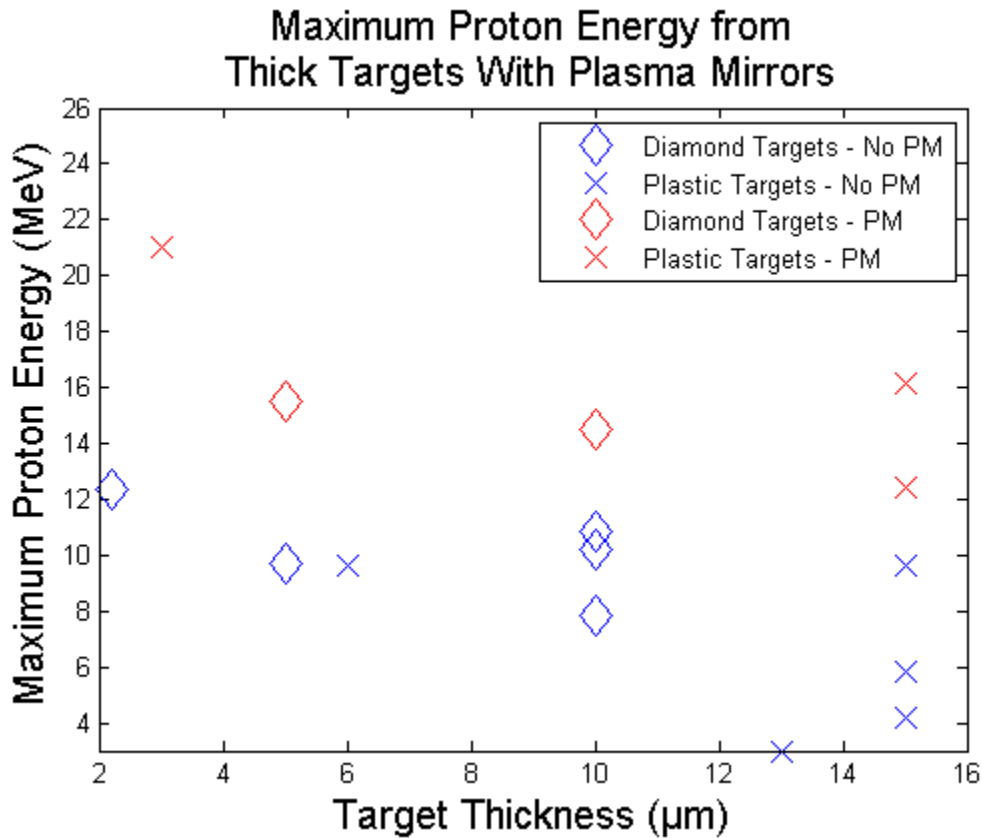


Figure 20: Maximum proton energies detected by the Thomson parabola spectrometer from targets thicker than 1 micron as a function of target thickness. Targets irradiated by the unfiltered pulse, shown in the blue, were only observed to produce proton energies below about 12 MeV. Targets irradiated with plasma mirrors, shown in red, produced protons with energies as high as 21.4 MeV.

The suite of electron spectrometers described in the Diagnostics chapter was utilized to record electron spectra produced from thick target irradiation, both with and without plasma mirrors. Typical electron spectra from these thick targets had an

exponential shape, as shown in figure 21 below. The measured spectra indicate the production of between  $10^{12}$  and a few  $10^{13}$  electrons per MeV per steradian. By fitting an exponential function to the high energy tail of the spectrum above 5 MeV, temperatures were determined for these observed electron populations. The temperatures characterizing these spectra were not seen to depend strongly on the target thickness, and were in the range of a few MeV to almost 20 MeV, with wide variations from shot to shot. The average temperature over all of the shots on thick targets without plasma mirrors was  $T_e = 10.2$  MeV. The implementation of plasma mirrors only weakly affected this average electron temperature, reducing it to  $T_e = 8.4$  MeV. This effect can be attributed to the reduction in the total pulse energy upon filtering with plasma mirrors.

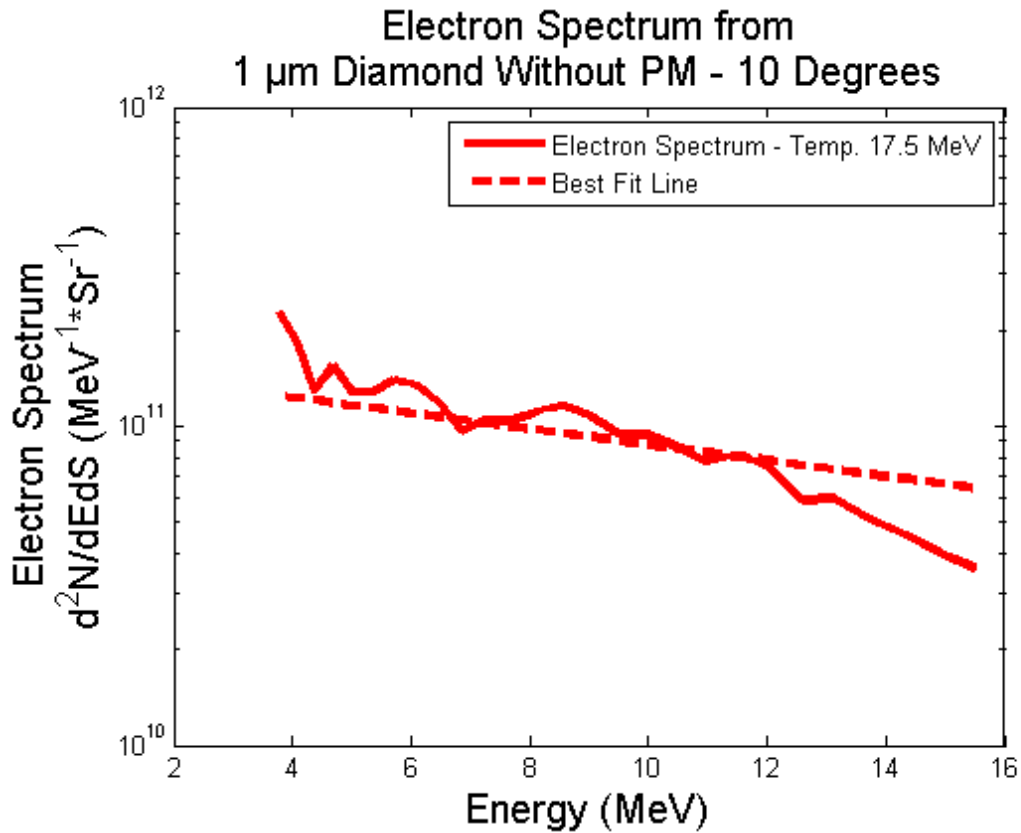


Figure 21: Typical electron spectrum measured at 10 degrees from a 1  $\mu\text{m}$  thick diamond target irradiated without plasma mirrors. The measured spectrum has a temperature of 17.5 MeV, as shown by the dashed fit line. The average electron temperature for targets 1  $\mu\text{m}$  and thicker was 10 MeV.

Typical electron spectrum measured at 10 degrees from a 400 nanometer diamond target irradiated with plasma mirrors. The measured spectrum has a temperature of 8.3 MeV, as shown by the dashed fit line. Average electron temperature for targets less than 1 micrometer thick was 7.7 MeV

The number of electrons measured by the small electron spectrometers was also determined for each shot by summing the counts from all four spectrometers. For thick targets, the results show that the small spectrometers collected between  $0.5 \times 10^7$  and  $1 \times 10^8$  total electrons on each shot. The exact number of electrons produced from these

targets was not seen to appreciably change when plasma mirrors were implemented, and any effect of this nature was less than the typical variations from shot to shot. The number of electrons detected by the spectrometers and the temperature of these electrons was roughly constant as a function of angle, as shown in figure 22. This is consistent with the theoretical description of TNSA described in the Ion Acceleration section of the Background chapter. In this model, a cloud of hot electrons is produced in the laser focus at the front target surface and expands as a cone from the target with some opening angle. In this case, the independence of the measured electron spectra with angle suggests that the half-angle of this expansion is at least 60 degrees.

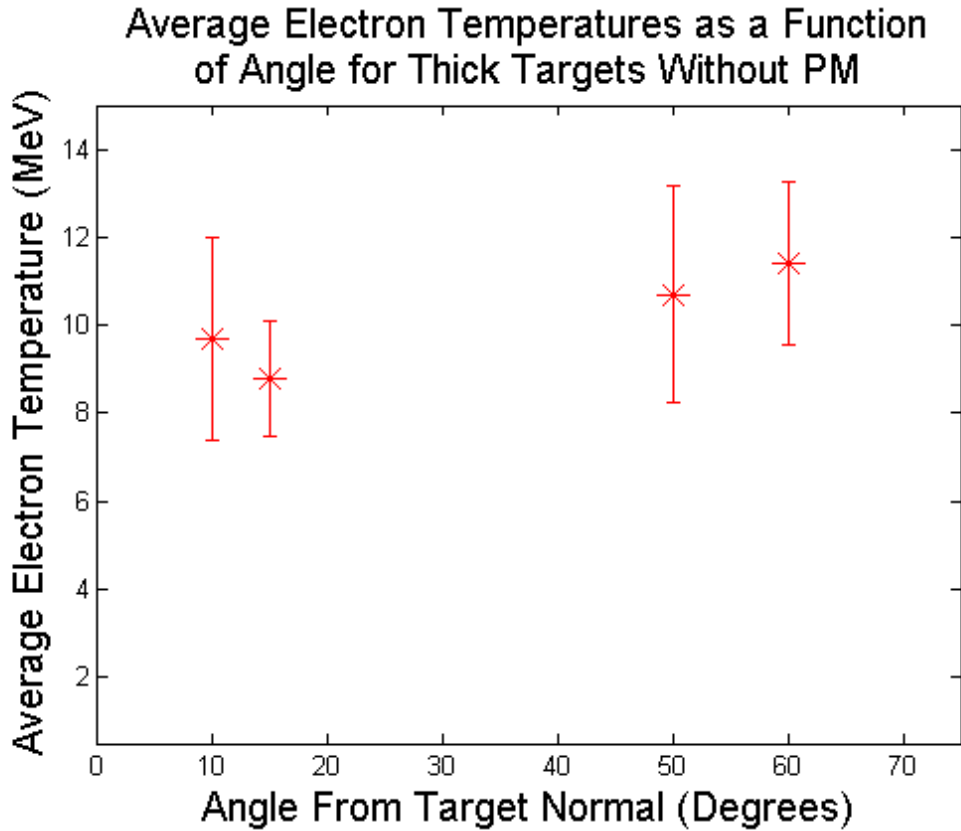


Figure 22: Average electron temperatures as a function of angle from thick targets irradiated without plasma mirrors, as recorded by the suite of small electron spectrometers. The uncertainty is given by the standard deviation of the electron temperatures. These temperatures are constant as a function of angle within the uncertainty. This is consistent with the uniform expansion of a hot cloud of electrons in a cone with an opening angle  $\theta_e > 60^\circ$ .

In order to gain further insight into these results, the one-dimensional TNSA model described in the Ion Acceleration section of the Background chapter can be applied to these experimental results. Recall that this model gives a theoretical expression for the maximum energy of protons produced by TNSA, given by:

$$E_p = 2T_e \left\{ \ln \left[ \frac{t_i \omega_{pp}}{\sqrt{2e_E}} + \sqrt{1 + \left( \frac{t_i \omega_{pp}}{\sqrt{2e_E}} \right)^2} \right] \right\}^2$$

where  $E_p$  is the proton cutoff energy,  $e_E = 2.71828 \dots$  is the Euler number, and  $t_i$  is the interaction time [7]. The proton plasma frequency at the rear target surface also enters into this equation, and is given by:

$$\omega_{pp} = \sqrt{\frac{n_{e0} e^2}{\epsilon_0 m_p}}$$

where  $n_{e0}$  is the initial electron density at the rear target surface,  $e$  is the electron charge,  $\epsilon_0$  is the permittivity of free space, and  $m_p$  is the proton mass.

Taking representative experimental values of  $E_p = 10$  MeV and  $T_e = 10$  MeV for the case of thick targets irradiated without plasma mirrors and approximating the interaction time by the pulse duration,  $t_i = 150$  femtoseconds, the first equation above gives a proton plasma frequency of  $\omega_{pp} = 1.19 \times 10^{13}$  cycles per second. In turn, this suggests an electron density at the rear target surface of  $n_{e0} = 8.21 \times 10^{19}$  particles per cubic centimeter. This result can then be substituted into the approximate theoretical expression describing the electron density at the rear target surface:

$$n_{e0} = \frac{N_e}{c\tau\pi[r + d \tan(\theta_e)]^2}$$

where  $\theta_e$  is the half-angle through which the electron beam diverges,  $\tau$  is the pulse duration,  $r$  is the focal spot radius, and  $d$  is the target thickness [7]. This equation will then allow for a determination of the half-angle of the electron expansion cone.

The final parameter needed to determine the electron expansion half-angle is the total number of electrons. This quantity can be approximated from the experimental electron spectral data. As reported above, four spectrometers were utilized, with each occupying a solid angle of  $\Delta\Omega = 2$  microsteradians as seen from the laser focal spot. As described above, the theoretical TNSA model assumes that electrons are uniformly distributed over a cone emerging from the focal spot with a half-angle  $\theta_e$ , which subtends a solid angle  $\Omega$  given by:

$$\Omega = 2\pi[1 - \cos(\theta_e)]$$

as is well known from basic geometry. On each shot, the four spectrometers observed an average total of  $\Delta N_e = 5 \times 10^7$  electrons. So, for electrons uniformly distributed throughout  $\Omega$ , we have:

$$\frac{\Delta N_e}{N_e} = \frac{4\Delta\Omega}{\Omega}$$

$$N_e = \frac{5 \times 10^7}{(8 \times 10^{-6})} 2\pi[1 - \cos(\theta_e)]$$

which uses experimental data to express the total number of electrons in terms of their divergence half-angle.

Now, the divergence half-angle of the hot electrons can be calculated. Substituting experimental values  $d = 2$  micrometers,  $\tau = 150$  femtoseconds, and  $r = 5$  micrometers into the theoretical equation for the divergence half-angle, we have:

$$8.21 \times 10^{25} m^{-3} = (2.78 \times 10^{17}) \frac{[1 - \cos(\theta_e)]}{[(5 \times 10^{-6}) + (2 \times 10^{-6}) \tan(\theta_e)]^2} m^{-3}$$

which must be solved for  $\theta_e$ . This calculation yields an expansion half-angle of  $\theta_e = 87.8$  degrees for electrons produced from thick targets without plasma mirrors, which is consistent with the flat spectra measured out to 60 degrees. With this divergence angle, the total number of hot electrons is  $N_e = 3.78 \times 10^{13}$ . Given an average electron energy of  $T_e = 10$  MeV, this number allows for a determination of the total fraction of laser energy in the electron population, denoted by  $\eta$  and given by:

$$\eta = \frac{E_L}{N_e T_e}$$

where  $E_L$  is the laser energy. Given an average pulse energy of  $E_L = 100$  joules, this gives a coupling efficiency of laser energy into electron energy of at least  $\eta = 60.6\%$ , which is on the low end of reported absorption values from the literature for petawatt systems [97]. In actuality, this coupling efficiency must have been higher, since the ions absorbed their energy from the hot electrons.

A similar calculation can be carried out for the greater proton energies observed from thick targets irradiated without plasma mirrors. For this case, we simply modify the observed maximum proton energy to be  $E_p = 20$  MeV and the average electron temperature to be  $T_e = 8$  MeV. Carrying out the same calculation for this case, the theory gives a proton plasma frequency of  $\omega_{pp} = 2.12 \times 10^{13}$  cycles per second, a rear surface electron density of  $n_{e0} = 2.59 \times 10^{20}$  particles per cubic centimeter, and an electron cone half-angle of  $\theta_e = 85.7$  degrees. According to this simple model, the enhanced proton energies observed upon the introduction of plasma mirrors were due to this slight decrease in the electron divergence angle, resulting in an increased hot electron density at

the rear target surface. In this case we have  $N_e = 3.63 \times 10^{13}$ , which is negligibly different than the case of targets irradiated without plasma mirrors. However, targets irradiated after plasma mirror filtering demonstrated significantly enhanced coupling of the laser energy into electron energy. Using  $E_L = 69$  joules for the laser energy, since the double plasma mirror apparatus was measured to pass 0.69% of the incident energy, gives a coupling efficiency of  $\eta = 71\%$ . This value is closer to the expected level of absorption for a petawatt laser [97].

All told, the maximum ion energies observed during these experiments were relatively low when compared to reported energies from experiments at other petawatt class lasers [48] [53]. This is particularly true in the case of targets irradiated without plasma mirrors. However, the measured electron temperatures were roughly in line with the expected values due to ponderomotive heating, which is 7.3 MeV for a laser wavelength of 1.058 micrometers and an intensity of  $5 \times 10^{20}$  watts per square centimeter, which was characteristic for this work. Similarly, the coupling of laser energy into electrons was in reasonable agreement with literature values. These results suggest that the conversion of laser energy into electron energy took place with the expected efficiency, but the acceleration of ions by these electrons was hindered by the experimental conditions.

The significant increase of the maximum ion energy and electron coupling efficiency with the implementation of plasma mirrors suggests that the pre-plasma conditions at the target were strongly influenced by these filters. It is likely that the unfiltered TPW pulse caused the formation of significant plasma before the arrival of the

main pulse. The relatively long scale length presented by this plasma likely diminished the ability of the laser to produce hot electrons and increased their divergence angle. In turn, these effects reduced the electron density at the rear surface and decreased the magnitude of the sheath field, reducing the observed ion energies. By contrast, plasma mirrors seem to have inhibited the formation of this pre-plasma. This increased the coupling of laser energy into electrons, and ultimately into ions.

This heuristic picture is consistent with the results of the contrast measurements described in the previous section of this chapter, which show pre-pulses of substantial intensity at approximately 50 nanoseconds before the main pulse and within the 2 nanoseconds of the main pulse. This is also consistent with results from experiments with nanoscale targets, presented in the next section of this chapter. These targets were not able to produce ion beams unless plasma mirrors were used to filter the laser pulse. In fact, interferometric measurements detailed in that section suggest that 400 nanometer thick targets were completely destroyed before the arrival of the main pulse, leaving only an underdense plume of plasma.

### **THIN TARGETS**

Thin targets, with thicknesses below one micron, behaved very differently from thick targets when irradiated by the TPW pulse. This type of fragile target often cannot survive the intense pre-pulse and pedestal features that arrive before the main pulse of a typical ultrahigh intensity laser pulse. This leads to a physical situation in which the main laser pulse interacts with a significant amount of long scale length pre-formed plasma.

However, the irradiation of nanoscale targets by lasers with sufficient contrast has been observed to lead to an enhancement in the maximum ion energies produced by the TNSA mechanism. In addition, the BOA ion acceleration mechanism, which is based on driving a target to a state of relativistic transparency, has only been observed with nanoscale targets.

Experimental results from the TPW laser facility confirm this general description for this particular system. Nanoscale targets were irradiated by both the unfiltered TPW pulse and a filtered pulse that passed through a double plasma mirror apparatus, as described in the Experimental Set-Up Chapter. The spectra of ions and electrons produced during these interactions were recorded with activation stacks, a Thomson parabola ion spectrometer, and a suite of electron spectrometers. In addition, a probe beam was passed through the pre-plasma in front of ultrathin targets irradiated without plasma mirrors. This beam was then sent to an interferometer, producing measurements of the pre-plasma density in this regime. Details about the design and operation of these diagnostics and the analysis of experimental data are presented in the Diagnostics chapter of this thesis.

As described above, interferometric phase shift measurements were collected with the TPW probe beam during four shots on 400 nanometer thick plastic foils using the method described in the Probe Beam and Interferometer section of the Diagnostics chapter above. For each of these shots, the probe interrogated the plasma in front of the target at a time 150 picoseconds before the arrival of the main pulse. All of these measurements indicate the presence of a plasma well below critical density. While the

critical density for light at 1064 nanometers is  $9.9 \times 10^{20}$  electrons per cubic centimeter, the plasma profile measured by the probe beam only reached a few  $10^{18}$  electrons per cubic centimeter at the target surface, as shown in figure 23 below. This indicates that the intensity of pre-pulse features was sufficient to ionize the target well before the arrival of the main peak of the laser pulse, leaving time for the remaining plasma cloud to expand. The physical situation for thin targets irradiated by the unfiltered TPW laser was therefore one in which the laser interacted with an underdense plasma plume at peak intensity.

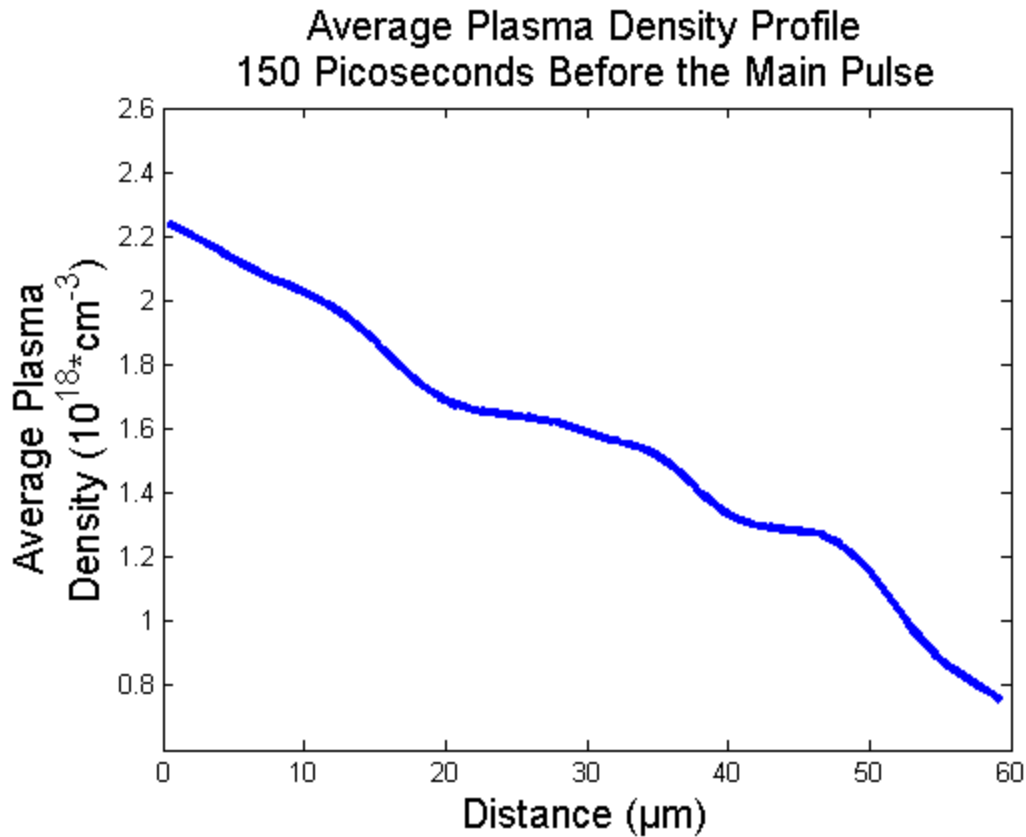


Figure 23: Pre-plasma density averaged over lines of sight as a function of perpendicular distance from the target surface. 400 nm thick targets were irradiated with the unfiltered TPW pulse to produce this plasma, which was measured 150 ps before the main pulse. The results indicate the presence of a plasma between  $10^{-2}$  and  $10^{-3}$  of critical density at the time of arrival of the main pulse.

Theoretically, the total number of electrons encountered by the probe beam can be determined by integrating the average plasma density over the extent of the plasma. This important number gives some indication of the amount of target material still present at the arrival of the main laser pulse. To obtain a rough estimate of this quantity, the plasma cloud was again to have a rectangular shape. The average plasma density along each line

of sight was then multiplied by the linear dimension of the plasma to obtain the total number of electrons encountered by each ray.

These calculations indicate that about  $10^{12}$  electrons interacted with the probe beam as it passed through the target plasma at a time 150 picoseconds before peak laser intensity. This number can be contrasted with the amount of matter contained in a 400 nanometer plastic target, which is 300 times the critical density for 1058 nanometer light at ambient conditions. This material contains  $10^{13}$  electrons within a 10 micrometer diameter section, which is approximately the size of the laser focal spot. The relatively small number of electrons present to affect the phase of the probe beam compared to the number in the target suggests that much of the target material had already been lost by the arrival of the main laser pulse.

Further data was collected by simply collecting the second harmonic light emitted by the pre-plasma at this same instant, 150 picoseconds before the arrival of the peak of the laser pulse. This was done by simply blocking the TPW probe beam and one leg of the interferometer. In this way, the plasma at the object plane in front of the target was collected by the probe line optics and imaged onto the camera, as described in the Diagnostics chapter. As shown in figure 24, these images show a bright plasma with linear dimensions of about 100 micrometers, in agreement with the phase shift measurements. The large extent of this plasma compared to the relatively thin target foil also suggests that the plasma had significant time to expand before the arrival of the main pulse.

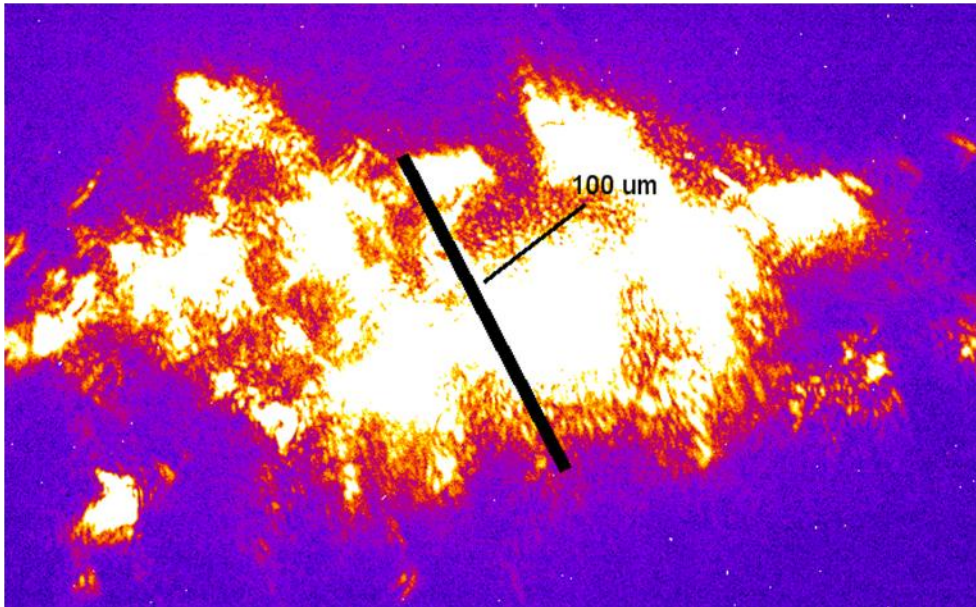


Figure 24: False color image of second harmonic light emitted from the expanding pre-plasma at the front target surface. This measurement was made by imaging the focal point of the laser to the interferometer camera with the probe beam blocked. The pre-plasma was measured to extend about 100 microns in front of the target.

The physical picture suggested by these measurements is one in which pre-pulse and pedestal features described in the Laser Contrast section of his chapter destroyed the thin targets before the arrival of the peak laser intensity. This lead to the interaction of the highest intensity light with a cloud of pre-formed plasma at a density between  $10^{-3}$  and  $10^{-2}$  of critical density. Such a system cannot support the strong sheath fields necessary for efficient ion acceleration, a fact that was confirmed by the observed absence of any ion signal when thin targets were irradiated by the unfiltered TPW pulse. However, this kind of slightly underdense plasma has been seen to be ideal for the acceleration of relativistic electrons. Previous experiments have demonstrated the production of

extremely collimated jets of electrons with tens of MeV through the irradiation of expanding plasmas at  $10^{-2}$  of critical density, as described in the Electron Acceleration and Heating section of the Background chapter [43]. Data collected using copper activation stacks suggests that similar jets were created during this experiment.

As described in the Activation Stacks section of the Diagnostics chapter, the activation signal due to induced radioactivity in stacks of copper provided much information about the particles produced by the irradiation of a target. This diagnostic produced some of the most convincing evidence that the dynamics of the laser-matter interaction differed significantly between thin and thick targets. For thin targets, It is significant that there was no observed signal from the decay of  $^{63}\text{Zn}$ , which is formed in ion induced nuclear reactions. As shown in figure 25, the primary activation signal recorded in the thin target regime was from the isotope  $^{62}\text{Cu}$ , produced by gamma and neutron induced reactions (for full details on the nuclear reactions induced in copper by various particles, see the Diagnostics chapter).

Since large numbers of energetic neutrons were not expected to be produced by the primary laser-target interaction in this experiment, the origin of this activation signal was identified as energetic photons. This implied a physical picture in which electron jets were produced from the laser irradiation of thin targets. These particles were stopped in the first layers of the copper, producing a directed beam of high energy bremsstrahlung x-rays that penetrated deeper into the stack, as illustrated schematically in figure 26 below. These photons then produced neutrons through interactions with copper nuclei, specifically the  $^{63}\text{Cu}(\gamma,n)^{62}\text{Cu}$  reaction, leaving behind radioactive  $^{62}\text{Cu}$ . The activation

signal produced by this mechanism was present even in the deepest layers of the copper, a drastic change from the signal observed upon the irradiation of thicker targets.

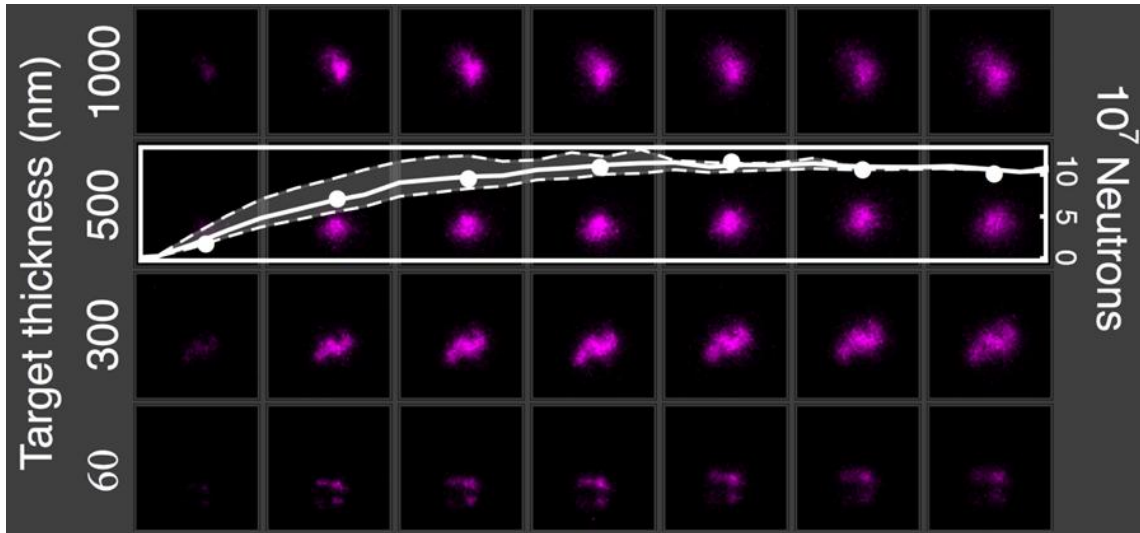


Figure 25: Activation signal of copper plates within the converter stack, recorded on an image plate. Each row presents an activation signal from a target of different thickness. The signal is due to the decay of  $^{62}\text{Cu}$ , created when bremsstrahlung photons interact with copper nuclei. Unlike the radioactivity induced by irradiating thick targets, this activation signal penetrates to the deepest layers of the copper stack. The spatial profile of the induced radioactivity acquired a notable lobed shaped when the thinnest targets were implemented.

The attenuation depth of the activation signal in the copper was measured after irradiation of a thin target, yielding a value of 22 millimeters. This is consistent with the stopping distance of MeV level photons in copper, supporting the hypothesis that these particles were produced in the first layers of the stack. The half-life of the radioisotopes responsible for the activation signal was also measured using a Geiger counter, confirming that the activation signal was due to the presence of  $^{62}\text{Cu}$ . In order to confirm

the nature of the particle jets incident on the copper, a thin target was irradiated with a 0.5 tesla magnet between the primary laser target and the copper converter. The activation signal from the copper stack dropped significantly upon the introduction of this magnet, confirming that charged particles were initially incident on the converter.

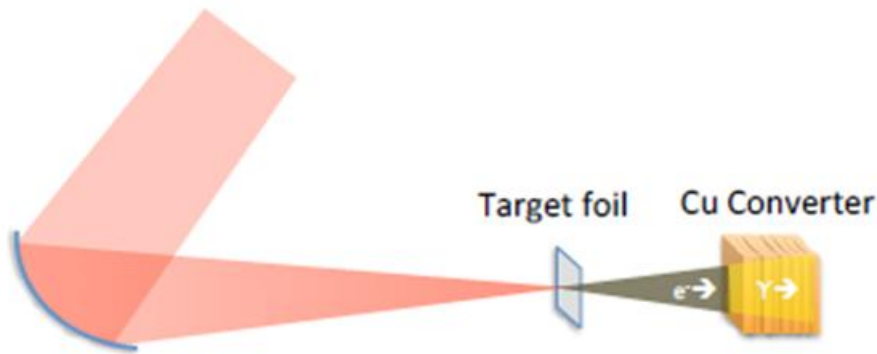


Figure 26: Schematic of the target chamber set-up utilized to shoot thin targets with a copper activation stack at the Texas Petawatt laser. Ultrathin targets were irradiated by the unfiltered TPW laser pulse, producing highly collimated electron beams that were incident on a copper converter. These electrons produced bremsstrahlung photons in the first layers of the converter, and these photons interacted with copper nuclei to produce radioactive  $^{62}\text{Cu}$ .

The spatial profile of the copper activation signal for thin targets is also quite striking, as the thinnest targets with thicknesses below 300 nanometers produced a lobed structure that was not observed when targets with thicknesses from 500 to 1000 nanometers were irradiated. This signal can be attributed to the filamentation of the laser beam and electron bunches in the early stages of interaction with a cloud of slightly underdense plasma. For targets of sufficient thickness, the megagauss scale magnetic fields produced by the interaction collapse these filaments down to a single beam before

the electrons exit the plasma. For the thinnest targets, electrons emerge from the plasma before the collapse of the filaments can take place. This direct laser acceleration scenario has been demonstrated in three-dimensional particle-in-cell simulations, as described in the Electron Acceleration and Heating section of the Background chapter [40]. This interpretation of the observed activation signal is also consistent with the interferometric plasma density measurements presented above, which suggest the presence of a plasma cloud with the proper density for direct laser acceleration at the time of arrival of the main laser pulse.

In order to modify the interaction between the TPW pulse and thin nanoscale targets, plasma mirrors were implemented as filters to improve the laser's contrast. This method had the desired effect, allowing for ion acceleration from targets as thin as 20 nanometers, the smallest thickness available for experimentation. The spectra of these particles was measured by the Thomson parabola spectrometer, as in the thick target experiments described in the previous section of this thesis. The observed signal was greatest for protons, with most shots recording a complete absence of any other ion species. As in the thick target experiments, typical proton spectra recorded during this work were semi-exponential, though with significantly more particle counts than the spectra from thick targets. This is remarkable considering the fact that plasma mirror filtering significantly reduced the incident laser energy. A typical ion spectra from this phase of the experiments is presented in figure 27.

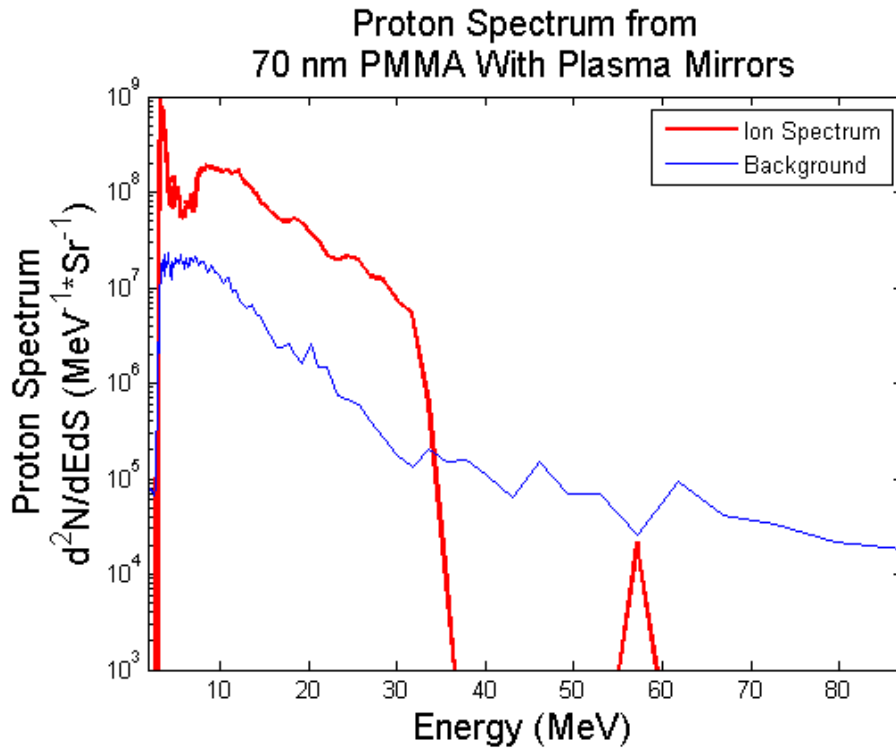


Figure 27: A typical hydrogen ion spectrum as measured by the Thomson parabola spectrometer after the irradiation of a thin target is shown in red. The background level of the measurement is shown in blue. This spectrum was produced by the irradiation of a 70 nm PMMA target with plasma mirrors, and the signal can be seen to cross below the background level at 34 MeV.

Remarkably, the highest ion energies of the whole experimental campaign were observed when irradiating ultrathin targets in this configuration. In this manner, protons were accelerated to energies greater than 35 MeV, and beams with cutoffs in the tens of MeV were routinely produced, as shown in figure 28. These results make it clear that the laser-target interaction dynamics at the TPW laser are most ideal for ion acceleration when thin targets are irradiated with high contrast. Maximum proton energy measurements suggest that the optimum target thickness for this system is a few hundred

nanometers. However, there was not a clear trend in the observed maximum proton energies as the target thickness was varied, likely due to substantial shot to shot variations in the laser pulse parameters.

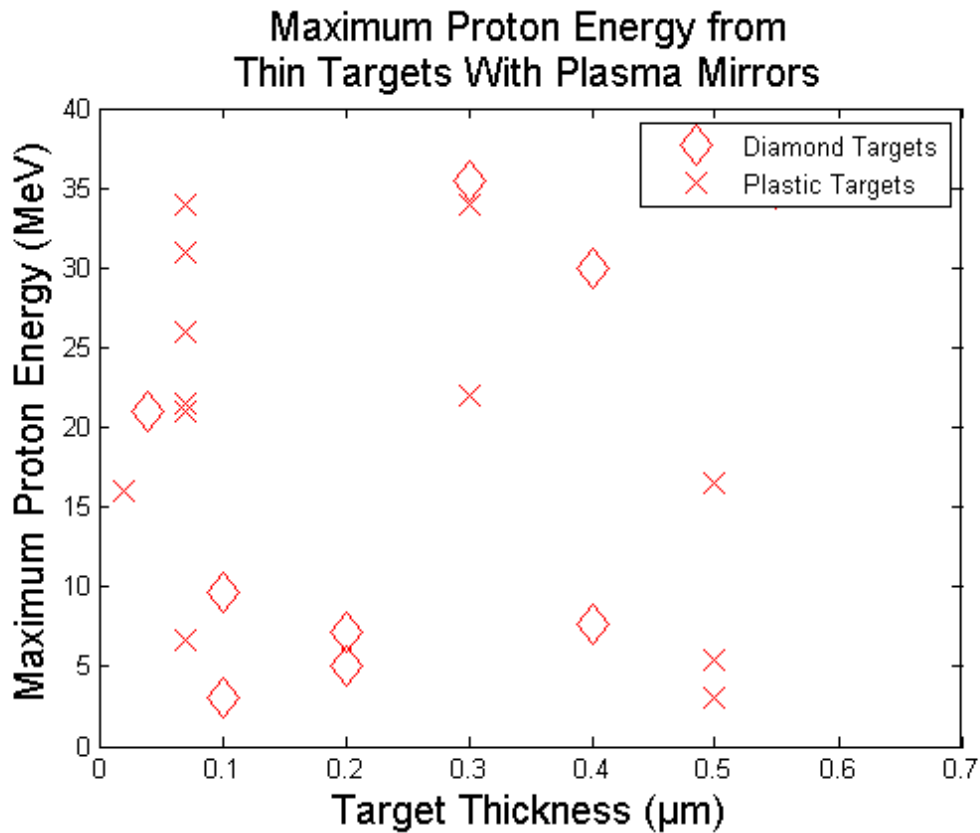


Figure 28: Maximum proton energies detected by the Thomson parabola spectrometer after the irradiation of diamond and plastic targets thinner than one micron with plasma mirrors. The maximum proton energy was greater than 35 MeV, significantly higher than the maximum energy observed from thicker targets.

Electron spectra from thin targets irradiated with plasma mirrors were seen to have the same rough shape as those from thicker targets. Again, these spectra were exponential with temperatures between a few MeV and about 15 MeV, with no clear

dependence of this parameter on target thickness. Typical electron spectra produced by thin targets irradiated with plasma mirrors are shown below in figure 29. The average electron temperature for shots during this phase was  $T_e = 7.7$  MeV, slightly lower than the values described in the previous section for thicker targets. The average total number of electrons recorded by the spectrometers was  $3 \times 10^7$ . As in the thick target case, the properties of the measured electron spectra were flat as a function of angle up to 60 degrees. The angular distribution of the average electron temperatures recorded during this work is shown in figure 30.

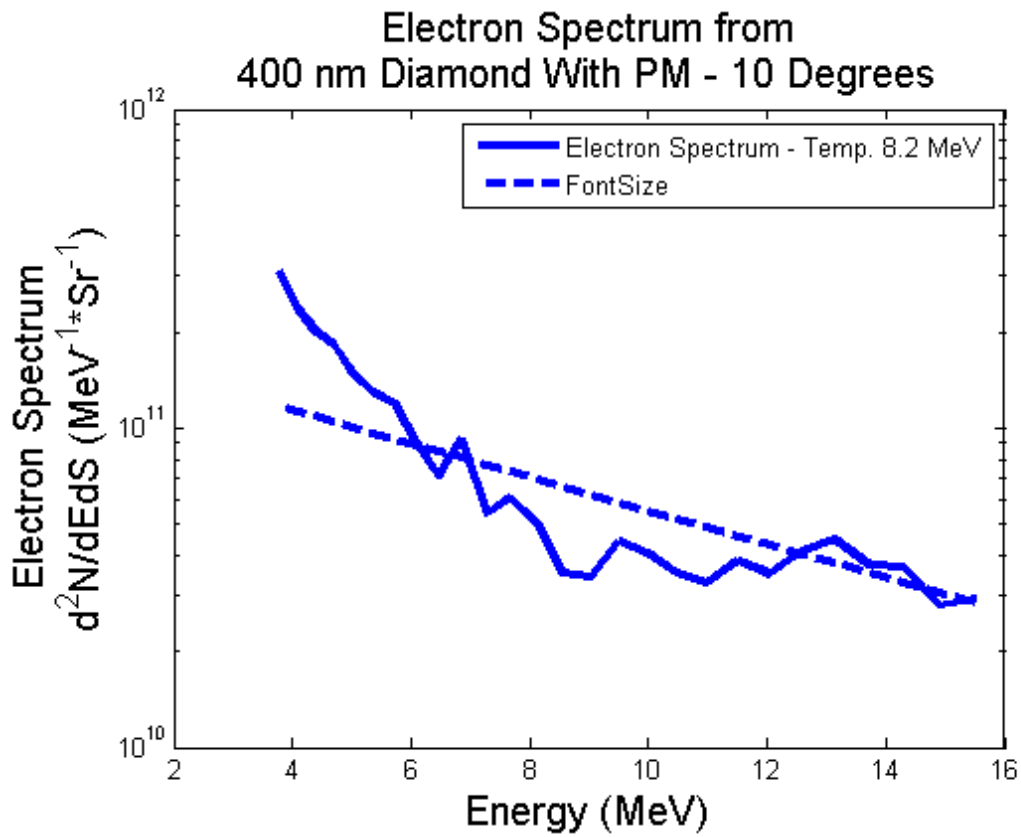


Figure 29: Typical electron spectrum measured at 10 degrees from a 400 nm diamond target irradiated with plasma mirrors. The measured spectrum has a temperature of 8.3 MeV, as shown by the dashed fit line. Average electron temperature for targets less than 1  $\mu\text{m}$  thick was 7.7 MeV

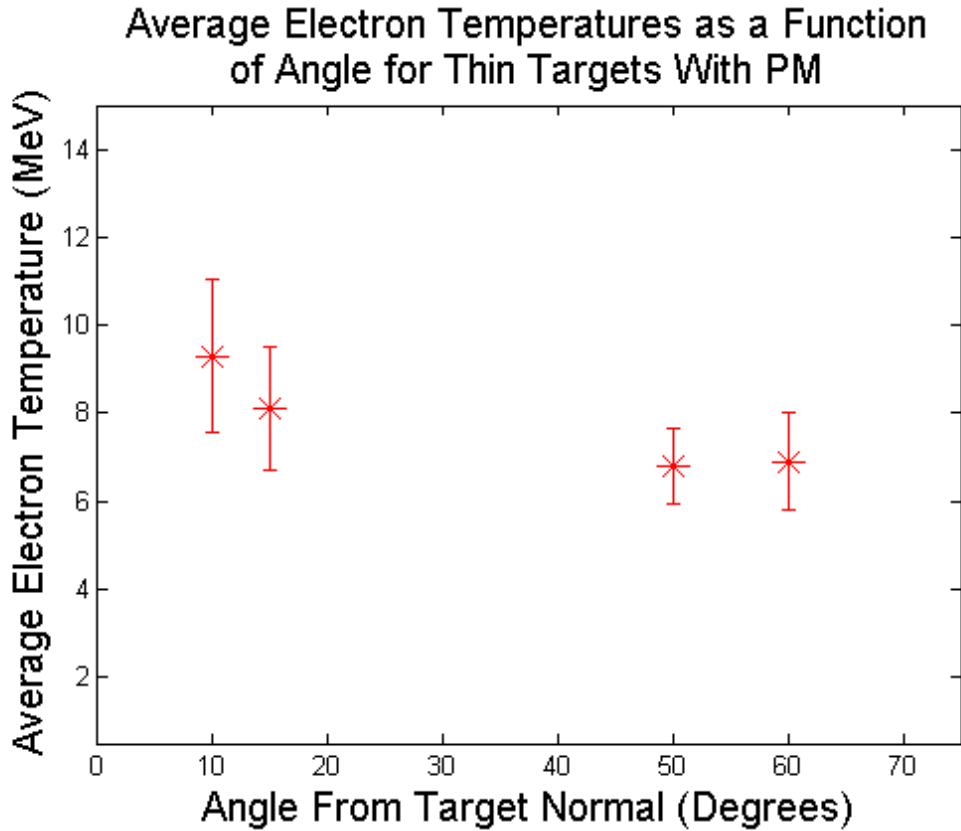


Figure 30: Average electron temperatures as a function of angle from nanoscale targets, irradiated with plasma mirrors. The measured electron temperatures were flat with increasing angle from target normal up to 60°.

The same theoretical analysis that was applied to the particle data from thick targets was carried out for the case of thin targets irradiated with plasma mirrors. The details of this process can be found in the Thick Targets section of this chapter. The TNSA model was applied with maximum proton energy of  $E_p = 35$  MeV, and electron temperature of  $T_e = 7.7$  MeV, an observed electron number of  $\Delta N_e = 3 \times 10^7$ , and with the interaction time approximated by the pulse duration,  $t_i = 150$  femtoseconds. The other parameters chosen were a target thickness of  $d = 300$  nanometers, a laser pulse duration of  $\tau = 150$  femtoseconds, and a focal spot radius of  $r = 5$  micrometers. With

these inputs, the theoretical model gives a proton plasma frequency of  $\omega_{pp} = 3.34 \times 10^{13}$  cycles per second, a rear surface electron density of  $n_{e0} = 6.43 \times 10^{20}$  particles per cubic centimeter, and an electron cone half-angle of  $\theta_e = 88.4$  degrees.

With this value for the electron divergence half-angle, the total number of hot electrons can be found to be  $N_e = 2.29 \times 10^{13}$ . This leads to a theoretically determined coupling efficiency from laser energy to electron energy of only  $\eta = 40.9\%$ , quite low for a petawatt laser [97]. This relatively weak coupling is surprising, given the large ion energies observed during this stage of the experimental campaign. This result suggests that the primary mechanism leading to enhanced ion energies from ultrathin targets during this work was the direct geometrical effect of a reduced target thickness. The increased charge density at the rear target surface with thinner targets was capable of increasing the observed ion energies despite the decreased electron heating efficiency.

These measurements suggest a consistent picture of the interaction of the TPW pulse with ultrathin targets. In the case of target irradiation without plasma mirrors, interferometric data suggests that the target is ionized by pre-pulses well before the arrival of the main laser pulse. This gives the resulting plasma time to expand, resulting in an underdense plasma at the time of arrival of the main pulse. This picture is consistent with the lack of any observed ion production from these targets and the observation of activation signals produced by energetic beams of collimated electrons. When these same ultrathin targets are irradiated with plasma mirrors in place to enhance the laser pulse contrast, the physical picture reverts to one of TNSA. In this case, the calculated transfer of laser energy to hot electrons seems to be less efficient than in the thick target case.

Nevertheless, these thinner targets offer a geometrical increase in charge density at the rear target surface, allowing for enhanced ion acceleration.

## Chapter 6: Conclusion

Throughout this experimental campaign, a large number of targets of varying thicknesses were irradiated with the Texas Petawatt laser. Extensive measurements were made of the spectral properties of particles produced from these laser-matter interactions. In addition, contrast measurements of the Texas Petawatt laser pulse were carried out in order to determine the relative intensities of disruptive pre-pulse and pedestal features. Plasma mirrors were also selectively employed as filters to enhance the contrast of the laser, at the expense of some of the pulse energy. Manipulation of the pulse contrast and the target parameters allowed for some experimental control of the interaction conditions between the laser pulse with the target, allowing for the investigation of several different regimes.

In addition, contrast measurements of the Texas Petawatt laser pulse were carried out in order to determine the relative intensities of disruptive pre-pulse and pedestal features. These measurements show a 4.5 nanosecond long pedestal at an intensity contrast of  $10^{-8}$  that is roughly centered on the main pulse. In addition, numerous pencil beam pre-pulses tens of nanoseconds before the main pulse were detected by these measurements. Of these pencil beams, the most intense pair of pulses arrive about 50 nanoseconds before the onset of peak intensity with intensities a few  $10^{-8}$  of the main pulse. In addition, a number of post-pulses were identified within the 4.5 nanosecond temporal window occupied by the stretched laser pulse. These post-pulses likely modulate the amplitude of the stretched pulse, causing nonlinear effects that produce pre-

pulses within the temporal window of the pedestal. The calculated intensities of these pre-pulses reach values between  $10^{-8}$  and  $10^{-6}$  of the main pulse.

The irradiation of targets thicker than one micrometer was investigated through measurements ions and electrons. These measurements are consistent with a physical picture in which thick targets were able to survive the pre-pulse and pedestal features of the laser intensity profile described above. The persistence of a sharp density gradient at the rear surface of these targets allowed for the production of energetic ions by the target normal sheath acceleration process. However, ion energies observed from these targets were relatively low when compared to values in the literature. This suggests that the pre-plasma conditions were not ideal during these experiments, likely due to the presence of the many pre-pulses in the laser system. Additional evidence for this conclusion is provided by the increased ion energies produced from these targets when plasma mirrors were used to improve the laser pulse contrast.

Comparable results were obtained when ultrathin nanoscale targets were irradiated with the use of plasma mirrors, suggesting that similar TNSA dynamics were at play in this regime. This configuration resulted in significantly higher ion energies than the irradiation of thick targets, but seemed to show a less efficient coupling of laser energy into hot electrons. This suggests that the irradiation of thinner targets produced greater ion energies due to a more advantageous geometry. However, this effect was not significant enough to provide a clear dependence of the maximum proton energy on target thickness within this regime, likely due to significant shot to shot fluctuations in the laser system.

Ions were not observed from nanoscale targets irradiated without plasma mirrors, suggesting that these targets did not maintain a sharp density interface until the arrival of the main laser pulse. This is consistent with density measurements of the target pre-plasma under these conditions, which was determined to be well below critical density. These results suggest that these targets were destroyed well before the arrival of the main pulse, leaving only a diffuse cloud of plasma. In this configuration, copper stacks were activated by bremsstrahlung photons emitted by laser accelerated electrons. The filamentary spatial signature of the activation signal from the thinnest targets is consistent with the direct laser acceleration of these particles. Again, this suggests the interaction of the main laser pulse with an underdense plasma cloud when ultrathin targets were irradiated without plasma mirrors.

Unfortunately, some gaps exist in the data collected during these experiments. Attempts to measure the effect of plasma mirrors on the pulse contrast were mostly unsuccessful. As such, it is only possible to infer their effect from the measured particle data. In addition, the interferometric data includes measurements from just a single instant in time, and only on one side of the original target. Needless to say, a fully time-resolved measurement of this plasma over a larger spatial region would be preferable. From this more complete data set, one could perhaps determine the time at which the plasma was formed and maybe even identify the responsible pre-pulse. These measurements could also shed light on the location of all the target material that was missing from the plasma at the time of interrogation during this experiment.

More ambitiously, any future experimental campaign that intends to produce ions at the Texas Petawatt Laser should consider implementing a more robust plasma diagnostic. The results presented in this thesis have clearly demonstrated the significance of pre-formed plasma to the ion acceleration process from solid targets, an effect that is also well documented in the literature. A full understanding of the physical principles at play on any laser systems therefore requires knowledge of the pre-plasma properties. As such, plasma density measurements from both the front and rear target surfaces should be collected for various target thicknesses with an improved diagnostic. In order to minimize the effect of shot to shot variations in the system, this device should provide a time-resolved picture of the plasma evolution. This could be accomplished through the use of a probe pulse train or the introduction of a long probe pulse recorded by a streak camera or framing camera.

Taken as a whole, these experimental results demonstrate the ability to influence the interaction between an ultrahigh intensity laser and a target through the manipulation of target properties and laser pulse contrast. The judicious choice of target thickness and composition will be an important part of future efforts to optimize the production of high quality particle beams using lasers. Efforts to improve the contrast of laser systems will also have a significant impact in this field. As the state of the art continues to advance, these observations will provide an important reference for future experiments.

## Bibliography

- [1] S.-W. Bahk, P. Rousseau, T. A. Planchon, V. Chvykov, G. Kalintchenko, A. Maksimchuk, G. A. Mourou, and V. Yanovsky. Generation and Characterization of the Highest Laser Intensities ( $10^{22}$  W/cm<sup>2</sup>). *Optics Letters*, 29: 2837, 2004.
- [2] D. Strickland and G. Mourou. Compression of Amplified Chirped Optical Pulses. *Optics Communications*, 56: 219, 1985.
- [3] Y.-H. Chuang, L. Zheng, and D. D. Meyerhofer. Propagation of Light Pulses in a Chirped-Pulse-Amplification Laser. *IEEE Journal of Quantum Electronics*, 29: 270, 1993.
- [4] O. Svelto. Principles of Lasers. Fifth Edition. Springer Science & Business Media., 2010.
- [5] I. N. Ross, P. Matousek, M. Towrie, A. J. Langley, and J. L. Collier. The Prospects for Ultrashort Pulse Duration and Ultrahigh Intensity Using Optical Parametric Chirped Pulse Amplifiers. *Optics Communications*, 144: 125, 1997.
- [6] Y.-H. Chuang, D. D. Meyerhofer, S. Augst, H. Chen, J. Peatross, and S. Uchida. Suppression of the Pedestal in a Chirped-Pulse-Amplification Laser. *J. Opt. Soc. Am. B*, 8: 1226, 1991.
- [7] M. Kaluza, J. Schreiber, M. I. K. Santala, G. D. Tsakiris, K. Eidmann, J. Meyer-ter-Vehn, and K. J. Witte. Influence of the Laser Prepulse on Proton Acceleration in Thin-Foil Experiments. *Phys. Rev. Lett.*, 93: 045003, 2004.
- [8] Y. Beaudoin, C. Y. Chien, J. S. Coe, J. L. Tapie, and G. Mourou. Ultrahigh-Contrast Ti:sapphire/Nd:glass Terawatt Laser System. *Optics Letters*, 17: 865, 1992.
- [9] F. Billhardt, M. Kalashnikov, P. V. Nickles and I. Will. A High-Contrast Ps-Terawatt Nd:Glass Laser System with Fiberless Chirped Pulse Amplification. *Optics Communications*, 98: 99, 1993.
- [10] J. D. Kmetec, J. J. Macklin, and J. E Young. 0.5-TW, 125-FS Ti:Sapphire Laser. *Optics Letters*, 16: 1001, 1991.
- [11] B. Luther-Davies, E. G. Gamaly, Y. Wang, and V. T. Tikhonchuk. Interaction of Ultrashort Powerful Laser Pulses with Matter. *Laser Physics*, 1: 325, 1991.
- [13] J. Itatani, J. Faure, M. Nantel, G. Mourou, and S. Watanabe. Suppression of the Amplified Spontaneous Emission in Chirped-Pulse-Amplification Lasers by Clean High-Energy Seed-Pulse Injection. *Optics Communications*, 148: 70, 1998.
- [14] M. Nantel, J. Itatani, A.-C. Tien, J. Faure, D. Kaplan, M. Bouvier, T. Buma, P. Van Rompay, J. Nees, P. P. Pronko, D. Umstadter, and G. A. Mourou. Temporal

- Contrast in Ti:Sapphire Lasers: Characterization and Control. *IEEE Journal of Selected Topics in Quantum Electronics*, 4: 449, 1998.
- [15] J. E. Murray, B. Vanwonderghem, L. Seppala, D. R. Speck, and J. R. Murray. Parasitic Pencil Beams Caused by Lens Reflections in Laser Amplifier Chains. *Proceedings of the 1st Annual International Conference on Lasers for Application to Inertial Confinement Fusion*, 1995.
- [16] N. V. Didenko, A. V. Konyashchenko, A. P. Lutsenko, S. Yu. Tenyakov. Contrast degradation in a chirped-pulse amplifier due to generation of prepulses by postpulses. *Optics Express*, 16: 3178, 2008.
- [17] W. E. White, F. G. Patterson, R. L. Combs, D. F. Price, and R. L. Shepherd. Compensation of Higher-Order Frequency-Dependent Phase Terms in Chirped-Pulse Amplification Systems. *Optics Letters*, 18: 1343, 1993.
- [18] M. D. Perry, T. Ditmire, and B. C. Stuart. Self-Phase Modulation in Chirped-Pulse Amplification. *Optics Letters*, 19: 2149, 1994.
- [19] O. A. Konoplev and D. D. Meyerhofer. Cancellation of B-Integral Accumulation for CPA Lasers. *IEEE Journal of Quantum Electronics*, 4: 459, 1998.
- [20] M. D. Perry, F. G. Patterson, and J. Weston. Spectral Shaping in Chirped-Pulse Amplification. *Optics Letters*, 15: 381, 1990.
- [21] D. A. Kleinman. Theory of Optical Parametric Noise. *Phys. Rev.*, 174: 1027, 1968.
- [21] F. Tavella, K. Schmid, N. Ishii, A. Marcinkevicius, L. Veisz, and F. Krausz. High-Dynamic Range Pulse-Contrast Measurements of a Broadband Optical Parametric Chirped-Pulse Amplifier. *Appl. Phys. B.*, 81: 753, 2005.
- [23] S. Witte, R. Th. Zinkstok, A. L. Wolf, W. Hogervorst, W. Ubachs, and K. S. E. Eikema. A Source of 2 Terawatt, 2.7 Cycle Laser Pulses Based on Noncollinear Optical Parametric Chirped Pulse Amplification. *Optics Express*, 14: 8168, 2006.
- [24] S. Witte and K. S. E. Eikema. Ultrafast Optical Parametric Chirped-Pulse Amplification. *IEEE Journal of Selected Topics in Quantum Electronics*, 18: 296, 2012.
- [25] N. Forget, A. Cotel, E. Brambrink, P. Audebert, C. Le Blanc, A. Jullien, O. Albert, and G.s Chériaux. Pump-Noise Transfer in Optical Parametric Chirped-Pulse Amplification. *Optics Letters*, 30: 2921, 2005.
- [26] H. C. Kapteyn, M. M. Murnane, A. Szoke, and R. W. Falcone. Prepulse Energy Suppression for High-Energy Ultrashort Pulses Using Self-Induced Plasma Shuttering. *Optics Letters*, 16: 490, 1991.
- [27] I. Hutchinson. Principles of Plasma Diagnostics, Second Edition. Cambridge University Press, 2002.

- [28] T. W. B. Kibble. Refraction of Electron Beams by Intense Electromagnetic Waves. *Phys. Rev. Lett.*, 16: 1054, 1966.
- [29] S. C. Wilks, W. L. Kruer, M. Tabak, and A. B. Langdon. Absorption of Ultra-Intense Laser Pulses. *Phys. Rev. Lett.*, 69: 1383, 1992.
- [30] J. P. Freidberg, R. W. Mitchell, R. L. Morse, and L. I. Rudsinski. Resonant Absorption of Laser Light by Plasma Targets. *Phys. Rev. Lett.*, 28: 795, 1972.
- [31] P. Gibbon and E. Forster. Short-Pulse Laser–Plasma Interactions. *Plasma Phys. Control. Fusion*, 38: 769, 1996.
- [32] T. Speziale and P. J. Catto. Cold Plasma Wavebreaking in the Presence of an Electromagnetic Driver. *Phys. Fluids*, 22: 681, 1979.
- [33] F. Brunel. Not-So-Resonant, Resonant Absorption. *Phys. Rev. Lett.*, 59: 52, 1987.
- [34] E. S. Weibel. Anomalous Skin Effect in a Plasma. *Phys. Fluids*, 10: 741, 1967.
- [35] W. Rozmus And V. T. Tikhonchuk. Skin Effect and Interaction of Short Laser Pulses with Dense Plasmas. *Phys. Rev. A*, 42: 7401, 1990.
- [36] W. L. Kruer and K. Estabrook. J x B Heating by Very Intense Laser Light. *Phys. Fluids*, 28: 430, 1985.
- [37] S. C. Wilks and W. L. Kruer. Absorption of Ultrashort, Ultra-Intense Laser Light by Solids and Overdense Plasmas. *IEEE Journal of Selected Topics in Quantum Electronics*, 33: 1954, 1997.
- [38] T.E. Cowan, M. Roth, J. Johnson, C. Brown, M. Christl, W. Fountain, S. Hatchett, E.A. Henry, A.W. Hunt, M.H. Key, A. MacKinnon, T. Parnell, D.M. Pennington, M.D. Perry, T.W. Phillips, T.C. Sangster, M. Singh, R. Snavely, M. Stoyer, Y. Takahashi, S.C. Wilks, and K. Yasuike. Intense Electron and Proton Beams from PetaWatt Laser-Matter Interactions. *Nuclear Instruments and Methods in Physics Research A*, 455: 130-139, 2000.
- [39] M. I. K. Santala, M. Zepf, I. Watts, F. N. Beg, E. Clark, M. Tatarakis, K. Krushelnick, A. E. Dangor, T. McCanny, I. Spencer, R. P. Singhal, K.W. D. Ledingham, S. C. Wilks, A. C. Machacek, J. S. Wark, R. Allott, R. J. Clarke, and P. A. Norreys. Effect of the Plasma Density Scale Length on the Direction of Fast Electrons in Relativistic Laser-Solid Interactions. *Phys. Rev. Lett.*, 84: 1459-1462, 2000.
- [40] A. Pukhov and J. Meyer-ter-Vehn. Relativistic Magnetic Self-Channeling of Light in Near-Critical Plasma: Three-Dimensional Particle-in-Cell Simulation. *Phys. Rev. Lett.*, 76: 3975-3978, 1996.
- [41] A. Pukhov, Z.-M. Sheng, and J. Meyer-ter-Vehn. Particle Acceleration in Relativistic Laser Channels. *Phys. Plasmas*, 6: 2847-2854, 1999

- [42] C. Gahn, G. D. Tsakiris, A. Pukhov, J. Meyer-ter-Vehn, G. Pretzler, P. Thirolf, D. Habs, and K. J. Witte. Multi-MeV Electron Beam Generation by Direct Laser Acceleration in High-Density Plasma Channels. *Phys. Rev. Lett.*, 83: 4772-4775, 1999.
- [43] D. Giulietti, M. Galimberti, A. Giulietti, L. A. Gizzi, R. Numico, P. Tomassini, M. Borghesi, V. Malka, S. Fritzler, M. Pittman, K. Ta Phouc, and A. Pukhov. Production of Ultracollimated Bunches of Multi-MeV Electrons by 35 fs Laser Pulses Propagating in Exploding-Foil Plasmas. *Phys. Plasmas*, 9: 3655-3658, 2002.
- [44] W. I. Linlor. Ion Energies Produced by Laser Giant Pulse. *Appl. Phys. Lett.*, 3: 210, 1963.
- [45] S. J. Gitomer, R. D. Jones, F. Begay, A. W. Ehler, J. F. Kephart, and R. Kristal. Fast Ions and Hot Electrons in the Laser-Plasma Interaction. *Phys. Fluids*, 29: 2679, 1986.
- [46] J. Denavit. Collisionless Plasma Expansion Into a Vacuum. *Phys. Fluids*, 22: 1384, 1979.
- [47] M. D. Perry, D. Pennington, B. C. Stuart, G. Tietbohl, J. A. Britten, C. Brown, S. Herman, B. Golick, M. Kartz, J. Miller, H. T. Powell, M. Vergino, and V. Yanovsky. Petawatt Laser Pulses. *Optics Letters*, 24: 160, 1999.
- [48] S. P. Hatchett, C. G. Brown, T. E. Cowan, E. A. Henry, J. S. Johnson, M. H. Key, J. A. Koch, A. B. Langdon, B. F. Lasinski, R. W. Lee, A. J. Mackinnon, D. M. Pennington, M. D. Perry, T. W. Phillips, M. Roth, T. C. Sangster, M. S. Singh, R. A. Snavely, M. A. Stoyer, S. C. Wilks, and K. Yasuike. Electron, Photon, and Ion Beams from the Relativistic Interaction of Petawatt Laser Pulses with Solid Targets. *Phys. Plasmas*, 7: 2076, 2000.
- [49] R. A. Snavely, M. H. Key, S. P. Hatchett, T. E. Cowan, M. Roth, T. W. Phillips, M. A. Stoyer, E. A. Henry, T. C. Sangster, M. S. Singh, S. C. Wilks, A. MacKinnon, A. Offenberger, D. M. Pennington, K. Yasuike, A. B. Langdon, B. F. Lasinski, J. Johnson, M. D. Perry, and E. M. Campbell. Intense High-Energy Proton Beams from Petawatt-Laser Irradiation of Solids. *Phys. Rev. Lett.*, 85: 2945, 2000.
- [50] S. C. Wilks, A. B. Langdon, T. E. Cowan, M. Roth, M. Singh S. Hatchett, M. H. Key, D. Pennington, A. MacKinnon, and R. A. Snavely. Energetic Proton Generation in Ultra-Intense Laser-Solid Interactions. *Phys. Plasmas*, 8: 542, 2001.
- [51] P. Mora. Plasma Expansion Into a Vacuum. *Phys. Rev. Lett.*, 90: 185002, 2003.
- [52] T. Grismayer and P. Mora. Influence of a Finite Initial Ion Density Gradient on Plasma Expansion Into a Vacuum. *Phys. Plasmas*, 13: 032103, 2006.
- [53] A. J. Mackinnon, M. Borghesi, S. Hatchett, M. H. Key, P. K. Patel, H. Campbell, A. Schiavi, R. Snavely, S. C. Wilks, and O. Willi. Effect of Plasma Scale Length on

- Multi-MeV Proton Production by Intense Laser Pulses. *Phys. Rev. Lett.*, 86: 1769, 2001.
- [54] B. M. Hegelich, B. Albright, P. Zudebert, A. Blazevic, E. Brambrink, J. Cobble, T. Cowan, J. Fuchs, J. C. Gauthier, C. Gautier, M. Geissel, D. Habs, R. Johnson, S. Karsch, A. Kemp, S. Letzring, M. Roth, U. Schramm, J. Schreiber, K. J. Witte, and J. C. Fernández. Spectral Properties of Laser-Accelerated Mid-Z MeV/u Ion Beams. *Phys. Plasmas*, 12: 056314, 2005.
- [55] M. Allen, P. K. Patel, A. Mackinnon, D. Price, S. Wilks, and E. Morse. Direct Experimental Evidence of Back-Surface Ion Acceleration from Laser-Irradiated Gold Foils. *Phys. Rev. Lett.*, 93: 265004, 2004.
- [56] M. Hegelich, S. Karsch, G. Pretzler, D. Habs, K. Witte, W. Guenther, M. Allen, A. Blazevic, J. Fuchs, J. C. Gauthier, M. Geissel, P. Audebert, T. Cowan, and M. Roth. MeV Ion Jets from Short-Pulse-Laser Interaction with Thin Foils. *Phys. Rev. Lett.*, 89: 085002, 2002.
- [57] B. M. Hegelich, B. J. Albright, J. Cobble, K. Flippo, S. Letzring, M. Paffett, H. Ruhl, J. Schreiber, R. K. Schulze, and J. C. Fernández. Laser Acceleration of Quasi-Monoenergetic MeV Ion Beams. *Nature*, 439: 441-444, 2006.
- [58] H. Schworer, S. Pfotenhauer, O. Ja'ckel, K.-U. Amthor, B. Liesfeld, W. Ziegler, R. Sauerbrey, K. W. D. Ledingham, and T. Esirkepov. Laser-Plasma Acceleration of Quasi-Monoenergetic Protons from Microstructured Targets. *Nature*, 439: 445-448, 2006.
- [59] L. Yin, B. J. Albright, B. M. Hegelich, and J. C. Fernandez. GeV Laser Ion Acceleration from Ultrathin Targets: The Laser Break-Out Afterburner. *Laser and Particle Beams*, 24: 291-298, 2006.
- [60] L. Yin, B. J. Albright, D. Jung, R. C. Shah, S. Palaniyappan, K. J. Bowers, A. Henig, J. C. Fernandez, and B. M. Hegelich. Break-Out Afterburner Ion Acceleration in the Longer Laser Pulse Length Regime. *Phys. Plasmas*, 18: 063103, 2011.
- [61] D. Jung, L. Yin, D. C. Gautier, H.-C. Wu, S. Letzring, B. Dromey, R. Shah, S. Palaniyappan, T. Shimada, R. P. Johnson, J. Schreiber, D. Habs, J. C. Fernández, B. M. Hegelich, and B. J. Albright. Laser-Driven 1 GeV Carbon Ions from Preheated Diamond Targets in the Break-Out Afterburner Regime. *Phys. Plasmas*, 20: 083103, 2013.
- [62] O. Buneman. Dissipation of Currents in Ionized Media. *Phys. Rev.*, 115: 503, 1959.
- [63] B. J. Albright, L. Yin, Kevin J. Bowers, B. M. Hegelich, K. A. Flippo, T. J. T. Kwan, and J. C. Fernández. Relativistic Buneman Instability in the Laser Breakout Afterburner. *Phys. Plasmas*, 14: 094502, 2007.
- [64] A. Henig, D. Kiefer, K. Markey, D. C. Gautier, K. A. Flippo, S. Letzring, R. P. Johnson, T. Shimada, L. Yin, B. J. Albright, K. J. Bowers, J. C. Fernandez, S. G.

- Rykovanov, H.-C. Wu, M. Zepf, D. Jung, V. Kh. Liechtenstein, J. Schreiber, D. Habs, and B. M. Hegelich. Enhanced Laser-Driven Ion Acceleration in the Relativistic Transparency Regime. *Phys. Rev. Lett.*, 103: 045002, 2009.
- [65] L. Yin, B. J. Albright, B. M. Hegelich, K. J. Bowers, K. A. Flippo, T. J. T. Kwan, and J. C. Fernández. Monoenergetic and GeV Ion Acceleration from the Laser Breakout Afterburner Using Ultrathin Targets. *Phys. Plasmas*, 14: 056706, 2007.
- [66] E. W. Gaul, M. Martinez, J. Blakeney, A. Jochmann, M. Ringuette, D. Hammond, T. Borger, R. Escamilla, S. Douglas, W. Henderson, G. Dyer, A. Erlandson, R. Cross, J. Caird, C. Ebberts, and T. Ditmire. Demonstration of a 1.1 Petawatt Laser Based on a Hybrid Optical Parametric Chirped Pulse Amplification/Mixed Nd:glass Amplifier. *Applied Optics*, 49: 1676, 2010.
- [67] B. Dromey, S. Kar, M. Zepf, and P. Foster. The Plasma Mirror - A Subpicosecond Optical Switch for Ultrahigh Power Lasers. *Rev. Sci. Instrum.*, 75: 645, 2004.
- [68] J. J. Thomson. Rays of Positive Electricity. *Phil. Mag. S.*, 21: 225, 1911.
- [69] D. Jung, R. Hörlein, D. Kiefer, S. Letzring, D. C. Gautier, U. Schramm, C. Hübsch, R. Öhm, B. J. Albright, J. C. Fernandez, D. Habs, and B. M. Hegelich. Development of a High Resolution and High Dispersion Thomson Parabola. *Rev. Sci. Instrum.*, 82: 013306, 2011.
- [70] FujiFilm's Proprietary Imaging Plate - Fujifilm Corporation
- [71] B. Hidding, G. Pretzler, M. Clever, F. Brandl, F. Zamponi, A. Lübcke, T. Kämpfer, I. Uschmann, E. Förster, U. Schramm, R. Sauerbrey, E. Kroupp, L. Veisz, K. Schmid, S. Benavides, and S. Karsch. Novel Method for Characterizing Relativistic Electron Beams in a Harsh Laser-Plasma Environment. *Rev. Sci. Instrum.*, 78: 083301, 2007.
- [72] Image Format Description - BAS2500 System - Fujifilm Corporation (2003).
- [73] Kazuo A. Tanaka, Toshinori Yabuuchi, Takashi Sato, Ryosuke Kodama, Yoneyoshi Kitagawa, Teruyoshi Takahashi, Toshiji Ikeda, Yoshihide Honda, and Shuuichi Okuda. Calibration of Imaging Plate for High Energy Electron Spectrometer. *Rev. Sci. Instrum.*, 76: 013507, 2005.
- [74] C. G. Freeman, G. Fiksel, C. Stoeckl, N. Sinenian, M. J. Canfield, G. B. Graeper, A. T. Lombardo, C. R. Stillman, S. J. Padalino, C. Mileham, T. C. Sangster, and J. A. Frenje. Calibration of a Thomson Parabola Ion Spectrometer and Fujifilm Imaging Plate Detectors for Protons, Deuterons, and Alpha Particles. *Rev. Sci. Instrum.*, 82: 073301, 2011.
- [75] A. Mančić, J. Fuchs, P. Antici, S. A. Gaillard, and P. Audebert. Absolute Calibration of Photostimulable Image Plate Detectors Used as 0.5–20 MeV High-Energy Proton Detectors. *Rev. Sci. Instrum.*, 79: 073301, 2008.

- [76] M. M. Günther, A. Britz, R. J. Clarke, K. Harres, G. Hoffmeister, F. Nürnberg, A. Otten, A. Pelka, M. Roth, and K. Vogt. NAIS: Nuclear Activation-Based Imaging Spectroscopy. *Rev. Sci. Instrum.*, 84: 073305, 2013.
- [77] I. Pomerantz, E. McCary, A. R. Meadows, A. Arefiev, A. C. Bernstein, C. Chester, J. Cortez, M. E. Donovan, G. Dyer, E. W. Gaul, D. Hamilton, D. Kuk, A. C. Lestrade, C. Wang, T. Ditmire, and B. M. Hegelich. Ultrashort Pulsed Neutron Source. *Phys. Rev. Lett.*, 113: 184801, 2014.
- [78] A. Niroomand-Rad, C. R. Blackwell, B. M. Coursey, K. P. Gall, J. M. Galvin, W. L. McLaughlin, A. S. Meigooni, R. Nath, J. E. Rodgers, and C. G. Soares. Radiochromic Film Dosimetry. *Medical Physics*, 25: 2093, 1998.
- [79] F. Nürnberg, M. Schollmeier, E. Brambrink, A. Blažević, D. C. Carroll, K. Flippo, D. C. Gautier, M. Geißel, K. Harres, B. M. Hegelich, O. Lundh, K. Markey, P. McKenna, D. Neely, J. Schreiber, and M. Roth. Radiochromic Film Imaging Spectroscopy of Laser-Accelerated Proton Beams. *Rev. Sci. Instrum.*, 80: 033301, 2009.
- [80] D. S. Hey, M. H. Key, A. J. Mackinnon, A. G. MacPhee, P. K. Patel, R. R. Freeman, L. D. Van Woerkom, and C. M. Castaneda. Use of GafChromic Film to Diagnose Laser Generated Proton Beams. *Rev. Sci. Instrum.*, 79: 053501, 2008.
- [81] R. N. Gyuzalian, S.B. Sogomonian, and Z. G. Horvath. Background-Free Measurement of Time Behaviour of an Individual Picosecond Laser Pulse. *Optics Communications*, 29: 239, 1979.
- [82] J. Janszky, G. Corradi, and R. N. Gyuzalian. On a Possibility of Analysing the Temporal Characteristics of Short Light Pulses. *Optics Communications*, 23: 293, 1977.
- [83] S. Luan, M. H. R. Hutchinson, R. A. Smith, and F. Zhou. High Dynamic Range Third-Order Correlation Measurement of Picosecond Laser Pulse Shapes. *Meas. Sci. Technol.*, 4: 1426, 1993.
- [84] E. I. Blount and J. R. Klauder. Recovery of Laser Intensity from Correlation Data. *Journal of Applied Physics*, 40: 2874, 1969.
- [85] J. Collier, C. Hernandez-Gomez, R. Allott, C. Danson, and A. Hall. A Single-Shot Third-Order Autocorrelator for Pulse Contrast and Pulse Shape Measurements. *Laser and Particle Beams*, 19: 231, 2001.
- [86] R. Wyatt and E. E. Marinero. Versatile Single-Shot Background-Free Pulse Duration Measurement Technique, for Pulses of Subnanosecond to Picosecond Duration. *Appl. Phys.*, 25: 297, 1981.
- [87] J. Hebling. Derivation of the Pulse Front Tilt Caused by Angular Dispersion. *Optical and Quantum Electronics*, 28: 1759, 2996.

- [88] S. S. Harilal and M. S. Tillack. Laser Plasma Density Measurements Using Interferometry, UCSD-ENG-114, 2004.
- [89] M. Takeda, H. Ina, and S. Kobayashi. Fourier-Transform Method of Fringe-Pattern Analysis for Computer-Based Topography and Interferometry. *J. Opt. Soc. Am.*, 72: 156, 1982.
- [90] W. R. Grigsby. Experimental Studies of High Energy Density Silicon Using Ultra-Fast Lasers. The University of Texas at Austin. Ph.D. Thesis, 2007.
- [91] D. C. Ghiglia and M. D. Pritt. Two-Dimensional Phase Unwrapping: Theory, Algorithms, and Software.
- [92] T. J. Flynn. Two-Dimensional Phase Unwrapping with Minimum Weighted Discontinuity. *J. Opt. Soc. Am.*, 14: 2692, 1997.
- [93] R. M. Goldstein, H. A. Zebker, and C. L. Werner. Satellite Radar Interferometry' Two-Dimensional Phase Unwrapping. *Radio Science*, 23: 713, 1988.
- [94] D. J. Bone. Fourier Fringe Analysis: The Two-Dimensional Phase Unwrapping Problem. *Applied Optics*, 30: 3627, 1991.
- [95] E. Gaul, N. Kandadai, G. Dyer, T. Borger, M. Martinez, M. Spinks, M. Donovan, and T. Ditmire. Pulse Contrast Measurements of the Texas Petawatt Laser. *Research in Optical Sciences, OSA Technical Digest*, paper JW2A.23, 2014.
- [96] M. J. Berger, J. S. Coursey, M. A. Zucker, and J. Chang. ESTAR, PSTAR, and ASTAR: Computer Programs for Calculating Stopping-Power and Range Tables for Electrons, Protons, and Helium Ions (version 1.2.3). Available: <http://physics.nist.gov/Star>. National Institute of Standards and Technology, 2005.
- [97] J. R. Davies. Laser Absorption by Overdense Plasmas in the Relativistic Regime. *Plasma Phys. Control. Fusion*, 51: 014006, 2009.